NTNU

Norwegian University of
Science and Technology

Thrust Optimisation of an Oscillating Hydrofoil

By Non-Sinusoidal Sway and Yaw Motion

Lennard Bösch

Marine Technology
Submission date: June 2017
Supervisor: Trygve Kristiansen, IMT
Co-supervisor: John Martin Kleven Godø, IMT

Norwegian University of Science and Technology
Department of Marine Technology

Summary

Past research has shown that oscillating hydrofoils can enhance the propulsion efficiency significantly compared to traditional propellers. Dynamic stall plays an important role in the thrust generated by an oscillating hydrofoil, combining this with non-sinusoidal motion makes it an complicated phenomenon to investigate.

Genetic optimisation algorithms are employed to optimise the motion for thrust efficiency of a NACA0015 foil with a 7.5cm chord oscillating in sway and yaw. The optimisation algorithm selects motion-parameters during model-scale experiments, and adjusts these to optimise thrust efficiency. Experiments are conducted in a circulating water tunnel (CWT) at the Norwegian University of Science and Technology (NTNU). Thrust efficiency was successfully increased compared to previous research, where traditional parametric search methods were applied.

Two different flow conditions are considered: one at low Reynolds number with a wide range of Strouhal number (S_t); and another with higher Reynolds number, and a turbulent boundary layer through turbulence stimulation. Thrust efficiency is measured to above 60% for a wide range of thrust coefficients $0.02 < C_T < 0.6$. If drag at zero angle of attack is disregarded, efficiencies above 90% are observed at $C_T < 0.2$.

Previous experiments by J. Anderson, Streitlien, Barrett, and Triantafyllou (1998) were successfully repeated. Good agreement was found for many of their results, except for a few cases.

The phase between sway and yaw showed a tendency towards $\phi = 75°$ if the Strouhal number is above $S_t > 0.2$, for which a reverse Von Kármán vortex street is expected.

For further work, all results from the optimisation experiments are listed in the attached *.csv* file, raw-data is available on request. The data generated for the optimisation experiments is enormous. A lot can still be investigated regarding the ideal motion parameters, and how thrust and power consumption varies through one oscillation. Additionaly it would be very interesting to look for similarities between the genetic algorithm, and motions of the dorsal fin on thunniform swimmers (Dolphines, Tunas, etc.). For which the author was unable to find any literature concerning measurements of the exact sway and yaw motion.

Sammendrag

Tidligere forskning har vist at oscillerende hydrofoiler kan forbedre fremdriftseffektiviteten betydelig sammenlignet med tradisjonelle propellere. Dynamisk stall spiller en viktig rolle i kraften som genereres av en oscillerende hydrofoil, kombinert med ikke-sinusformet bevegelse blir dette et komplisert fenomen å undersøke.

Genetiske optimaliseringsalgoritmer er benyttet for å optimalisere bevegelsen for framdriftsvirkningsgraden av en NACA0015 foil med en 7,5 cm lang korde, som oscillerer sideveis og i rotasjon. Optimaliseringsalgoritmen velger bevegelsesparametere under modellskalaeksperimenter, og justerer disse for å optimalisere fremdriftsvirkningsgraden. Eksperimenter utføres i en sirkulasjonstunnel (CWT) ved Norges teknisk-naturvitenskapelige universitet (NTNU). Fremdriftseffektiviteten ble vellykket økt i forhold til tidligere forskning, der tradisjonelle parametriske søkemetoder ble anvendt.

To forskjellige strømningsforhold vurderes: En til lave Reynold-tall med et bredt spekter av Strouhal-nummer (S_t); Og en annen med høyere Reynold-tall, og et turbulent grensesjikt ved bruk av turbulensstimulering. Fremdriftseffektiviteten måles til over 60% for et bredt spekter av skyvkraft-koeffisienter $0,02 < C_T < 0,6$. Hvis man fjerner drag ved null angrepsvinkel, observeres effektivitet over 90% ved $C_T < 0,2$.

Tidligere eksperimenter av J. Anderson et al. (1998) ble repetert. Veldig godt samsvar ble funnet for mange av deres resultater, bortsett fra noen få tilfeller.

Fasen mellom sideveis- og rotasjons-bevegelse viser en tendens til $\phi = 75°$ hvis Strouhal-tallet er over $S_t > 0,2$. Her forventes det at det oppstår en reversert Von Kármán virvelgate.

For videre arbeid er alle resultatene fra optimaliseringseksperimentene oppført i vedlagt *.csv* filen. Rådata er tilgjengelig på forespørsel. Dataene som genereres for optimaliseringseksperimentene er enorme. Det er fortsatt mye som kan undersøkes om de ideelle bevegelses-parameterne, og hvordan trykk og strømforbruk varierer gjennom en oscilasjon. I tillegg vil være veldig interessant å se etter likheter mellom bevegelsen til den genetiske algoritmen og bevegelser av halefinnen på *thunniform*-svømmere (Delfin, Tunfisk, etc.).

Preface

This thesis is part of the 5-year study programme, Marine Technology at the Norwegian University for Science and Technology (NTNU). Experiments are conducted in the circulating water tunnel (CWT).

The experiments and set-up are done in collaboration with Thomas Gjerde, who wrote his separate master thesis on how to optimise bio-inspired propulsion systems using genetic algorithm. Together we worked for several months in the laboratory, a lot of time and effort was spent on automation, which was a crucial part for doing the thrust optimisation experiments.

Note: List of figures and tables is not included, as requested by the supervisor.

Acknowledgement

I would like to thank my supervisor Trygve Kristiansen, for the weekly discussions on this master thesis, and constructive feedback. In addition I would like to thank my co-advisor John Martin Kleven Godø, who gave me the idea for this thesis, and supported me through it. Gratitudes also go to Eirik Bøckmann, who showed a lot of interest in this project, and gave guidance on several occasions.

Additionally I would like to thank the NTNU-laboratory staff, especially Torgeir Wahl who assisted significantly in setting up the experiments. Also the author would like to thank Herman Schrader Bordal, who was involved in the experiments through the UROP-project.

I also want to thank my better half, Helle Skytøen, for continious support throughout the work on this thesis.

Lennard Bösch

Table of Contents

Abbreviations

LDV	=	Laser Doppler Velocimetry
PIV	=	Particle Image Velocimetry
TS	=	Turbulence Stimulation
CWT	=	Circulating Water Tunnel
AoA	=	Angle of Attack
GA	=	Genetic Algorithm
LAN	=	Local Area Network

Nomenclature

α	Angle of attack
β	Change in angle of attack due to induced sway velocity
β^{amp}	Maximum change in angle of attack due to induced sway velocity
$\cdot y_{sway}$	First timederivative of sway position
χ	Feathering parameter
$\delta_{blasius}$	Laminar boundary layer thickness, described by blasius equation
$\delta_{turb.}$	Turbulent boundary layer thickness
$\dot{y}_{sway}$	Sway position
η	Thrust efficiency
γ	Confidence Interval
μ	Mean value of a measured series
ω	Oscillation frequency in $\mathrm{rad\,s^{-1}}$
$\overline{F}$	Average thrust force over one oscillation
$\overline{P}$	Average power consumption over one oscillation
$\overline{u_{inf}}$	Mean inflow velocity
ϕ	Phase difference between sway and yaw
ρ	Fresh water density
σ	Standard deviation of a gaussian distributed series
$\sigma(u_{inf})$	standard deviation of inflow velocity
θ	Yaw angle
θ^{amp}	Yaw angle amlitude
c	Foil chord length

C_f	Skin friction coefficient
C_P	Power coefficient
C_R	Resultant Force coefficient, (vectorsum of C_l and C_T)
C_T	Thrust coefficient
$c_v(u_{inf})$	coefficient of variation of inflow velocity
C_{DS}	Total drag coefficient
f	Oscillation frequency in Hz
F_d	Drag force
F_l	Lift force
F_x	Force parallel with the foil center-line
F_y	Force perpendicular with the foil center-line
$f_{nat.}$	Natural frequency
K_θ	Non-harmonic motion parameter for yaw
K_y	Non-harmonic motion parameter for sway
M	Mach number
N	Number of oscillations
N_{crit}	Parameter describing how easy a transition from laminar to turbulent boundary layer occurs
$P_{\overline{X}}$	Relative precision error
Re_c	Chord Reynold Number
s	Foil span length
S_t	Strouhal number
S_x	Standard deviation of a measured series
T	Period for one foil oscillation
T	Turbulence intensity level
t	Foil thickness
u_{inf}	Inflow velocity

v	Kinematic viscosity of fresh-water
X_j	Sample number j for calculation of precision error
y_{sway}	Sway position
y_{sway}^{amp}	Sway amplitude

Chapter 1

Introduction

> One general law, leading to the advancement of all organic beings, namely, multiply, vary, let the strongest live and the weakest die.
>
> Charles Darwin

In this chapter the background of previous research on oscillating hydrofoils is presented. The objective and scope for this thesis is defined, together with a outline for the chapters to come.

1.1 Background

Oscillating foils is a known concept of ship propulsion and energy extraction from waves, wind and currents. A foil is oscillated in yaw and sway to generate thrust. This concept could achieve higher efficiency than a conventional propeller system since the swept water area can be larger (Yamaguchi & Bose, 1994).

Several research institutes are investigating the affect of various parameters on thrust generation and efficiency. The most cited results are by J. Anderson et al. (1998). They were able to measure a maximum efficiency of 87%, by doing a parametric search for Strouhal number (S_t), harmonic yaw/sway phase and maximum incident angle of attack (AoA).

Through model experiments Read, Hover, and Triantafyllou (2003) demonstrated that oscillating hydrofoils possibly can offer good manoeuvring capability to the vessel, and thereby neglecting the need for a rudder. This is achieved through the high oscillating lift forces.

Traditionally only sinusoidal sway and yaw motions have been considered by researchers. Hover, Haugsdal, and Triantafyllou (2004) have shown through model experiments that introducing higher harmonics to the sway motion can broadly increase thrust and efficiency. They achieved this by adjusting the higher harmonic coefficients such that a smooth AoA profile is created. Read et al. (2003) indicates that further investigations in introducing non-sinusoidal motions to both

sway and yaw could be interesting.

1.2 Literature Review

An overview is given on previous research which had the most impact on oscillating foils for propulsion. Most of this is focused on model scale experiments.

Massachusetts Institute of Technology (MIT) is one of the most prominent research institutes on oscillating foil propulsion. They have a small towing tank with equipment to do power and force measurement on a foil oscillated in heave and pitch. The towing tank is 30 m long, 2.6 m wide, and 1.3 m deep. Since the 90's several researchers used this equipment for research on oscillating hydrofoils (Hover et al., 2004; Read et al., 2003; J. Anderson et al., 1998; Triantafyllou, Triantafyllou, & Grosenbaugh, 1993).

1.2.1 Ideal Strouhal Number

A sway and yaw oscillating foil will produce a reversed Karman vortex street, where the average velocity corresponds to a jet flow. Triantafyllou et al. (1993) argues that the flow is linearly unstable, acting as a amplifier. A small band of oscillation frequencies yield maximum disturbance amplification. Triantafyllou proposes that if the efficient development of thrust is associated with the formation of staggered array of vorticies (Reverse Von Kármán Vortex Street), then the frequency of maximum instability growth must also be the frequency of maximum foil efficiency. This theory was tested in a small experiment on a NACA0012 foil in a towing tank. The experiments concluded that highest efficiency is reached in a range of $0.25 < St < 0.35$ with a peak at 0.25. The chord Reynold number in this test is $Re_c \approx 2000$. The reported thrust efficiency is still low with a peak at $\eta \approx 0.2$. This is expected due to a poor choice of other parameters (amplitude to chord length ratio, yaw axis location and feathering parameter). A description on parameters will be given in section two.

Observations in Nature

Another interesting phenomenon concerning Strouhal number, is that in nature a pattern is observed. According to Taylor, Nudds, and Thomas (2003), the Strouhal number typically coincides at $0.19 < St < 0.41$. They collected experimental results for 42 different species from various publications, which all rely on flapping flight or swimming, and concluded that 75% of the species were operating

in the proposed range of S_t. Further they argue that natural selection is likely to tune the selected animals for high propulsive efficiency.

An effort was made to find further inspiration in nature. However most scientists either investigated the energy consumption, tailbeat frequency (Syme & Shadwick, 2011), or a combination of both (Knower, 1998), no research was found concerning actual relation between sway and yaw motion. Investigations were focused on looking for animals which use the thunniform swimming technique, because it is referred to the most efficient locomotion mode evolved in the aquatic environment (Sfakiotakis, Lane, & Davies, 1999). Additionally 90% of the thrust is generated through lifting forces on the caudal fin, making it comparable to one oscillating hydrofoil. According to Sfakiotakis et al. (1999), thunniform locomotion is used by for example: Tuna, mackerel, sharks, and marine mammals (dolphins, whales, etc.).

1.2.2 High Thrust Efficiency

J. Anderson et al. (1998) continued the work of Triantafyllou in the same towing tank. By doing parametric variations she investigated how other parameters affect propulsion efficiency. In general the highest efficiency was achieved for the largest tested sway motions ($H_0/c = 0.75$) with large angles of attack ($15 < \alpha_{max} < 25$), sway-yaw phase at $\phi = 75°$, and Strouhals number in the same range (0.3 to 0.4) as observed by Triantafyllou et al. (1993). The highest efficiencies were measured at 87%. Anderson indicated that a larger sway motion could be even better, because $H_0/c = 0.75$ was the highest tested value. In this thesis, $H_0/c = 1.2$ can be achieved.

1.2.3 Discrepancy between different Experiments

Read et al. (2003) repeated some of the tests done by Anderson, also at MIT, but presumably at a different towing tank, due to slight variations in the tank dimensions reported. Read was able to reproduce Andersons results where the phase was $\phi = 90°$, and efficiency was fairly high with 78%. The true efficiency, including drag, was reduced to 67%. The extraordinary high efficiency of 87%, achieved with a phase of $\phi = 75°$ was not supported by Reads experimental results. The author points out that discrepancy between the experiments can be due to low values of thrust C_T and power C_P, which makes the efficiency calculations susceptible to measurement error.

1.2.4 Effect of Angle of Attack

Hover et al. (2004) did an investigation of how the angle of attack (AoA) profile, and rate of change affects the generated thrust and efficiency. Previous researchers identified that dynamic stall and unsteady flow conditions play an important role in biomimetic propulsion, making physical design and kinematic control complicated.

The author achieved different AoA profiles by changing the heave/sway motion, and keeping pitch/yaw harmonic. By this three AoA profile types were obtained; harmonic, sawtooth, and cosine. Through systematic variation of Strouhal number and maximum AoA the author investigated how well these profiles perform in a wide range of thrust-coefficients.

1.3 Objective

The objective is to investigate if and how the motion of a oscillating hydrofoil can be adjusted to achieve high thrust efficiency. Most of previous research in this field has assumed a response for an oscillating foil, and then systematically conducted experiments. It will be investigated if the reported thrust efficiency can be exceeded by employing an optimisation algorithm, which will base the hydrofoil motion on real-time experimental model tests. The optimisation algorithm was written in the master thesis by Thomas Gjerde and employed in collaboration with him (Gjerde, 2017).

A system must be developed to analyse the foil performance automatically. In addition outliers must be detect, where either the system could not represent the desired motion, or the uncertainty is too high.

An effort will be made to determine whether non-harmonic motions in sway and yaw can give a significant improvement on thrust and efficiency. This is done by conducting two separate optimisation-experiments under the same conditions, where one experiment only allows harmonic sway and yaw motions. A comparison of the generated thrust and efficiency can then be made.

Some of the experiments done by J. Anderson et al. (1998) will be repeated. This will be done for three reasons: Firstly, Anderson presents results with extraordinary high efficiency, with a peak at $\eta \approx 87\%$; secondly, the paper is renown, with 893 citations according to Google Scholar; and finally Read et al. (2003) was able to repeat some of the experiments, but was unsuccessful in those with the highest efficiency.

1.3.1 Scope

The scope of this thesis is summarized by the following points:

- How can oscillating foil motions be optimized through model-scale experiments to deliver efficient thrust?

  What kind of motions are preferred, and are there any trends?

- What problems arise when doing foil experiments at steady and unsteady conditions with very low Reynold number ($Re_c < 100000$), and how can these be remedied?

- Investigate contradicting previous research results in this field. Either strengthen or weaken their experimental findings by repetition.

1.4 Outline

This thesis is divided into 5 chapters. In chapter two, the theory is explained, where focus is set on highlighting theory used for the experiments. Initially mathematical expressions are explained, then a short introduction is given on the genetic optimisation algorithm. Further the treatment and filtering of measurements is discussed, followed by a discussion on issues concerning scaling, and boundary layers in the circulating water tunnel (CWT).

In chapter three, set-up of the oscillating foil experiments is presented. Results which are essential to confirm a correct set-up are also presented and discussed here. This concerns measuring static forces on the foil, vibrations, and in-flow conditions of the CWT. Finally a benchmark case is presented, which is based on results by (J. Anderson et al., 1998), and will be used to confirm that experiments and measurements are executed correct.

Chapter four concerns the optimisation results, and interpretation of them. Findings are discussed directly in this chapter, and comparisons are made with other scientists.

In the final chapter, findings are summarized and concluded. A recommendation on further work is also given.

Chapter 2

Theory

A short overview of relevant theory regarding oscillating hydrofoil is given. Scaling issues are discussed, and the genetic optimisation algorithm is presented. How data processing is done during the experiments is also described.

2.1 Non-Dimensional Units

Several non-dimensional variables are typically used to describe the characteristics of a oscillating foil. This section gives a short introduction to their definition.

The Strouhal number is defined in Equation (2.1) by the relation between oscillation speed and width of the created jet flow. This is hard to define before the experiments, in several other studies this is estimated as twice the heaving amplitude (J. Anderson et al., 1998; Triantafyllou et al., 1993).

$$S_t = \frac{2f\ y_{sway}^{amp}}{u_{inf}} \tag{2.1}$$

Where f is the oscillation frequency in Hz.

The feathering parameter, χ, is based on the maximum quasi static angle of attack. It describes the relation between maximum induced angle of attack due to sway motion, β, and maximum yaw angle, θ. Lighthill (1970) defined this parameter as:

$$\chi = \frac{\theta^{amp}}{\beta^{amp}} = \frac{\theta^{amp}}{arctan(y_{sway}^{amp}\ \omega / u_{inf})} \tag{2.2}$$

Where θ and θ^{amp} are the yaw angle and yaw angle amplitude respectively, u_{inf} the inflow velocity, and ω the angular oscillation frequency.

Combining Equation (2.1) and (2.2), shows that the feathering parameter also is a relation between the Strouhal number and yaw amplitude:

$$\chi = \frac{\theta^{amp}}{arctan(\pi\ S_t)} \tag{2.3}$$

This parameter dictates whether the foil extracts energy from the flow or exerts

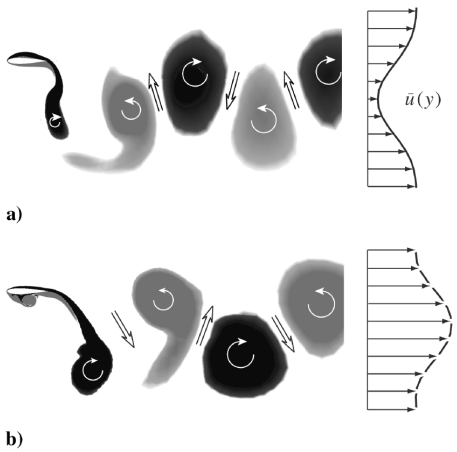

Figure 2.1: Foil wake with vortices and wake flow velocity profile, in a) the foil is extracting energy from the flow, and in b) it is generating thrust. Courtesy of Kinsey and Dumas (2008).

energy on it and can be used as propulsion. Where energy/power/force is defined as the mean through one oscillation. Kinsey and Dumas (2008) states that for $\chi > 1$ energy is extracted from the flow, and with $\chi < 1$ propulsion is generated. The dominant power regime can also be evaluated by the flow characteristics of the wake. In energy extraction the mean velocity will be less than inflow velocity, and vice versa for propulsion. As a result the vortices will change direction, as seen in Figure 2.1.

Other authors (Hover et al., 2004; J. Anderson et al., 1998) have used the maximum angle of attack (α_{max}) as a parameter to set the yaw amplitude. If parameters for an experiment would have been chosen at random, one would have to discard many tests because they would not generate any thrust. By using the feathering parameter instead, and setting its range below 1 the optimisation time is reduced by ensuring thrust generation in most of the tests.

Chord Reynold number is defined as:

$$Re_c = \frac{u_{inf}\ c}{v} \tag{2.4}$$

Where c is the foil chord length, and v the kinematic viscosity of the fluid.

2.1.1 Thrust and Power Consumption

The thrust and power consumption for foil oscillation can be expressed as coefficients, for this a reference area is needed. As a convenience the area of one foil

side is used ($c\ s$), where s is the foil span, and c the chord length. Another possibility would be to use the working area of the foil ($2\ y_{sway}^{amp}\ s$). The later would be more comparable to propeller theory, where traditionally the swept area is used as a reference. However, most authors of papers on oscillating foil propulsions are using the foil area. To make research of this thesis more comparable, the foil area is used as reference. Thrust and power coefficient are defined as (J. Anderson et al., 1998):

$$C_T = \frac{\overline{F}}{0.5\ \rho\ c\ s\ u_{inf}^2} \qquad (2.5) \qquad\qquad C_P = \frac{\overline{P}}{0.5\ \rho\ c\ s\ u_{inf}^3} \qquad (2.6)$$

where $\overline{F}$ is the average thrust force, and $\overline{P}$ the average power consumption, ρ the fluid density, c the foil chord length, s the foil span, and U_{inf} the inflow velocity.

The power consumption and thrust must be averaged over one oscillation period T. The power consumption is affected by both the sway and yaw contribution. Time-varying force and power consumption is integrated over one oscillation:

$$\overline{F} = -\frac{1}{T}\int_0^T F_d(t)dt \qquad (2.7)$$

$$\overline{P} = \frac{1}{T}\left(\int_0^T F_l(t)\ \frac{dy(t)}{dt}dt + \int_0^T M_z(t)\ \frac{d\theta(t)}{dt}dt\right) \qquad (2.8)$$

Where $F_d(t)$ and $F_l(t)$ are the forces acting in drag and lift direction respectively. $M_z(t)$ is the torque about vertical axis of the foil. $\frac{dy(t)}{dt}$ and $\frac{d\theta(t)}{dt}$ are the sway velocity and yaw-rate.

The propulsive efficiency η, is the product of useful power divided by power input:

$$\eta = \frac{\overline{F}\ u_{inf}}{\overline{P}} = \frac{C_T}{C_P} \qquad (2.9)$$

In Figure 2.2 the positive direction of the forces is notated. Because the force transducer is fixed to the foil shaft, it will measure F_x, F_y and M_z. To calculate the thrust and power coefficient, lift and drag forces are of interest. By using trigonometry these can be decomposed to Equation (2.10).

$$\begin{aligned} F_d &= F_x \cos\theta + F_y \sin\theta \\ F_l &= -F_x \sin\theta + F_y \cos\theta \end{aligned} \qquad (2.10)$$

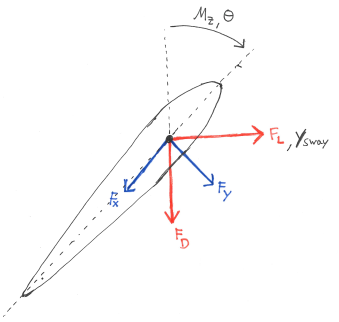

Figure 2.2: Positive direction for forces (F_x, F_y, F_d, F_l), yaw torque (M_z), sway motion (y_{sway}), and yaw rotation (θ). Water flow is coming from direction $\theta = 0$.

2.2 Yaw and Away Motion Profile

A function is needed to describe how sway and yaw varies with time. The most basic is a harmonic function, which has been used in most of the studies mentioned in Section 1.2, Literature Review. For sway and yaw it can be described as:

$$\begin{aligned} y_{sway}(t) &= y_{sway}^{amp} \ \sin(\omega \ t) \\ \theta(t) &= \theta^{amp} \ \sin(\omega \ t + \phi) \end{aligned} \tag{2.11}$$

Where y_{sway}^{amp} is the sway amplitude, and θ^{amp} the yaw amplitude, ϕ the phase difference, and ω the angular oscillation frequency.

The oscillation frequency is defined by the Strouhal number in Equation (2.1), and the yaw amplitude can be described by the feathering parameter in Equation (2.2). Rewriting these yields:

$$\omega = \frac{\pi \ u_{inf} \ S_t}{y_{sway}^{amp}} \tag{2.12}$$

$$\theta^{amp} = \chi \ \arctan(\pi \ S_t) \tag{2.13}$$

Combining these with Equation (2.11) yields:

$$y_{sway}(t) = y_{sway}^{amp} \ sin\left(\frac{\pi \ u_{inf} \ S_t}{y_{sway}^{amp}} \ t\right) \tag{2.14}$$

$$\theta(t) = \chi \ \arctan(\pi \ S_t) \ \sin\left(\frac{\pi \ u_{inf} \ S_t}{y_{sway}^{amp}} \ t + \phi\right) \tag{2.15}$$

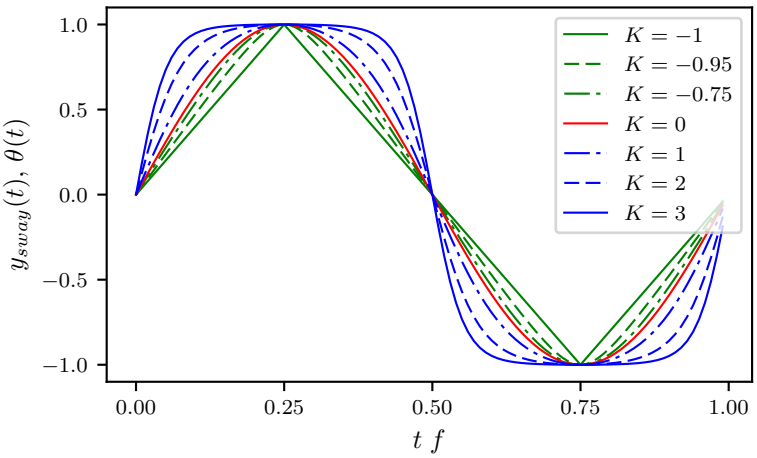

Figure 2.3: The K-profile function for sway (Equation (2.17)) or yaw (Equation (2.16)) for one period where K is varied and the following variables are fixed to: $\phi = 0°$, $f = 1$ and $\theta^{amp} = 1$ or $y^{amp}_{sway} = 1$. Courtesy of Lu et al. (2014b).

A sway and yaw motion unlike from sinus can be achieved through the use of a K-parameter. This was first described by Lu, Xie, and Zhang (2014a). One K-parameter is used for yaw (K_θ), and one for sway (K_y):

$$\theta(t) = \begin{cases} \theta^{amp}\ \arcsin[-K_\theta\ \sin(\omega\ t + \phi)] & \text{if } -1 \leq K_\theta < 0, \\ \theta^{amp}\ \sin(\omega\ t + \phi) & \text{if } K_\theta = 0, \\ \frac{\theta^{amp}\ \tanh[K_\theta\ \sin(\omega\ t + \phi)]}{\tanh(K_\theta)} & \text{if } K_\theta > 0 \end{cases} \tag{2.16}$$

$$y_{sway}(t) = \begin{cases} y^{amp}_{sway}\ \arcsin[-K_y\ \sin(\omega\ t)] & \text{if } -1 \leq K_y < 0, \\ y^{amp}_{sway}\ \sin(\omega\ t) & \text{if } K_y = 0, \\ \frac{y^{amp}_{sway}\ \tanh[K_y\ \sin(\omega\ t)]}{\tanh(K_y)} & \text{if } K_y > 0 \end{cases} \tag{2.17}$$

Where ω and θ^{amp} are defined by Equation (2.12) and (2.13).

From this it is apparent that sway and yaw motion can be fully defined by 6 parameters; the sway amplitude (y^{amp}_{sway}), Strouhal number (S_t), feathering parameter (χ), phase difference (ϕ), K-parameter for sway (K_y), and K-parameter for yaw (K_θ). These 6 parameters will be adjusted in the genetic optimisation to maximise the thrust efficiency. In addition the inflow velocity (u_{inf}) is needed, which is treated as a fixed variable in the experiments. Figure 2.3 gives an illustration on how the motion profile for either sway or yaw would look like for one period with different values of K. As a simplification the amplitudes and oscillation frequencies are set to 0.

2.2.1 Angle of Attack

The angle of attack (AoA), α, is an important parameter which is derived from the other motion parameters. The generated normal forces on the foil are highly dependent on AoA. Geometrically this is defined as the angle between foil centreline and direction of oncoming flow. For a foil oscillating in sway and yaw, two components affect AoA most. One is the yaw position of the foil, θ. The other, β, is the angle induced due to a sway velocity component, which changes the direction of oncoming flow locally on the foil.

The quasi static angle of attack at time, t, can be calculated with (Hover et al., 2004):

$$\alpha(t) = \theta(t) + \beta(t) = \theta(t) - arctan\left(\frac{\dot{y}_{sway}(t)}{u_{inf}}\right) \tag{2.18}$$

Where $\dot{y}_{sway}(t)$ is the sway velocity at time incident t.

Wake Dynamics

Through particle image velocimetry (PIV), J. M. Anderson (1996) investigated how the wake of an oscillating foil is affected by Strouhal number (S_t), and maximum angle of attack (α_{max}). The tests were conducted at a very low Reynold number, $Re_c = 1100$, using sinusoidal sway and yaw motion with a phase difference of $\phi = 90°$, and sway amplitude of $y^{amp}_{sway} = 1.0$. Wake structure is illustrated in Figure 2.4 and Anderson summarizes it into six different regions:

A, and B Drag producing Von Kármán Vortex street is formed at trailing edge, low or negative thrust. Weak leading edge vortex is starting to form for case B.

C Reverse Von Kármán street is forming, accompanied by a strong leading edge vortex. Highest thrust and efficiency is observed in Anderson's experiments.

D High thrust is generated, and two vortices per half-cycle are shed, low efficiency.

E Very small angle of attack, and thrust. No distinctive wake pattern.

F Very high angles of attack, "Piston Mode" appears, leading-and trailing-edge vortices form and roll up in the wake to form four vortices per cycle.

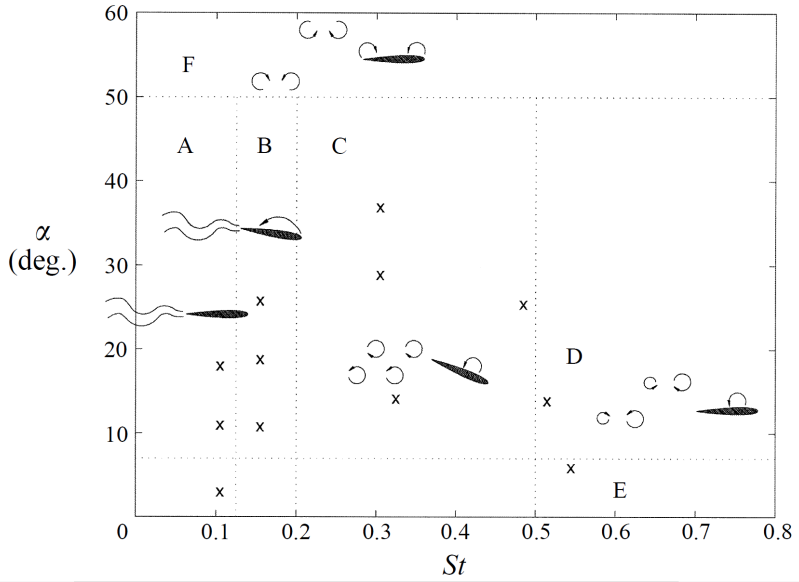

Figure 2.4: Wake patterns for an sinusoidal oscillating hydrofoil, as a function of Strouhal number (S_t), and maximum angle of attack (α_{max}). Courtesy of J. M. Anderson (1996).

Table 2.1: Test-range for motion parameters for optimisation runs at $Re_c \approx 40000$.

Parameter	min	max	Number of values
Strouhal number (S_t)	0.05	0.18	26
Yaw non-sinusoidal (K_θ)	-0.8	2.0	28
Sway non-sinusoidal (K_y)	-0.8	2.0	28
Phase-difference (ϕ)	45°	135°	90
Feathering (χ)	0.0	1.0	50
Sway amplitude (y^{amp}_{sway})	1.0	1.2	3

2.2.2 Test-Range of Parameters

A test-range for the motion parameters was selected, within this range the optimisation algorithm is able to select any combination freely. K_y, K_θ, and S_t were limited by the load on sway and yaw motors. Feathering parameter (χ) is set to be lower than 1, which according to Kinsey and Dumas (2008) will ensure that thrust is generated. Phase was set between 45° and 135°. The selection of parameter ranges is summarized in table 2.1 for $Re_c \approx 40000$, and in 2.2 for $Re_c \approx 19000$. Based on the number of values on all parameters, there can be 275 million different combinations for tests at $Re_c \approx 40000$.

Table 2.2: Test-range for motion parameters for optimisation runs at $Re_c \approx 19000$.

Parameter	min	max	Number of values
Strouhal number (S_t)	0.15	0.35	20
Yaw non-sinusoidal (K_θ)	-0.8	2.5	33
Sway non-sinusoidal (K_y)	-0.8	2.5	33
Phase-difference (ϕ)	45°	135°	81
Feathering (χ)	0.0	1.0	50
Sway amplitude (y^{amp}_{sway})	0.75	1.2	9

2.3 Genetic Optimisation Algorithm

> Genetic algorithms (GAs) are computer programs that mimic the processes of biological evolution in order to solve problems and to model evolutionary systems.
>
> *Melanie Mitchell*
> *(Mitchell, 1995)*

A genetic algorithm (GA) is used to select motion parameters during the test experiment. The algorithm is explained in the master thesis by Thomas Gjerde, and employed in the experiments in collaboration with him. In this section a brief overview of the method is given, based on the paper by Mitchell (1995). For more details refer to the master thesis by Gjerde (2017).

Evolution is an efficient method to search among enormous number of possibilities for solutions. Effective use of parallelism is achieved by searching for many different solutions simultaneously.

A GA is programmed using "bottom-up" paradigm, simple rules are used, from which complex behaviours emerge. The experimental parameters are decoded into a string of bits, which are comparable to a sequence of chromosomes in a population described with biological evolutionary theory. In this experiment the parameters with step-size given in section 2.2.2 are encoded as bit-strings. As an example we will decode the following values of Strouhal number, S_t, to a bit-string:

$$S_t = \{0.10, 0.125, 0.15, 0.175\} \tag{2.19}$$

The range of S_t in equation (2.19) can be encoded into 3 bits, which can be translated with the following relationship:

$$\begin{aligned} 000 &\longrightarrow S_t = 0.10 \\ \begin{matrix}100\\010\\001\end{matrix} &\longrightarrow S_t = 0.125 \\ \begin{matrix}110\\011\\101\end{matrix} &\longrightarrow S_t = 0.15 \\ 111 &\longrightarrow S_t = 0.175 \end{aligned} \tag{2.20}$$

In the same way all the other variables are decoded into a string of bits, the string of bits for each variable are then combined into a long string that describes the entire motion, also called the *individual*. The length of this string will be $\sum_0^V (N_v - 1)$, when V is the number of variables, and N_v the number of values for variable V.

Now that the parameters are represented as a bit-string, the GA-scheme is given according to Mitchell (1995) (with modifications on how it is implemented for the oscillating foil experiment):

1. Start with a randomly generated population of randomly generated N_{pop} individuals.
2. Run the experiments for each individual, and analyse it with the procedure described in Section 2.4, confirm that thrust (C_T) is within acceptable range, and tolerances for motion representation and precision error are met. Calculate the thrust efficiency (η).
3. Repeat the following steps (a)-(c) until N_{pop} offsprings have been created.
   (a) Select a pair of parent individuals from the current population, with the probability of selection being an increasing function of fitness (efficiency, η).
   (b) With probability p_c (the crossover probability), cross over the pair at randomly chosen points of the bitstring to form two offspring.
   (c) Mutate m_{rate} percentage of bits for the two offspring with a probability p_m for mutation, place the resulting genotypes into the new population.
4. Replace the current population with the new population.
5. Go to step 2.

Mitchell (1995) refers to each iteration of the scheme above as a "generation". A GA is usually repeated 50 to 500 generations, which is called a "run". As every run is started with a random generation, each run can achieve a slightly

dissimilar solution. Mitchell (1995) points out that researchers usually repeat runs and report statistics, which are averaged over many different runs of the GA. This will be an issue in experiments for this thesis, the test of each genotype or individual will take approximately 1 min. If each generation consists of 50 individuals, and 50 generations are done in each run, the run will last for at least 41 h. Instead of repeating the same run, different maximum or minimum limits on the thrust C_T are imposed, such that a continuous function for efficiency $\eta(C_T)$ can be established afterwards.

Individuals that are not accepted due to precision error, or wrongly represent the motion are retried, increasing the duration of a run even further. When an individual is discarded it is mutated iteratively with 20% until accepted.

To further reduce the time consumption, a registry of all tested and accepted individuals is created. During the evolution of several generations it is expected that the same genotypes will occur, and for these, no new experiment is conducted. Instead the result is read from registry. When the algorithm converges to a result, significant amount of individuals in a generation are fetched from the registry.

2.4 Data Acquisition and Analysis

The data is sampled at a rate of 200 Hz, all measurement channels are connected to the same data acquisition system (DAQ); HBM MGCplus. A 20 Hz-butterworth lowpass hardware filter is applied to all channels inside the DAQ. The coefficient matrix is applied to the strain gauge measurements to derive the forces F_x, F_y, and M_z.

Further analysis is done in Python after each oscillation test. All measurements except for force are filtered with a 16th order bandpass filter. To avoid numerical errors due to high filter order, cascaded second-order sections are used. The lowcut frequency is set to half of the oscillation frequency. Highcut frequency is set constant for all tests at 6 Hz, which is 6 times higher than the fastest oscillation frequency tested. Such a low highcut limit is used because of the eigenfrequency of the foil, which is at ≈ 10 Hz. The filter characteristic for both filters is illustrated in figure 2.5.

The force measurements are filtered differently because severe drift is noticed. The zero position is affected by the room and water temperature, due to strain caused by thermal expansion of the force transducer. At the start of each test the drag and lift forces are recalibrated. For each tested set of motion-parameters the foil is oscillated 20 times. At the beginning and end of motion, the angle of attack, α, is set to zero for 20 s. The mean drag value is measured, and a linear

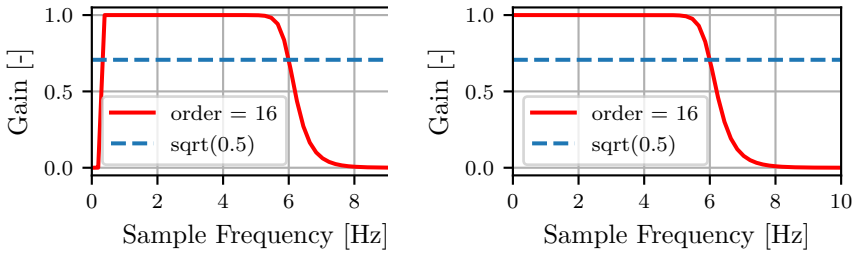

(a) Bandpass **(b)** Lowpass

Figure 2.5: Filter amplification characteristic for different sample frequencies.

correction is done to shift the force measurement to the correct zero-position. This is illustrated in Figure 2.6. The correct reference drag force is measured in the beginning of each optimisation experiment, usually every 24 hours. The normal force (F_y) and torque (M_z) is set to zero, because no lift and thereby torque is expected for a symmetric foil with zero angle of attack.

By plotting the drift correction (Figure 2.7) for a 24-hour cycle, something interesting was observed. The drift increased much during night, after $22:00$, and a large change was observed at $07:00$. This corresponds to when the air-condition was turned off and on to save energy, the water temperature can be increased with up to $2\,^{\circ}\mathrm{C}$ during one day when operating at high velocities. It is believed that this only has a minor impact on the results, in the future however one should ensure that the room is temperature-controlled.

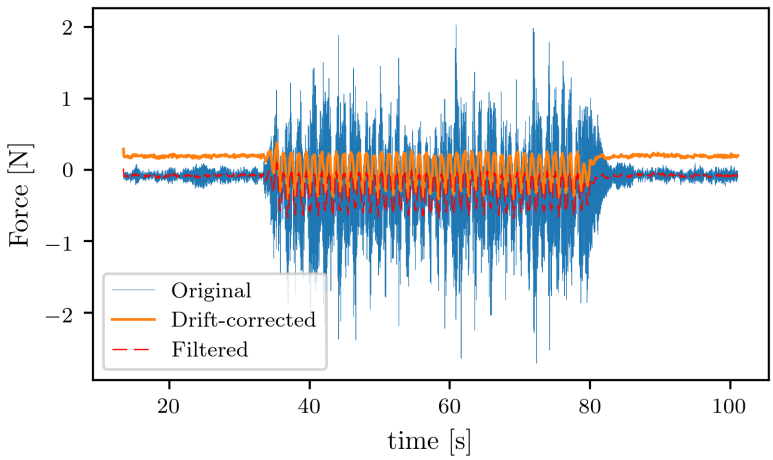

(a) Time-series of one individual test.

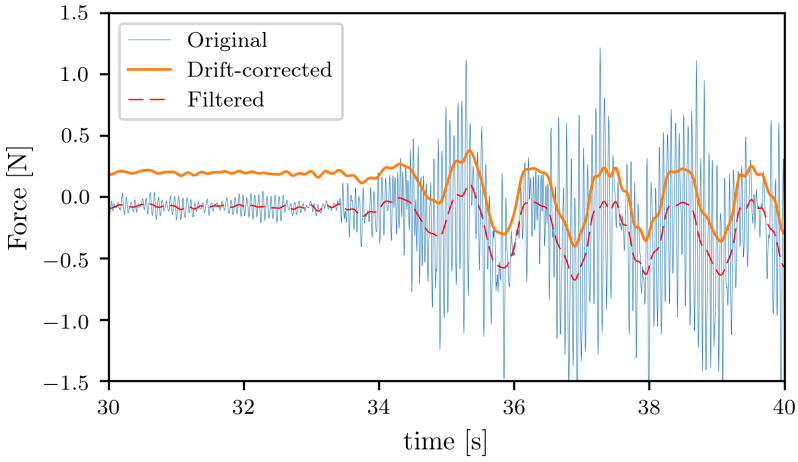

(b) Detailed view when oscillation motion is started, 2 oscillations are shown here.

Figure 2.6: Example on how the raw-data is filtered and corrected for drift. This shows the F_x force for a test done at $Re_c \approx 40000$ with motion parameters: $K_\theta = -0.18$, $K_y = 0.24$, $S_t = 0.16$, $\phi = 77.3°$, $U_{inf} = 0.527$, $\chi = 0.55$, $y^{amp}_{sway} = 1.2$.

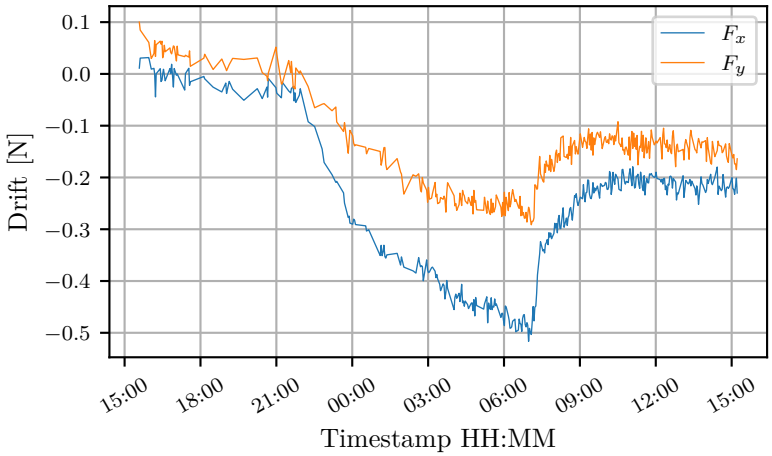

Figure 2.7: F_x and F_y sensor drift correction during a 24-hour optimisation-run. Note that the drift slowly increases at 22:00, and has a jump at 07:00, it is believed that this is due to the air-conditioning in the room. This example is for optimisation test number 7 in Table 3.3.

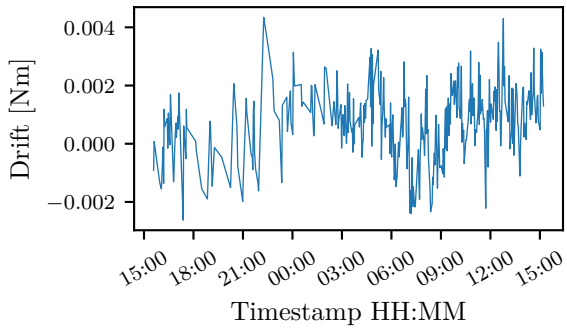

Figure 2.8: M_z sensor drift, no significant drift is noted for this. This example is for optimisation test number 7 in Table 3.3.

2.4.1 Motion Representation

At the end of every test, and before the results are accepted for an individual, it is checked that the motion is represented correctly. The original functions for sway and yaw (Equation 2.17 and 2.16) are fitted to the motion using least square method in Python. The fitted motion parameters are compared to the requested test-parameters, if the deviation is too high, the result is discarded. This typically occurred when forces on the sway and yaw motors are too high. For example when a high Strouhal number is tested together with a high non-sinusoidal K-parameter, the accelerations are very high due to high oscillation frequency, and square motion profile.

2.4.2 Precision Error

To evaluate if a measurement is acceptable the precision error is determined according to Steen (2014). For every set of parameters the foil is oscillated 20 times, the first and last 2 oscillations are disregarded for analysis. The mean value of the 16 oscillations is then calculated together with its precision error. If the precision error is above 5% the measurement is automatically discarded. The confidence-interval of a sample is then given by Equation (2.21).

$$\text{Prob}(X_j - t\,\sigma \leq \mu \leq X_j + t\,\sigma) = \gamma \tag{2.21}$$

where γ is the confidence interval, typically $\gamma = 0.95$. σ is the standard deviation for the gaussian distribution and is unknown for a finite number of samples. μ is the sample mean, and X_j the sample number j.

It is assumed that if the measurements are repeated infinitely, the results will follow a gaussian distribution. To describe the t factor for a finite number of measurements, a student-t distribution with $N-1$ degrees of freedom is used. Where N is the number of samples. Equation (2.21) can be rewritten to:

$$\gamma = \text{Prob}(-t \leq \frac{X_j - \mu}{S_x} \leq t) \tag{2.22}$$

$$t = F^{-1}(0.5(1+\gamma)) \tag{2.23}$$

Where $F^{-1}()$ is the inverse of the cumulative density function for the t-distribution, and S_x is the standard deviation of the measured series.

The relative precision error ($P_{\overline{X}}$) of the mean of N repetitions can now be found

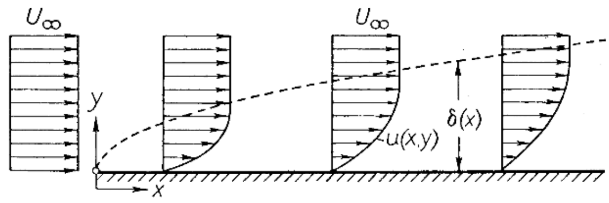

Figure 2.9: Boundary layer velocity profiles at a flat plate with zero incidence. Courtesy of Schlichting et al. (1960)

by:

$$P_{\overline{X}} = t \, \frac{S_x}{\sqrt{N}\mu} \tag{2.24}$$

2.5 Boundary Layer

The wall boundary layer of the circulating water tunnel (CWT) can affect the inflow velocity at the foil-tips. It is therefore important to estimate its thickness, both experimental and theoretical. A common definition of the boundary layer thickness is where velocity near the wall is above 99% of the inflow velocity, u_{inf} (Schlichting, Gersten, Krause, Oertel, & Mayes, 1960). There are two equations which can describe the boundary layer thickness. For a laminar boundary layer the Blasius equation can be used.

$$\delta_{blasius} \approx 5 \, x \, \sqrt{\frac{1}{Re_x}} \tag{2.25}$$

where $\delta_{blasius}$ is the boundary layer thickness, x the downstream position along a flat plate, and Re_x the Reynold number at the downstream position on the flat plate, defined in Equation 2.26.

$$Re_x = \frac{u_{inf} \, x}{v} \tag{2.26}$$

Here u_{inf} is the undisturbed inflow velocity, and v the kinematic viscosity of the fluid.

Transition to a turbulent boundary layer on a flat plate occurs approximately at $Re_x \approx 10^5$. The turbulent boundary layer thickness can be described with the following formula:

$$\delta_{turb.} \approx 0.14 \, \frac{v}{u_{inf}} \, \frac{Re_x}{\ln(Re_x)} \, G(\ln(Re_x)) \tag{2.27}$$

Table 2.3: Reynolds-number (Re_x) for different velocities at top and bottom of the tank where the foil will be placed in the experiment.

position / u_{inf}	Top	Bottom
$\approx 0.25\,\mathrm{m\,s^{-1}}$	$7.8e5$	$1.8e5$
$\approx 0.5\,\mathrm{m\,s^{-1}}$	$15.5e5$	$3.5e5$

where $G(\ln(Re_x))$ is weakly dependent on Re_x. According to Schlichting et al. (1960) this will be 1.5 for $10^5 < Re_x < 10^6$, and limit to 1.0 when $\ln(Re_x) \to \inf$. For experiments in the CWT two boundary layers are of interest. One at the tank top, and one at the bottom, here the foil tip interacts with the wall boundary layer. The distance x at tank-top, measured from the flow straighteners to the foil-model, is 3.1 m. At the bottom plate a boundary layer can build over a distance $x \approx 0.73\,\mathrm{m}$. Table 2.3 gives an overview of the Reynold numbers that will occur during the experiments at the tank top and bottom. For both test-velocities a laminar boundary layer would be expected on the bottom. Because of the long distance from the flow straightener to the test-section a transition or turbulent boundary layer is expected at the top for both velocities.

2.6 Scaling from Model- to Full-Scale

Yamaguchi and Bose (1994) did a study on propulsion efficiency by linear and non-linear theory of a $200,000DWT$ Tanker equipped with harmonically oscillating hydrofoil. Their estimate on foil dimensions can be used as an indication of the Reynold number in full-scale. The tanker is set to travel at 14 knots, with a foil chord length of 7 m and sea water at 15 °C with a kinematic viscosity $1.1988 \times 10^{-6}\,\mathrm{m^2\,s^{-1}}$. The Reynold number for this operation condition will be $Re_c = 42 \times 10^6$. For foils with $Re_c > 1 \times 10^6$ the boundary layer is typically fully turbulent (Shyy, Lian, Tang, Viieru, & Liu, 2007), below this Reynold number transition from laminar to turbulent boundary layer flow can occur. This can cause early stall, and formation of laminar separation bubbles. Which in return affects the performance with respect to drag and lift, and makes the comparison between model and full-scale difficult.

2.6.1 Low Reynold Number Effects

Issues for model-scale experiments on hydrofoils has been discussed in the authors project thesis during the autumn semester 2016 (Bösch, 2016), and is summarized in this subsection. All the literature found focuses on effects that occur at static

angle of attacks at low Reynold number ($Re_c < 100000$). It is therefore unknown how dynamic motions would affect the formation of laminar separation bubbles, expectedly it has some impact on the hydrodynamic forces. In addition would a investigation of low Reynold number effects at unsteady flow conditions be a thesis of its own.

Laminar Separation Bubbles

Foil experiments at very low Reynolds number can introduce laminar separation bubbles (LSB). It causes the flow around the foil to change, and therefore it influences the hydrodynamic performance. The separation bubbles can form at low angles of attack, and can cause early stall (Arena & Mueller, 1980).

Separation bubbles occur when the laminar boundary layer separates from the surface, and reattaches further downstream. Mueller and Batil (1982) describes that separation bubbles occur when there is a strong adverse pressure gradient downstream of the point of minimum pressure. The flow will reattach when the pressure is nearly equal to what it would be if there had been a turbulent boundary layer. In Figure 2.10a the streamlines around a LSB forming near the leading edge are illustrated, S denotes the separation point, and R the reattachment point. The length of the LSB is defined as the distance between S and R. Arena and Mueller (1980) points out that that the presence of a LSB can be seen in the pressure distribution along the foil chord, which is illustrated in figure 2.10b, one line for a foil with turbulent boundary layer, and one where a LSB occurs, separation and reattachment points are indicated as S and R.

There are several factors which affect the formation and extend of LSB, Mueller and Batil (1982) summarizes the main factors as thickness of boundary layer at separation, angle of attack, free-stream turbulence level, and surface roughness. In experiments for this thesis, the latter three factors can be manipulated to reduce the extend of LSB.

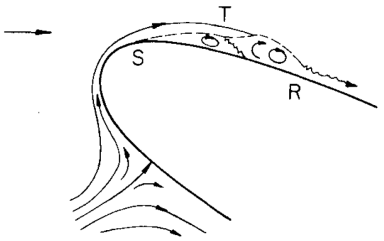

(a) Streamlines around a LSB forming at the leading edge. S denotes the separation point, and R the reattachment point.

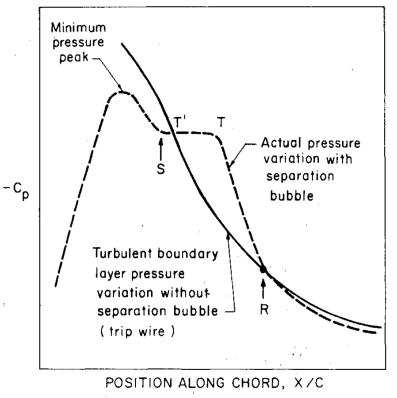

(b) Typical pressure distribution around a foil with the presence of a LSB.

Figure 2.10: Illustrations for a laminar separation bubble. Courtesy of Arena and Mueller (1980).

Static Stall Hysteresis

When a foil is operating near stall a hysteresis effect occurs in the lift and drag characteristics. The lift and drag is dependent on whether the angle of attack (AoA) is decreasing or increasing. At low Reynolds numbers this will even occur in a very slow or quasi static change in yaw angle. Carmichael (1981) reported that this static hysteresis effect can typically be observed in a Reynold number range of $Re_c \approx 30\,000$ to $500\,000$.

An illustration of a typical hysteresis loop for a static change in AoA is given in Figure 2.11. The figure is taken from Yang, Igarashi, Martin, and Hu (2008), the lift and drag forces are based on pressure measurements at the foil surface. Stall occurs at either 13° or 16° based on whether the angle of attack is increasing or decreasing. This deviation is attributed to that with increasing AoA the streamlines are still attached to the foil surface, which is not the case for a decreasing AoA.

Deadband

According to Selig, Guglielmo, Broeren, and Giguère (1995), at Reynold number below $Re_c \approx< 150000$ symmetrical airfoils can have a non-linear relation between lift and AoA, this is illustrated in Figure 2.12. Further they argue that for some extreme cases the lift-slope can become negative at small angles, his findings are

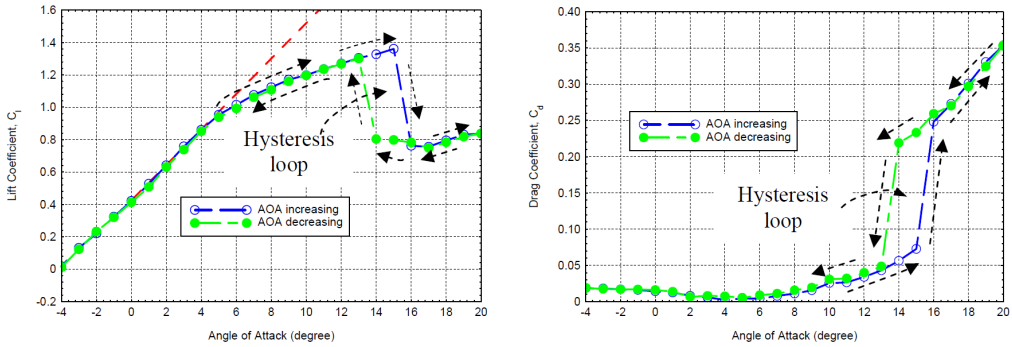

Figure 2.11: Static stall hysteresis loop observed in the lift and drag coefficient measurements by Yang et al. (2008). These experiments were done for a `GA(W)-1` airfoil at a Reynold number of $Re_c = 160000$ and a inflow turbulence intensity of 1%.

based on experiments of over 200 air-foils at low Reynold number in the wind-tunnel at The University of Illinois.

Selig et al. (1995) also tested if the deadband region could be completely eliminated by applying a zig-zag boundary layer trip. The trip is applied at 25% chord, with a trip-height of 0.32% chord the deadband was completely removed between Re_c =60 000 to 100 000. At $Re_c = 40000$ some non-linearity was still present. It should be noted that inflow turbulence plays an important role, it is therefore not granted that the same performance will be achieved in the experiments for this thesis in the circulating water tunnel (CWT). The wind-tunnel used in Seligs tests has very low turbulence, measured below 0.1%. The circulating water tunnel (CWT) at NTNU has a reported turblence level by its manufacturer, Engineering Laboratory Design, of 1% at maximum operating velocity $U_{inf} \approx 1$. Higher turbulence should contribute to smaller separation bubbles, and thereby less non-linearity.

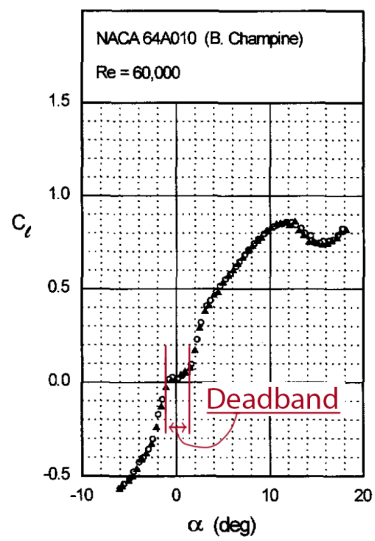

Figure 2.12: Deadband region illustrated for a NACA64A010 at $Re_c = 60000$ based on experimental results. Courtesy of Selig et al. (1995).

Laminar-Turbulence Transition

Laminar to turbulence transition can occur naturally, or be enforced by a sharp change in geometry; a boundary layer trip. The dimensions of this trip is crucial to ensure low induced drag, and elimination of laminar separation bubbles. In Selig et al. (1995) experiments, the trip-height is based on the method described by Braslow and Knox (1958), and the position on simulations done in XFOIL (Drela, 1989), how these methods are used is discussed in Section 3.5.1. XFOIL is a 2d vortex panel program, especially designed for low Reynold number foils, and is used to determine the location of a LSB, to ensure its effectiveness the boundary layer trip has to be place upstream of the LSB.

2.6.2 Theoretical Drag

There are several empirical methods to determine the drag of an airfoil profile in a turbulent boundary layer. These methods are typically only valid for very high Reynold numbers $Re_c \approx> 500000$. The skin friction is first determined by a friction-line method. An widely employed method is the ITTC-75 formulation, which is based on empirical data. The skin friction is dependent on the Reynold number only:

$$C_f = \frac{0.075}{(\log_{10}(Re_c) - 2)^2} \tag{2.28}$$

where C_f is the skin friction, and Re_c the chord Reynold number.

Some corrections must be made to the skin friction to account for the drag generated by the foil thickness (Hoerner, 1965). First the mean velocity along the foil surface will be higher than inflow velocity, this is proportional to t/c, where t is the foil thickness, and c the chord length. Additionally will the pressure affect drag, this scales with $(t/c)^4$. To describe this, Hoerner uses empirical data. The three drag components; pressure, profile, and friction, can be summarized to the total drag coefficient C_{DS}.

$$C_{DS} = 2\, C_f \left(1 + 2\, \frac{t}{c} + 60\, (\frac{t}{c})^4\right) \tag{2.29}$$

The method described by Hoerner has been used instead of the more common ITTC-1978 formulation for propeller open water-tests. The ITTC-1978 method is only valid if the model tests are conducted at $Re_c > 2e5$ (ITTC-1978, 2008), much than what is expected for the experiments in this thesis. Equation (2.29) will be used to correct the force coefficient in parallel direction to the foil F_x (figure 2.2)

at a steady angle of attack of $\alpha = 0$. This will not be accurate, but will give an indication on how high F_x forces would be expected in full-scale.

The drag coefficient for the full-scale oscillating foil described by Yamaguchi and Bose (1994), is calculated to $C_{DS} = 0.00631$ with Equation 2.29. This is for chord Reynold number $Re_c = 42 \times 10^6$. This value can be used to correct the drag measured in model-scale.

Chapter 3

Experimental Set-up and Methods

In this chapter it is discussed how the oscillating foil experiments are set-up. It also covers measurements that are done to confirm correct conditions for the optimisation experiments, concerning turbulence stimulation, laser doppler velocimetry (LDV) measurements of the boundary layer, and confirmation of correct inflow-velocity.

3.1 Equipment

The experiments are conducted in a circulating water tunnel (CWT), located at NTNU campus Tyholt. The tunnel consists of a 609 mm times 609 mm test-section which is 2500 mm long. Upstream a series of mesh grids are used to create a near laminar inflow condition, combined with a contraction ratio of 6:1, a turbulence intensity below 1 % is achieved. This has been confirmed by LDV measurements.

To conduct foil experiments with a flow similar to 2D an extra bottom plate is used. Such that the foil span is equal to the test section height. Water is allowed to pass over and under the plate. The plate and foil inside the test section is illustrated in Figure 3.2.

Periodic motion in sway and yaw are created with equipment lent from John Martin Kleven Godø, which has been used in similar experiments for his doctoral thesis. Modifications to the real-time control algorithm in LabView were made to allow for automation of the experiments and non-sinusoidal motions as described with Equations (2.17) and (2.16).

The foil oscillator consists of two electrical motors. A Rexroth motor is used to drive a carriage via a belt-pulley system, this creates the sway motion. Inside the carriage a JWL motor is mounted parallel to the foil centre-axis, and drives its yaw rotation through connecting rods. Part numbers of all devices are summarized in table 3.1.

Force measurements are done with multiple strain gauges mounted to a weakened circular section on the main shaft. This section is placed as close to the foil as possible to ensure low measured inertial forces. A matrix calibration was done

Table 3.1: Summary of essential parts used in the foil-rig (Motors, sensors, and controllers).

Device	Manufacturer	Part Number
Sway Motor	Rexroth	MKD041B-144-KG0-KN
Yaw Motor	JVL	MPA2020S0009
Motion controller	National Instruments	NI-cRIO-9030
Sway position sensor	ASM	WS10-1250-R1K-L-10-SB0-D8
Accelerometers	MARINTEK	unknown
Yaw angle sensor	TT Electronics	3381R1KL.5
Data Acquisition	HBM	MGCplus

after all bolts which can cause strain are tightened. In this experiment the forces in x and y-direction (F_x & F_y) and bending moment around center-axis (τ_z) are used.

To calculate the energy consumption, position and acceleration for both sway and yaw has to be measured. One accelerometer is placed inside the wagon, and one on the pivot arm which rotates the foil. A potentiometer is used to measure the yaw angle. The sway position is measured with a "Wire" position sensor. The calculation of power consumption and thrust coefficient is discussed in Section 2.1.1.

3.2 Automation

Through this master thesis an automation system for the experiments is developed in corporation with Thomas Gjerde. Everything must be automated such that one only has to start the optimisation run, and return next day.

In Figure 3.4 a flowchart is given, this illustrates how the three major components in the automated system interact. Three individual systems are running simultaneously: Python on a desktop computer for optimisation and data-analysis; LabView on a micro-controller (CompactRIO) which controls the foil motion and timing; and a measuring amplifier and data aquisition unit from HBM.

Torgeir Wahl, who is an electrical engineer for NTNUs laboratory staff, has helped significantly in developing this automated system.

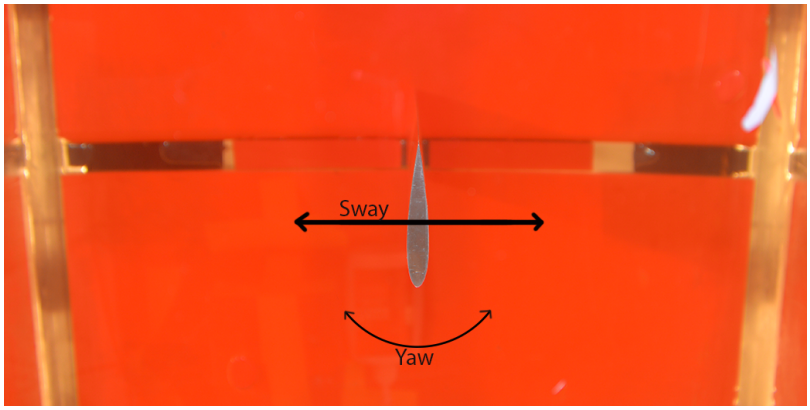

(a) Foil seen from below with its two degrees of freedom indicated

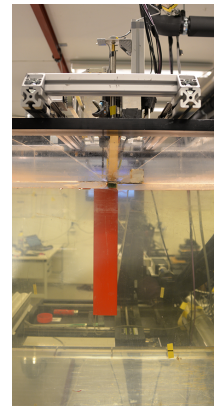

(b) Side view

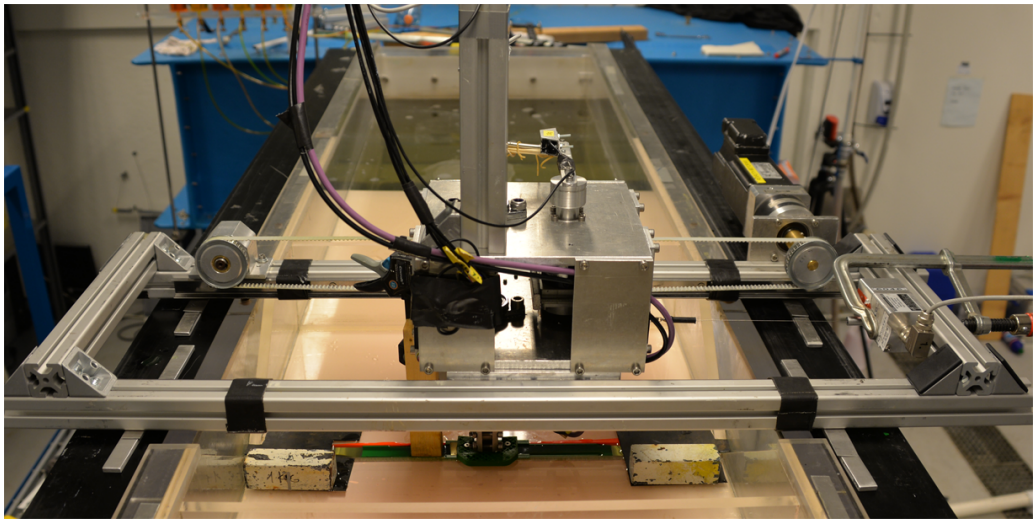

(c) Front view of the wagon that moves on rails to create a sway motion on the foil

Figure 3.1: Illustrations of the foil oscillator installed in the circulating water tunnel (CWT) laboratory at NTNU.

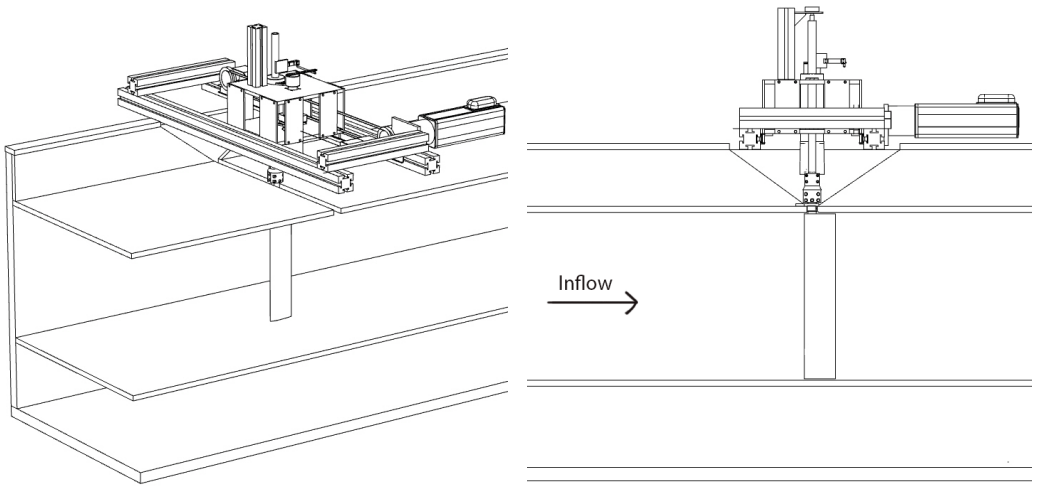

(a) Isometric view with side-wall removed **(b)** Side-view

Figure 3.2: CAD-sketches of the foil oscillator rig mounted inside the water tunnel. Courtesy of John Martin Kleven Godø.

3.2.1 Python

Python is used as a backbone for the system, everything is controlled from the desktop computer which runs the GA-optimisation code. When a new individual is tested, the GA-optimisation code communicates the 6 motion-parameters with the CompactRIO through an application programming interface (API) via a local area network (LAN) connection. After a short delay the trigger-signal to start the motion is sent, also through API.

After the CompactRIO is done with running the experiment for the individual and the data aquisition unit has saved a result file, python is used to post-process the measurements to determine efficiency (η) and thrust (C_T). Beforehand the data is filtered and checked if limits for precision error and motion representation are satisfied, as described in Section 2.4. If the precision error is too high, the number of oscillation is doubled, and it is tested again. If it fails again, the individual is discarded.

The GA-optimisation code takes over again, and adds the result to the current population. The tested parameters of the individual and its efficiency and thrust are saved in a *.csv* log-file. Afterwards a new individual is tested, and the cycle is repeated. If an individual has been tested before, the results are fetched from the *.csv* log-file, this is done to reduce the duration of a optimisation run. This cycle will continue until aborted by the user, which is done if most of the individuals are fetched from memory, indicating a converging result.

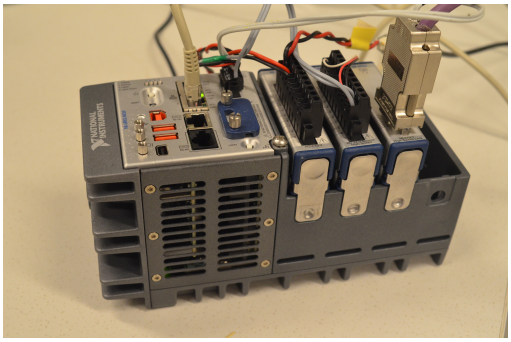

(a) CompactRIO (cRIO-9030) from National Instruments, which runs the LabView program to control sway and yaw motion, and data aquisition trigger.

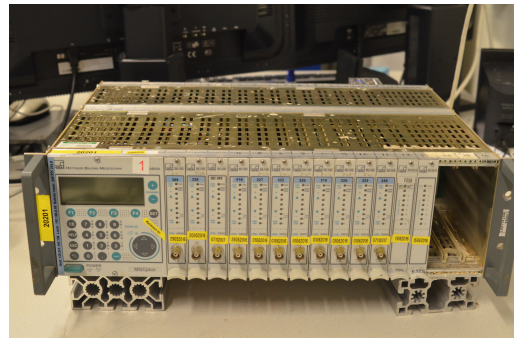

(b) Measurement amplifier, and data acquisition unit (HBM MGCplus).

Figure 3.3: Instruments used for motion control, and data acquisition.

3.2.2 LabView and CompactRIO

When motion-parameters are passed to the CompactRIO from python, LabView generates the motion for one period, and saves it in memory as an array. To represent the yaw motion correctly, the motor-controller needs information on both yaw-angle and -acceleration. Yaw-acceleration is determined through numerical differentiation in LabView, the acceleration is also stored as an array.

Once a start-signal is given by Python through API, LabView initiates the test, and triggers a new measurement-series at the data acquisition unit through an analogue signal. First a steady yaw angle at 0° is held for 20 s, this information is later used to correct sensor-drift by setting a new zero position for force-measurements. To avoid mechanical overload the motion amplitudes are slowly ramped up. Subsequently 20 oscillations are done, and then ramped down. Finally the foil is again held at a steady 0° yaw angle for 20 s, this information is used to confirm that the strain-gauges have not drifted during the test. The data acquisition is stopped through an analogue signal, and the measurements are saved to a file and sent to the desktop computer via LAN communication, here the results are analysed with Python, as described in the previous section.

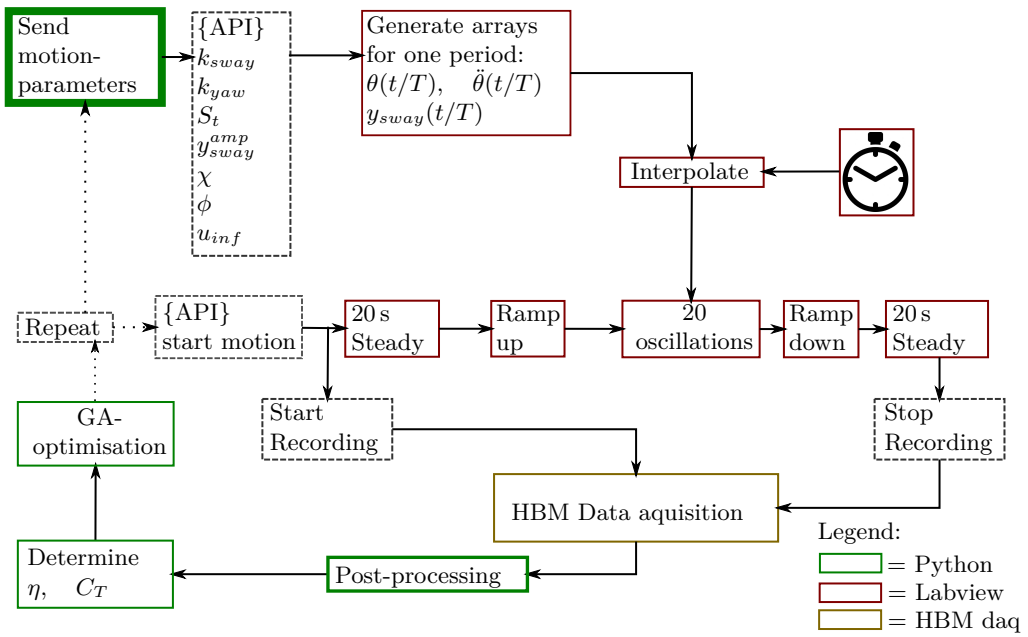

Figure 3.4: Flowchart illustrating how the optimisation run is automated, indicating the communication between 3 major components. Python is running on a desktop computer, it communicates through API to a CompactRIO which runs the LabView program. The HBM data aquisition unit is triggered through analoge signals from the CompactRIO/LabView. The HBM sends measurement files to the desktop computer after each test through Local Area Network (LAN) communication.

3.3 Vibrations in the Set-up

Vibrations are observed when the foil is at a static yaw angle, this behaviour is mapped to investigate if and how it will affect measurements.

Natural frequency of the foil is determined through a decay test. To include added mass from water, the foil is submerged in water, and assembled equal as in the optimisation experiments. The foil is then hit with a hammer, and the force in that direction is recorded, this is done in y- and x-direction. Natural frequency is then determined through the power spectrum, which is created with a fast fourier transformation. In Figure 3.5 the time-history and power spectrum of F_x and F_y is illustrated.

It is observed that the natural frequency is low, 9.7 Hz in y-direction, and 15.1 Hz in x-direction. Dissimilarity in direction is expected due to difference in added mass. To set the values in perspective, the highest oscillation frequency will be up to 1 Hz, which should not cause a resonant excitement.

Ideally the natural frequency should be much larger than the operating frequency, it can be changed by either changing the mass or stiffness of the system. Both are difficult to change because the stiffness is defined by its softest member, which is the force transducer. If the mass of the foil is reduced, so will its stiffness. The only way to significantly increase the natural frequency would be to either suspend the foil from both ends, or use a transducer with a much higher stiffness. One could for example use piezoelectric transducers, which rely the measurement on deformation of a crystal instead of steel.

During the static tests where the lift and drag is determined for a set of fixed yaw angles, it was observed that the foil vibrates in y-direction. This behaviour would only occur at small angles of attack $\alpha < 4^\circ$, and is very dependent on the inflow velocity. These tests were systematically conducted at the entire possible range of inflow-velocities. In Figure (3.6) the mean lift coefficient C_l and its standard deviation $\sigma(C_l)$ is plotted. The figure indicates that this behaviour occurs at $22500 \leq Re_c < 74500$. Based on this, two different test-conditions were chosen, one at $Re_c \approx 19500$ or $u_{inf} \approx 0.25\,\mathrm{m\,s^{-1}}$, and one at $Re_c \approx 40000$ or $u_{inf} \approx 0.525\,\mathrm{m\,s^{-1}}$. The latter one was chosen because literature described in section 2.6.1 indicates that this Reynold number is approximately the lower limit where turbulence stimulation can be achieved, in is this the same as in the experiments by J. Anderson et al. (1998), and Read et al. (2003), this will make it easier to compare results.

When the static tests were repeated at $Re_c \approx 40000$ with and without turbulence-stimulation (TS) it was recognized that the vibration problem has completely

disappeared. The power spectrum is indicated for $\alpha = 1.8°$ in Figure 3.7, the test with TS has only one large peak at 0 Hz which indicates a steady mean value. The test without TS has a peak at 9.7 Hz, which is the natural frequency, indicating resonant behaviour. This is observed for the entire range of yaw angles.

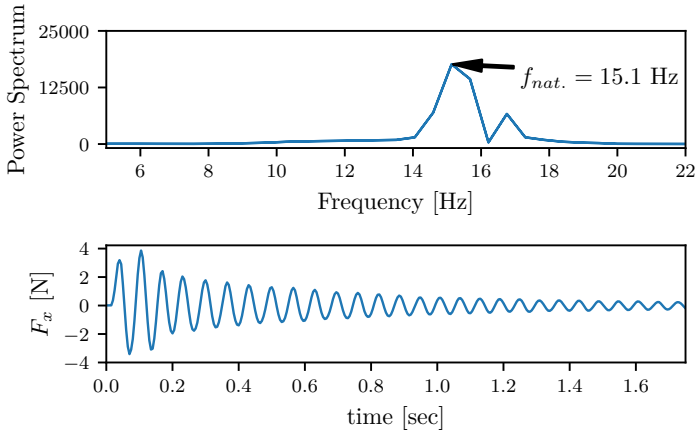

(a) F_x

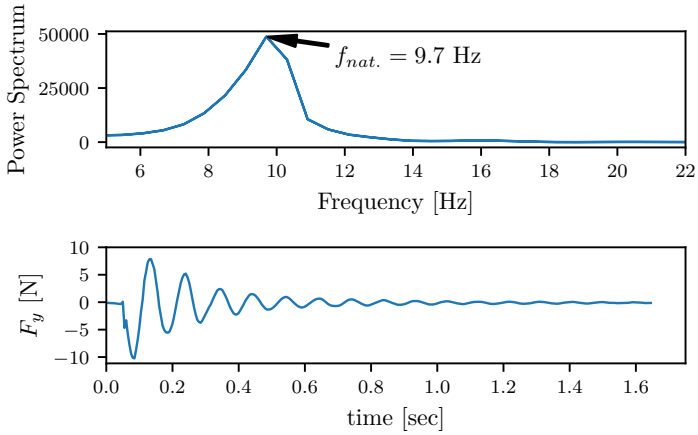

(b) F_y

Figure 3.5: Timeseries, and fourier spectral analysis from the decay tests. One test is done in each direction. The foil is hit with a hammer while submerged in water with the extra bottom in place, and foil-rig fixed to the tank-top. The natural frequency $f_{nat.}$ is indicated in the figures.

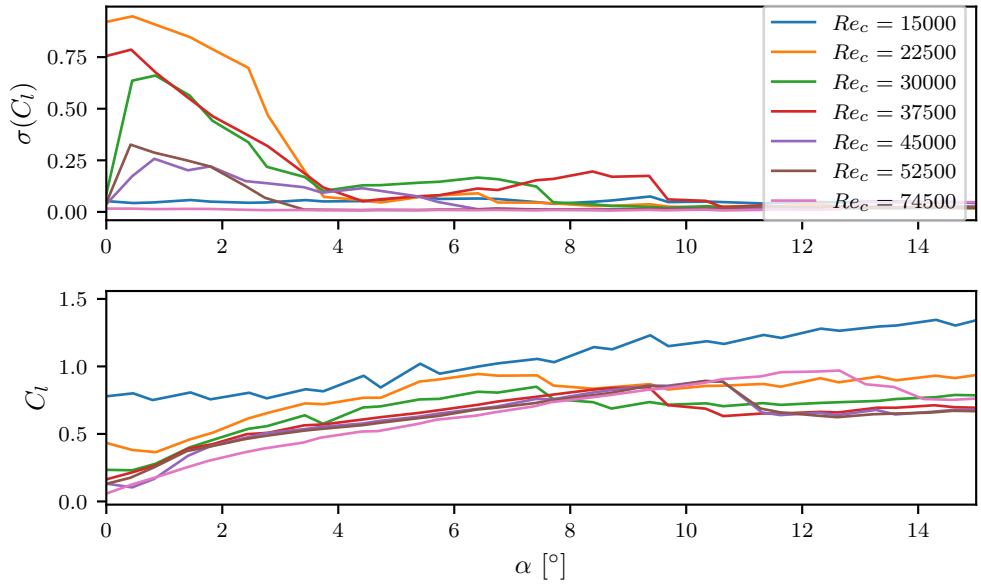

Figure 3.6: Lift coefficient (C_l) and time varying standard deviation of lift ($\sigma(C_l)$) at different static angles of attack. Static tests are done at several different inflow-velocities, or Reynold number Re_c. The lower plot shows the measured lift coefficient for different angle of attacks, and the upper plot the standard deviation of the measured lift coefficient. When a high standard deviation is given, the foil is resonated at the natural frequency in y-direction $f_{nat.} = 9.7\,\text{Hz}$. These tests are used to determine on which velocities optimisation experiments should be conducted. The Reynold number corresponds to the tested velocities of $u_{inf} = \{0.2, 0.3, 0.4, 0.5, 0.6, 0.7, 1.0\}$.

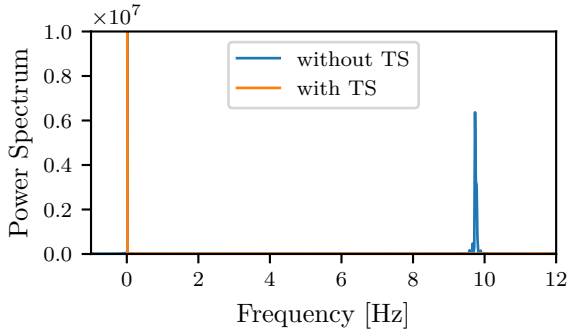

Figure 3.7: Power spectrum from static test at $\alpha = 1.8°$with $Re_c \approx 39200$. Tests done with and without turbulence stimulation (TS).

3.4 Force Transducer Verification

Beforehand of the experiments the force transducer calibration is checked. This is done by tilting the foil shaft horizontal, and suspending weights at the foil centre. Measured force and applied weight is then compared. Both force measurements in y- and x-direction are checked. The measured force versus applied load is illustrated in Figure 3.8. Up to 36 N, F_x and F_y are within 1% deviation from the actual measured value, above 48 N, F_y deviates significantly. One must assume that force measurements below 27 N are also linear. This is expected because the force is measured through strain-gauges which record the deformation of a steel-pipe. Basic mechanics tells us that a material deformation is linear before yield, and with small applied loads. In addition was the transducer calibrated when it was built a year ago, where also the lower measurement-range was checked. Any damage to either the strain-gauges or steel-pipe would be reflected in a significant error in the measured force.

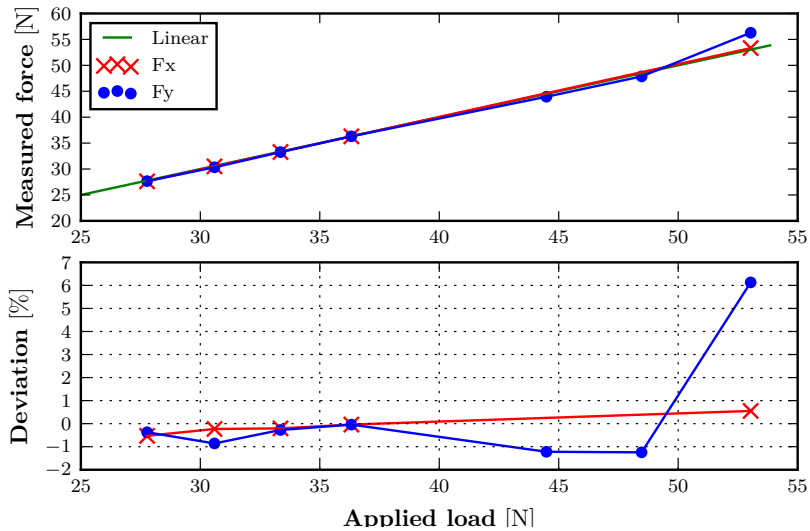

Figure 3.8: Measurements for the force transducer verification. Deviations are within 1% up to a measured force of 37 N. Linearity is assumed for forces below 27 N.

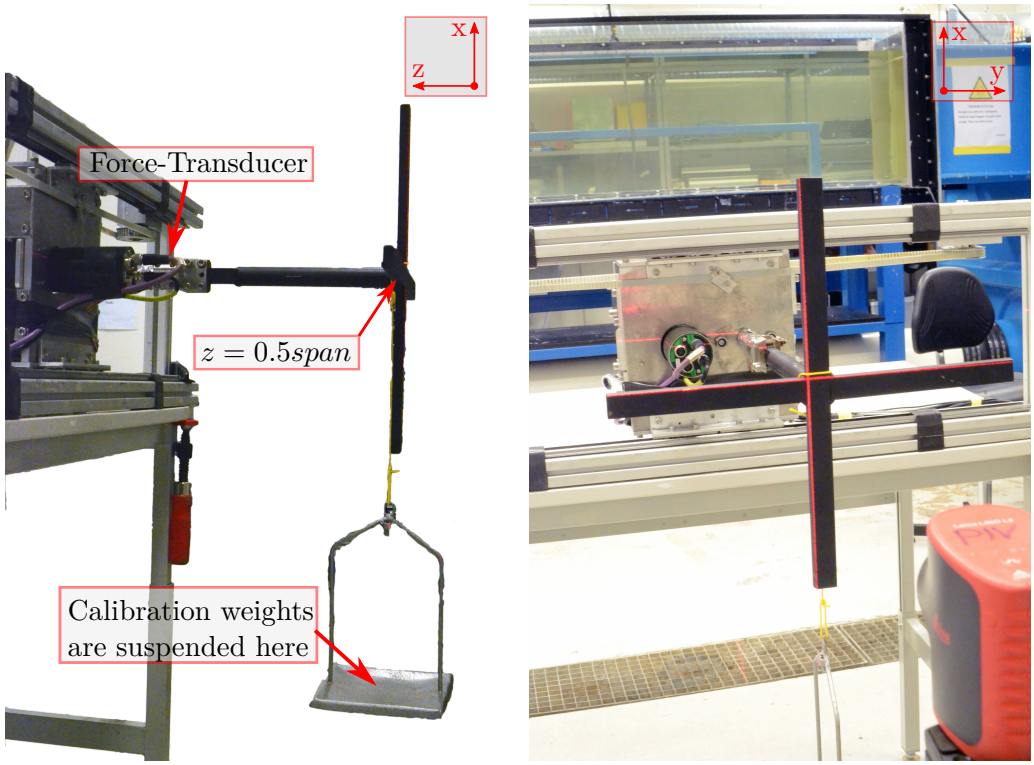

(a) Calibration weights are suspended at $z = 0.5s$, where also the center of force in the experiment is expected.

(b) A laser spirit level is used to verify that load is applied in the correct direction.

Figure 3.9: Set-up for **force transducer verification**. The foil-rig is tilted 90°, in picture **(b)** the carriage and rails are seen from underneath, a calibration cross is fitted to foil-shaft instead of the foil.

3.5 Test-Conditions

The achievable oscillation frequency is limited by equipment. The Strouhal number is highly dependent on inflow velocity and oscillation frequency. At a too low Reynold number (Re_c) or inflow velocity, scale effects occur due to laminar separation bubbles (LSB). Optimisation experiments are therefore conducted at two conditions: at $Re_c \approx 19000$, where the scale effects are severe but high Strouhal number is achieved ($S_t < 0.35$); and at $Re_c \approx 40000$, where the Strouhal number is low ($S_t < 0.18$) and scale effects are minimal. To reduce the scale-effects even further, a boundary layer trip in accordance to Braslow and Knox (1958) is utilized at $Re_c \approx 40000$, as discussed in Section 3.5.1, the drawback is increased skin friction.

At $Re_c \approx 40000$ two seperate optimisation tests are done: one where a sinusoidal motion is enforced by setting the K-paramater to 0; and the other where a wide range of K is accepted. This will give a direct comparison whether there is a significant performance improvement by using non-sinusoidal sway and yaw motions.

3.5.1 Turbulence Stimulation

The extent of a LSB under different flow-conditions is simulated with XFOIL (Drela, 1989). The Reynold number for the experiments is set to $Re_c \approx 40000$, for which Selig et al. (1995) was able to reduce the deadband at low angles of attack with turbulence stimulation (TS).

In Figure 3.10 the position of a LSB on the foil is indicated. The LSB extends from the separation- to the reattachment-point. Simulations are repeated for different N_{crit} values, the N_{crit} value dictates how easy transition from laminar to turbulent boundary layer occurs. Van Ingen (2008) argues that if one simplifies that only inflow-turbulence affects the N_{crit} value, it can be equal to the empirical relationship in Equation (3.1).

$N_{crit} = 2.82$ corresponds to 1% inflow turbulence intensity, equal to what is measured in the circulating water tunnel (CWT) used for experiments in this thesis. Higher N_{crit} values are included in Ffigure 3.10, which corresponds to a lower inflow turbulence intensity. This is done to investigate the sensitivity for other N_{crit} values. Based on Figure 3.10 the boundary layer trip can be placed at $x/c = 0.1$. There it will be effective for an AoA up to 6-8° dependent on the inflow turbulence or N_{crit}.

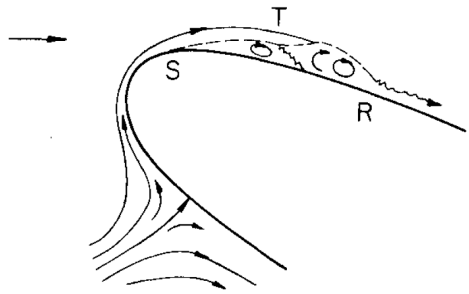

(a) Recap on laminar separation bubbles (LSB), S denotes the **separation** point, and R the **reattachment** point. Courtesy of Arena and Mueller (1980).

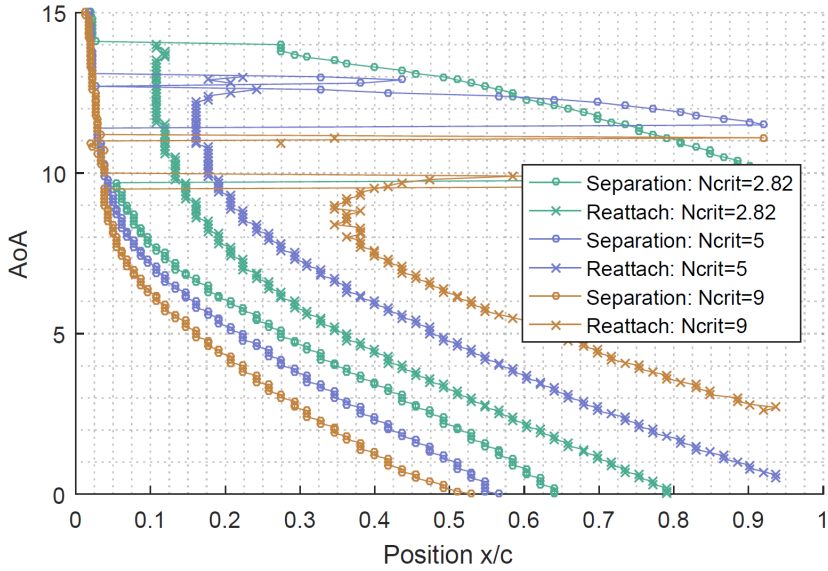

(b) Simulated reattachment and separation point for varying angle of attack.

Figure 3.10: XFOIL simulations on size of laminar separation bubbles (LSB) at $Re_c \approx 40000$ for a NACA0015 foil, different N_{crit} values describe a difference in inflow turbulence, $N_{crit} = 2.82$ corresponds roughly to the conditions in the circulating water tunnel (CWT) at NTNU. A LSB exists between the separation and reattachment position, and moves its location with the angle of attack (AoA). This result is used to find a position along the foil chord (x/c) for the turbulence stimulation, which would be ineffective if it's placed inside a LSB.

Table 3.2: Height for a zig-zag and sand grain boundary layer trip located at $x/c = 0.1$ and operating at $Re_c = 40000$, calculations are done according to the method described by Braslow and Knox (1958).

Trip type	Re_{crit}	Re_x	η_{2d}	min. height [mm]
Zig-Zag	200	4000	1.7	0.4
Sand grain	600	4000	4.2	1

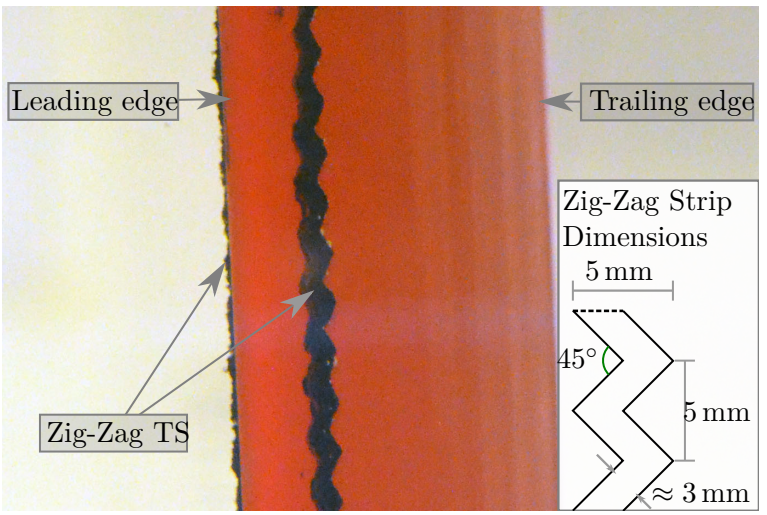

Figure 3.11: Illustrations of the turbulence stimulation, the foil is rotated in yaw, and the camera is looking at the leading edge.

$$N_{crit} = -8.43 - 2.4 \ln(T) \tag{3.1}$$

where T is the turbulence intensity level.

By using the method described by Braslow and Knox (1958) the trip height for the conditions described above is calculated. The calculation is done for a zig-zag trip which requires a critical roughness Reynolds number of at least $Re_{crit} > 200$ (Van Rooij & Timmer, 2003), and granulated sand which requires $Re_{crit} > 600$ (Braslow & Knox, 1958). The calculations are summarized in Table 3.2.

Due to time limitations in the experiments, only one configuration could be tested, and to be sure a successful turbulence stimulation is achieved a thicker trip (0.9 mm) than necessary is used. The Zig-Zag strip is cut out of *3M SafetyWalk* adhesive tape, which has a rough surface. In Figure 3.11 a picture with the boundary layer trip adhered to the foil is given, the dimensions are also illustrated. The middle of the Zig-Zag strip is placed at $0.1c$ measured from leading edge. Static lift measurements presented in section 3.6.1, confirm that the boundary layer trip is successful.

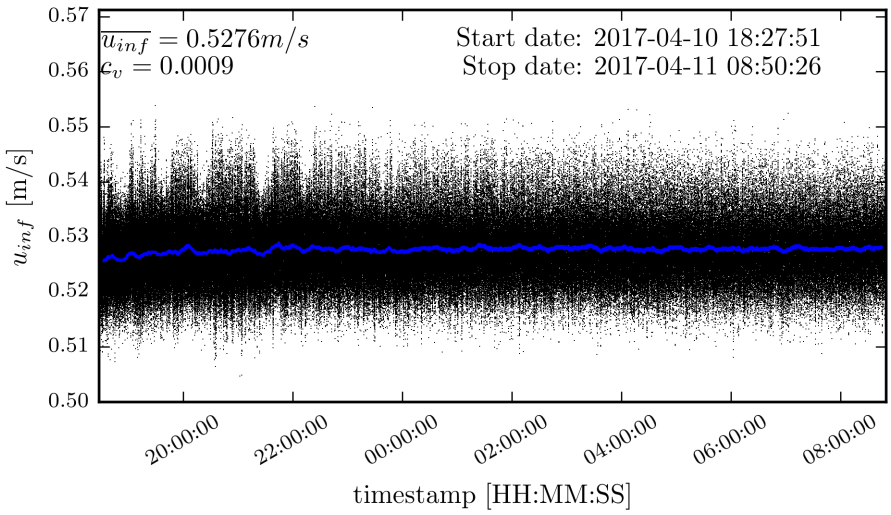

Figure 3.12: 10 min-moving average velocity, and scatter plot of time samples with laser-doppler-velocimetry (LDV) measurement series. This LDV measurement was done during test number 6, described in Table 3.3.

3.5.2 Inflow Velocity

A Laser-doppler-velocimetry (LDV) device is used to measure the inflow velocity during all experiments. The LDV measures the velocity of small hollow glass spheres, which are seeded into the water. They are neutrally buoyant in water, such that no vertical velocity is induced due to buoyancy. The LDV measures velocity of the spheres when they pass the laser probe. A sample is taken each time the glass sphere passes the probe, resulting in a irregular sampling frequency. To compensate for this the data is re-sampled using linear interpolation, with a fixed sampling frequency. Which corresponds to the mean sampling frequency of the entire series. To evaluate the long term variations, a moving average is taken with a 10 min window size.

The idea is to confirm that the inflow velocity (u_{inf}) during the measurement is within reasonable limits. For this the statistical parameter, coefficient of variation (c_v) is used. It is determined from the moving average.

$$c_v(u_{inf}) = \frac{\sigma(u_{inf})}{\overline{u_{inf}}} \tag{3.2}$$

Where $\overline{u_{inf}}$ is the mean inflow velocity, and $\sigma(u_{inf})$ its standard deviation.

Table 3.3: Inflow velocity measured with LDV, and water-temperature for all AI optimisation experiments.

Test-nr.	$\overline{u_{inf}}$	$c_v(u_{inf})$	Duration	Water Temperature		Note
				at start	at end	
1	0.2488 $\frac{\text{m}}{\text{s}}$	–	≈ 28 h			LDV crashed, $\overline{u_{inf}}$ based on 3 min measurement
2	0.2512 $\frac{\text{m}}{\text{s}}$	0.0025	≈ 18 h	21.9 °C	22.0 °C	
3	0.2542 $\frac{\text{m}}{\text{s}}$	0.0063	≈ 10 h	19.0 °C	19.8 °C	$C_T > 0.5$
10	0.2515 $\frac{\text{m}}{\text{s}}$	0.0026	≈ 10 h	22.3 °C	22.3 °C	$C_T < 0.4$
4	0.5276 $\frac{\text{m}}{\text{s}}$	0.0008	≈ 17 h	20.0 °C	21.3 °C	
5	0.5272 $\frac{\text{m}}{\text{s}}$	0.0012	≈ 7 h	21.3 °C	22.9 °C	
$5_{cont.}$	0.5243 $\frac{\text{m}}{\text{s}}$	0.0012	≈ 18 h	22.9 °C	24.1 °C	Last test was continued due to maintenance
6	0.5276 $\frac{\text{m}}{\text{s}}$	0.0009	≈ 14 h	20.6 °C	22.8 °C	$C_T > 0.2$
7	0.5278 $\frac{\text{m}}{\text{s}}$	–	≈ 24 h	22.8 °C	23.8 °C	LDV crash, RMS was 1.15%. $C_T < 0.06$
8	0.5276 $\frac{\text{m}}{\text{s}}$	0.0008	≈ 16 h	23.8 °C	24.4 °C	$C_T > 0.18$
9	0.5255 $\frac{\text{m}}{\text{s}}$	0.0010	≈ 13 h	20.8 °C	22.3 °C	

Table 3.4: Inflow velocity measured with LDV, and water-temperature for static and Anderson comparison tests.

Test-nr.	$\overline{u_{inf}}$	$c_v(u_{inf})$	Duration	Water Temperature	Note
11	0.2485 $\frac{\text{m}}{\text{s}}$	0.0033	2 h 36 min	19.0 °C	static test low-speed
12	0.2512 $\frac{\text{m}}{\text{s}}$	0.0033	6 h	19.0 °C	Anderson test low-speed
13	0.5263 $\frac{\text{m}}{\text{s}}$	0.0012	4 h	19.9 °C	Anderson test high-speed without TS
14	0.5245 $\frac{\text{m}}{\text{s}}$	0.0041	3 h 0 min	20.0 °C	Static test high-speed without TS
15	0.5244 $\frac{\text{m}}{\text{s}}$	0.0039	3 h 0 min	20.0 °C	Static test high-speed with TS
16	0.4747 $\frac{\text{m}}{\text{s}}$	0.0013	4 h	24.3 °C	Anderson test high-speed with TS

Inflow Velocity Profile

The inflow velocity profile, and wall boundary layer is measured using the laser Doppler velocimetry (LDV) device. The LDV probe is mounted on a transverse system which allows it to move in freely in x, y, and z direction. Measurements are done on a grid in the yz plane, which is normal to the inflow velocity. On each position up to 1000 samples are captured, except for near the boundary layer, to save time, the sample size is here 100. The inflow profile is measured for the two inflow (u_{inf}) velocities used in the optimisation experiments; $0.5217\,\mathrm{m\,s^{-1}}$ in figure 3.13, and $0.2482\,\mathrm{m\,s^{-1}}$ in figure 3.14. In both figures the laminar boundary layer position defined by Blasius Equation (2.25), and turbulent boundary layer (Equation (2.27)) is indicated.

Refering to Table 2.3, it is expected that the boundary layer is definitely turbulent ($\delta_{turb.}$) at the tank-top for $u_{inf} = 0.5217\,\mathrm{m\,s^{-1}}$, and will be in transition from a laminar boundary layer ($\delta_{blasius}$) at $u_{inf} = 0.2482\,\mathrm{m\,s^{-1}}$. This is also confirmed by the LDV measurements, the line where $u/u_{inf} > 0.99$ denotes the boundary layer position, which matches with $\delta_{turb.}$ in Figure 3.13, and also $\delta_{blasius}$ matches with Figure 3.14.

A deviation is observed at the tank-bottom, the boundary layer is measured much thicker than what is predicted by theory. This could be due to that the edge of the temporary bottom plate facing the inflow stream causes flow detachment. The error this introduces is however insignificant for about 30 mm height, the velocity only reduced to 90%, in addition this covers only 8% of the total section height. When determining the efficiency it is assumed that the velocity in the centre of the tank covers the entire cross-section. Using Equation (2.9), the efficiency will be underestimated.

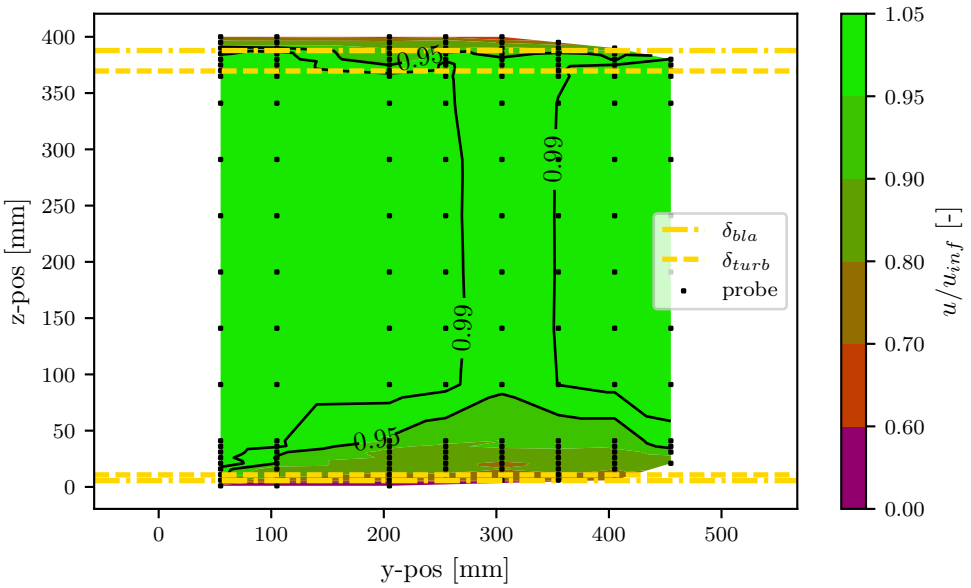

(a) Overview

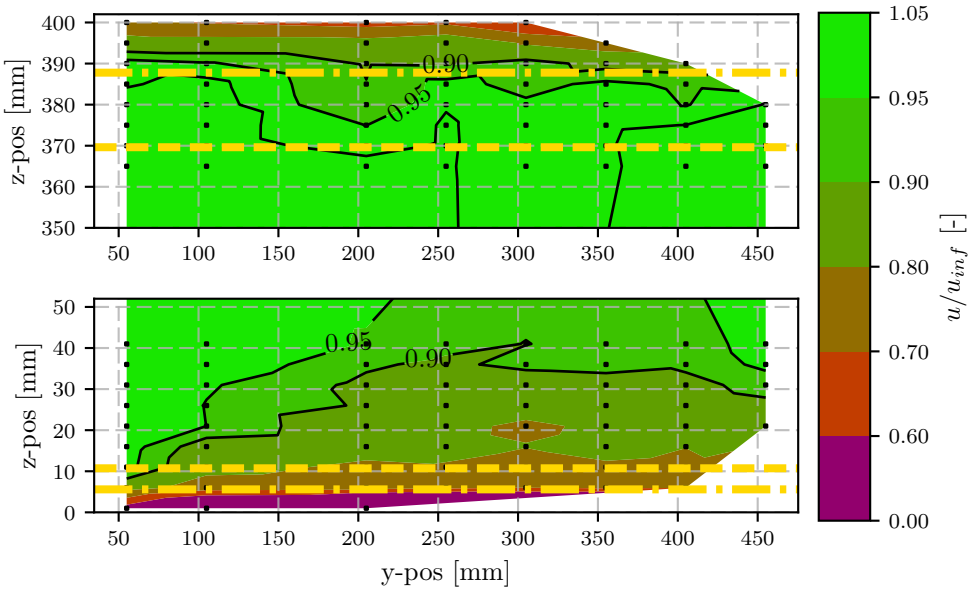

(b) Zoomed near the boundary layers

Figure 3.13: Inflow velocity profile at $u_{inf} = 0.5217\,\mathrm{m\,s^{-1}}$, with a water temperature of 20.6 °C. Note that the tank centre is at $y = 300\,\mathrm{mm}$, because the total tank width is 600.9 mm. Boundary layers at the tank-walls are of no interest, because the foil is not interacting with them. The speed reduction at $y = 300\,\mathrm{mm}$ is due to that the foil is still in place downstream of the LDV probe.

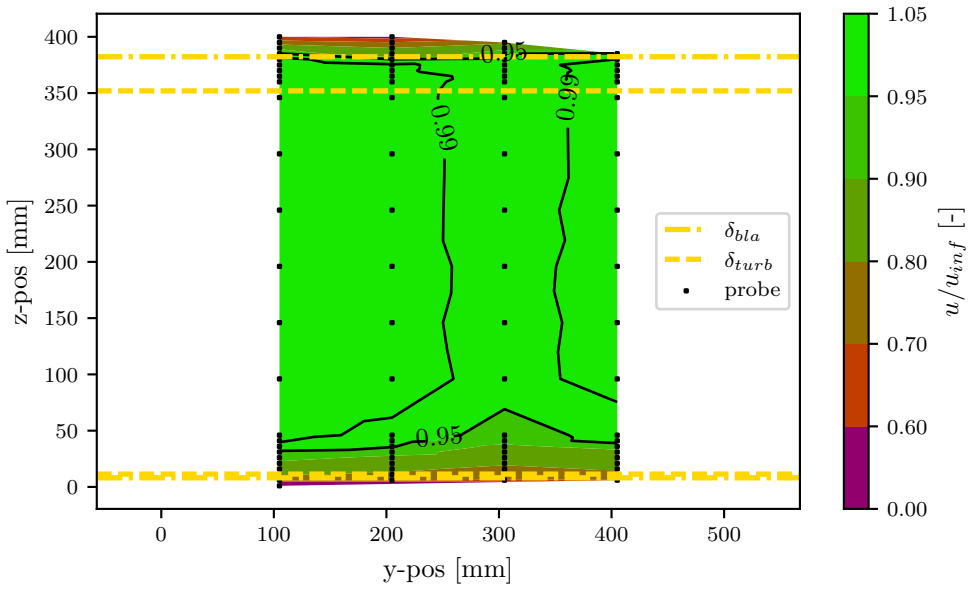

(a) Overview

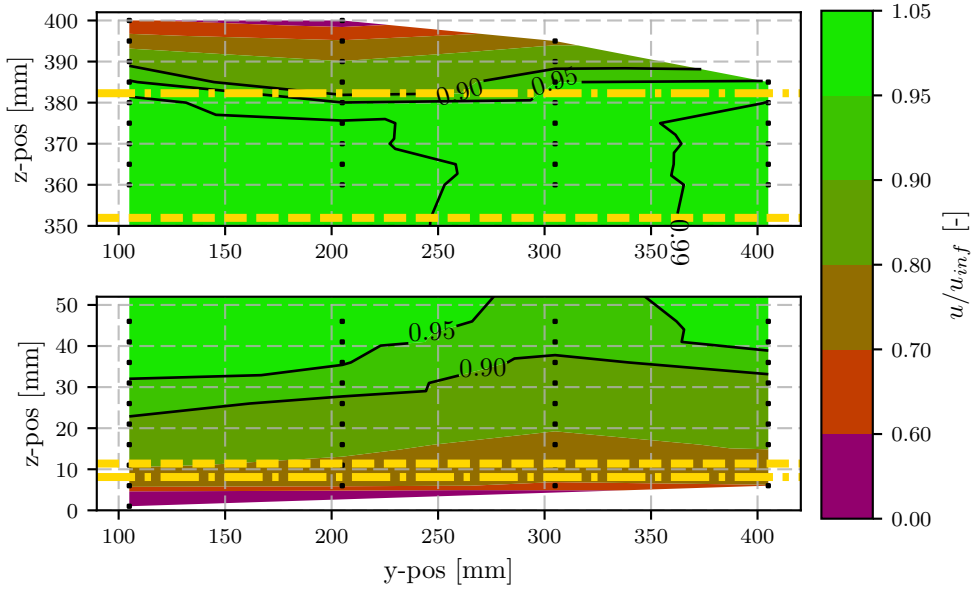

(b) Zoomed near the boundary layers

Figure 3.14: Inflow velocity profile at $u_{inf} = 0.2482\,\mathrm{m\,s^{-1}}$, with a water temperature of 22.1 °C. Note that the tank centre is at $y = 300\,\mathrm{mm}$, because the total tank width is 600.9 mm. Boundary layers at the tank-walls are of no interest, because the foil is not interacting with them. The speed reduction at $y = 300\,\mathrm{mm}$ is due to that the foil is still in place downstream of the LDV probe.

3.6 Static Calibration

Static tests are conducted to find the lift and drag characteristic in different flow conditions. In addition the effect of turbulence-stimulation is evaluated. The foil is held at a steady yaw angle for 50 s, where the mean lift (C_l), drag (C_d) and torque (M_z) is measured. The yaw angle is stepped with 0.5° increments. To measure static hysteresis the yaw angle is stepped in and out of stall angle, this is done by stepping the yaw angle in the following sequence: $\alpha = 0° \rightarrow \alpha = -20° \rightarrow \alpha = +20° \rightarrow \alpha = 0°$.

As a comparison to full-scale behaviour the experimental measurement presented by Riegels (1961) are used. The experimental measurements are done in the AMES laboratory at Iowa State University in a high-speed wind-tunnel. The foil used in the experiment has a NACA0015 geometry, the same as for this thesis. The author claims the experiments are done at Mach number $M = 0.3$ with a 6 inch model. In general for experiments done at $M < 0.3$ the compressibility effect is small, and can be considered incompressible (Young, Munson, Okiishi, & Huebsch, 2010). The experiments can therefore be compared to tests done in water which is incompressible. By assuming the air-temperature in their test was 17 °C, the kinematic viscosity and speed of sound is; $v_{air@17\,°C} = 15.9 \times 10^{-6}\,\mathrm{m^2\,s^{-1}}$ and $c_{air@17\,°C} = 343.3\,\mathrm{m\,s^{-1}}$ respectively (Inglezakis & Poulopoulos, 2006). When using the definition for Mach number (equation (3.3)) and Reynold number (equation (2.4)), the chord Reynold number of the experiment can be deducted to $Re_c \approx 1e6$, which should be representative for a turbulent boundary layer, and full-scale behaviour.

$$M = \frac{u_{inf}}{c_{air@17\,°C}} \tag{3.3}$$

Where M is the mach number, u_{inf} the inflow velocity, and $c_{air@17\,°C}$ speed of sound in air at 17 °C.

As an additional comparison the lift slope $\frac{dC_l}{d\alpha}$, for full-scale, is compared to another source. According to Abbott and Von Doenhoff (1959) the lift slope for a NACA0015 airfoil is $\frac{dC_l}{d\alpha} \approx 5.7$, close to flat plate theory with a slope of 2π. This is based on experimental data measured at $Re_c = 6e6$, which can correspond to the flow regime of a full-scale airfoil.

3.6.1 Lift-Coefficient, C_l

In Figure 3.15 the lift coefficient versus angle of attack (α) is illustrated for $Re_c \approx 39200$. The clean results describes a foil without turbulence stimulation (TS), and zig-zag a test with turbulence stimulation (TS), as photographed in Figure 3.11. From the plot it is apparent that the TS has removed the deadband at low angles of attack due to laminar separation bubbles. The lift slope is now completely linear in range $-7° < \alpha < 7°$. The static hysteresis which is observed at $\alpha \approx 10°$ is also removed due to TS. Two negative consequences on lift coefficient are observed; the stall angle has reduced from $\alpha_{max} \approx 9°$ to $\alpha_{max} \approx 7°$, and the maximum lift coefficient has reduced from $C_{l(max)} \approx 0.7$ to $C_{l(max)} \approx 0.45$.

When comparing the zig-zag curve in Figure 3.15 with the high Reynold number results described by Riegels (1961), it is easy to see similarities in the curves. The main differences are a different $\frac{dC_l}{d\alpha}$ slope, and reduced stall angle and maximum lift coefficient.

With a Reynold number reduced to $Re_c = 18600$, which is the regime where optimisation tests with high Strouhal number are tested, the deadband is increased significantly. This is illustrated in Figure 3.18, with results from higher Reynold number in transparent colors. Previous research described in Section 2.6.1 indicated that no turbulence stimulation can be achieved in a Reynold number this low, the static test is therefore only done without TS (clean).

An important issue arises when doing tests at low Reynold number, the zero position in yaw is usually found by rotating the foil until no lift forces are measured. By using this procedure the zero position for yaw could therefore lay between $-3° < \theta < 3°$ at $Re_c = 18600$. To avoid this behaviour, zero position is set at a high Reynold number where no dead-band is observed. The most prominent research articles which experimentally investigated oscillating hydrofoils, introduced in section **??**, have all calibrated zero yaw angle at low Reynold number $Re_c \leq 40000$ (Hover et al., 2004; Read et al., 2003; J. Anderson et al., 1998; Triantafyllou et al., 1993). None of them have discussed the static characteristics in their experiments, or any problems concerning low Reynold number behaviour.

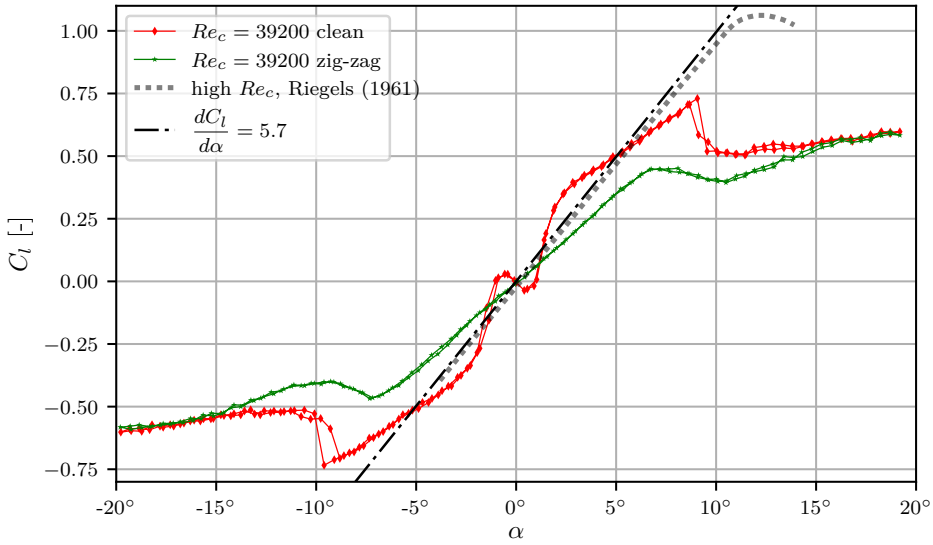

Figure 3.15: Static lift coefficient, C_l, versus angle of attack, α, at $Re_c = 39200$. With and without zig-zag turbulence stimulation. Turbulence stimulation is effective in removing deadband and static stall hysteresis, a downside is reduced stall angle.

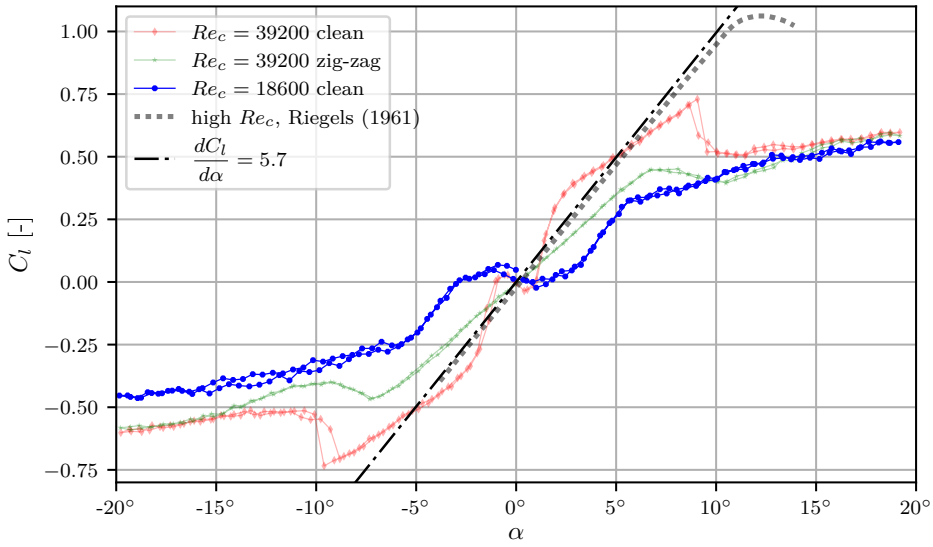

Figure 3.16: Static lift coefficient, C_l, versus angle of attack, α, at $Re_c = 18600$ for a clean foil. The results at $Re_c = 39200$ from figure 3.15 are included as shaded lines. Deadband is large for this case, and no clear stall angle can be determined, but indicated at 6°.

Table 3.5: Drag coefficients at $\alpha = 0°$, experimental and theoretically calculated with equation (2.29).

Case	Experimental C_d	Theoretical C_d
$Re_c = 39200$ clean	0.024	0.030
$Re_c = 39200$ zig-zag	0.038	0.030
$Re_c = 18600$ clean	0.032 to 0.067	0.039
high Re_c, Riegels (1961)	0.006	0.0125

3.6.2 Drag-Coefficient, C_d

The turbulence stimulation (TS) has mainly a negative impact on the drag-coefficient. Drag is increased significantly in the region of low angle of attack (α), as it is seen in Figure 3.17. The reduced stall angle (α_{max}) has caused the drag to increase at a lower angle of attack.

For the clean foil at $Re_c = 18600$ in Figure 3.18, the drag seems to be dependent on whether the angle is increasing or decreasing. However, this can also be attributed to measurement error, the inflow velocity is quite low $u_{inf} \approx 0.251\,\mathrm{m\,s^{-1}}$, which in return causes very small forces.

In an attempt to argue that the measured drag forces at $\alpha = 0°$ are reasonable, the theoretical drag is calculated with Equation (2.29) (Hoerner, 1965), and presented in table 3.5. At $Re_c = 39200$ with a clean foil the measured drag is slightly lower than theoretical, and slightly higher with zig-zag TS. For $Re_c = 39200$, the theoretical drag is within the range measured. One has to keep in mind that the theoretical drag is calculated with a very simple formula, which does not account for any special effects at low Reynold number. The conclusion: There is a good correspondence between the measured- and theoretical-drag. Surprisingly is the drag from Riegels (1961) experiments at $Re_c \approx 1e6$ measured to the half of theoretical drag, which gives an indication that equation (2.29) is conservative if used to predict drag at full-scale.

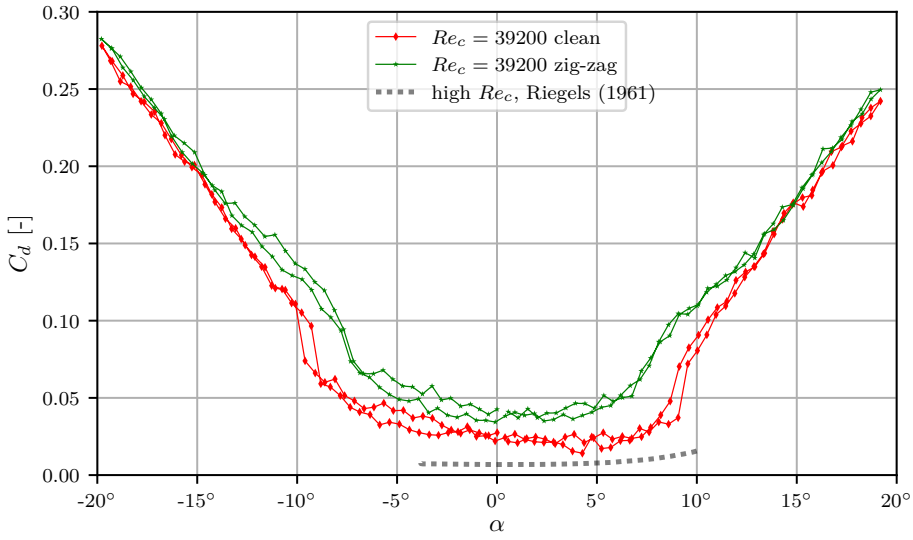

Figure 3.17: Static drag coefficient, C_d, versus angle of attack, α, at $Re_c = 39200$. With and without zig-zag turbulence stimulation (TS). Drag is increased due to TS, drag in model-scale is much higher than with a comparable test with a higher Reynold number at $Re_c \approx 1e6$.

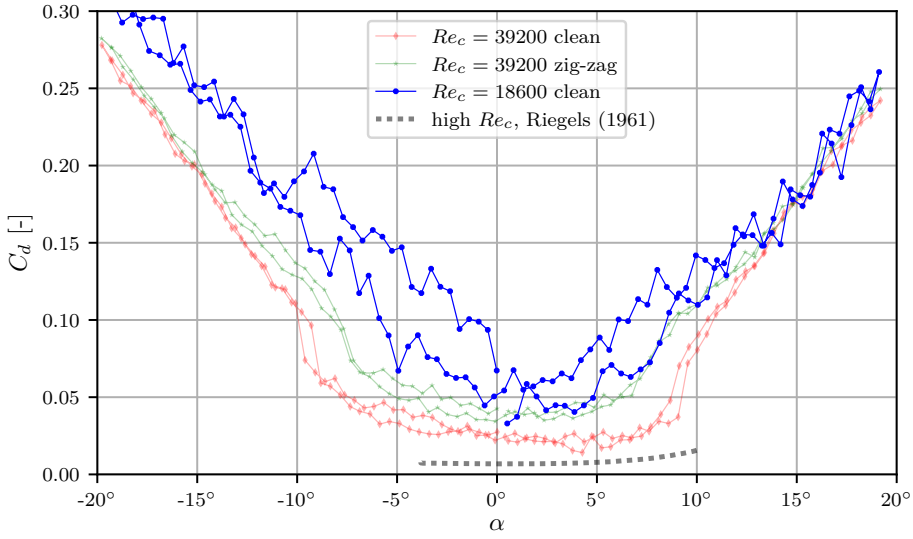

Figure 3.18: Static drag coefficient, C_d versus angle of attack, α, at $Re_c = 18600$ for a clean foil. The results at $Re_c = 39200$ from Figure 3.17 are included as shaded lines. Very small forces are measured, this could cause a high measurement error, causing the asymmetry at $Re_c = 18600$.

3.6.3 Torque-Coefficient, C_m

Behaviour of the torque coefficient is also drastically changed when zig-zag TS is used at $Re_c = 39200$, as seen in Figure 3.19. Interestingly is the peak torque reduced for low angles before stall $-7° < \alpha < 7°$. For $Re_c = 18200$, Figure 3.20 gives the same indications as seen at the drag coefficient C_d, the measured forces are small, which gives high uncertainty. To be certain that the abnormal behaviour is caused by measurement error, repetition tests should have been done. Due to time limitations, focus was set on doing uncertainty analysis for dynamic tests instead. The forces are significantly higher for dynamic stall, for high thrust efficiency it is typical that dynamic stall occurs (Triantafyllou et al., 1993).

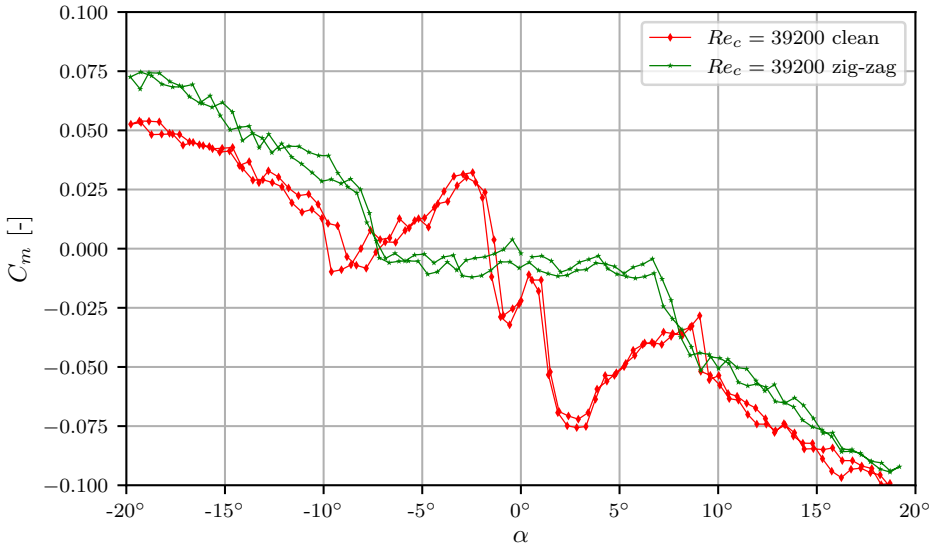

Figure 3.19: Static moment coefficient, C_m, versus angle of attack, α, at $Re_c = 39200$. With and without zig-zag turbulence stimulation (TS). The torque at angles below stall has reduced significantly due to TS.

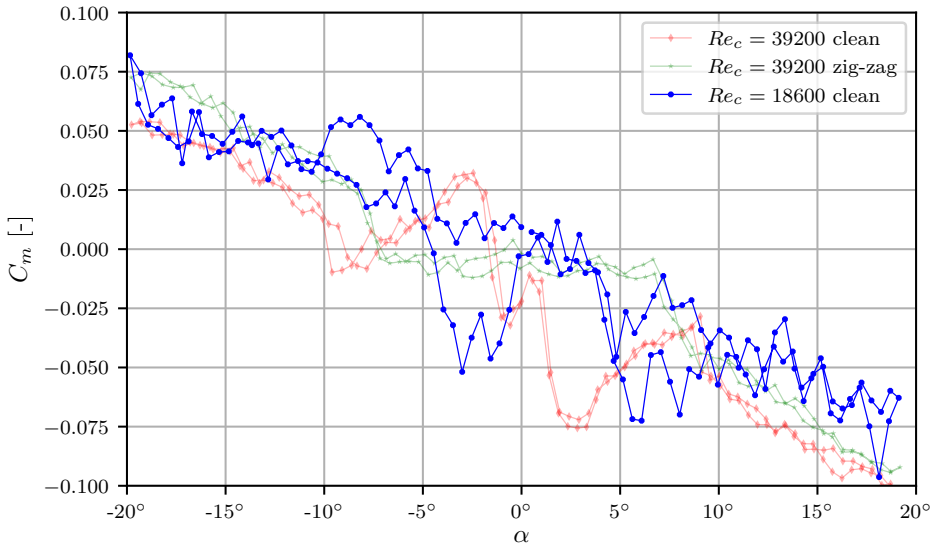

Figure 3.20: Static moment coefficient, C_m versus angle of attack, α, at $Re_c = 18600$ for a clean foil. The results at $Re_c = 39200$ from Figure 3.19 are included as shaded lines.

3.7 Benchmark

As a benchmark the experiments by J. Anderson et al. (1998) are repeated. The main difference is that they are using a thinner foil, which thickness is 12% of chord length (NACA0012), opposed to the foil in the presented experiments which is 15% of chord length thick (NACA0015). A difference is also in how the foil-ends are treated, in the experiments by J. Anderson et al. (1998) circular end-plates are used, which will not introduce a thick boundary layer, as discussed in Section 3.5.2. If the the end-plates are large enough to prevent downwash, higher efficiency should be expected. In addition the axis of yaw rotation is placed differently, in Anderson's experiments it is placed at $0.3c$ from leading edge, in this thesis the rotation axis is located at $0.25c$.

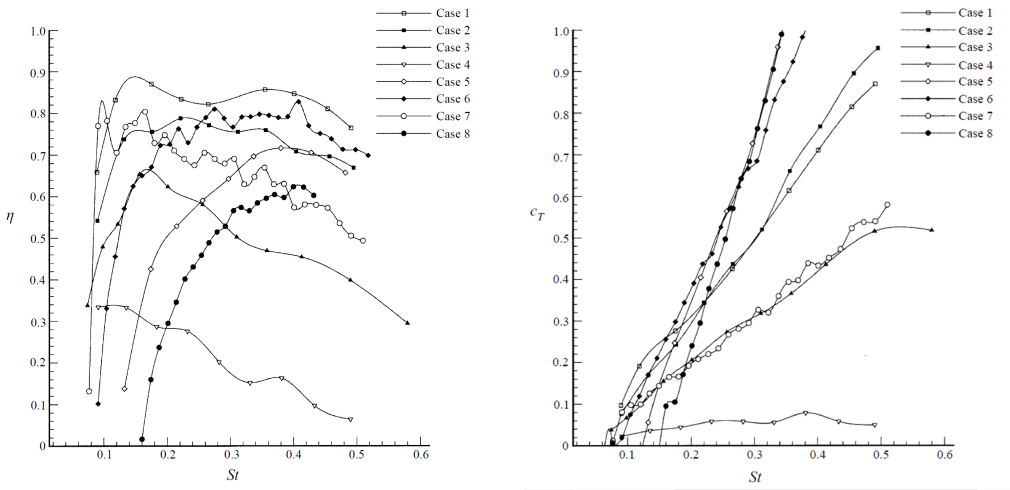

(a) Efficiency η **(b)** Thrust coefficient C_T

Figure 3.21: Experimental results for an oscillating hydrofoil at various Strouhal numbers by J. Anderson et al. (1998). The cases denote a different combination of sway amplitude, phase, and maximum angle of attack, see Table 4.1 for case description.

Chapter 4

Results and Discussion

In this chapter the thrust optimisation results are presented and discussed, an effort is made to evaluate how phase (ϕ), maximum angle of attack (α_{max}), and Strouhal number (S_t) affect the thrust efficiency and thrust coefficient. As a calibration, the experiments by J. Anderson et al. (1998) are repeated. How the precision error varies with efficiency (η) and thrust coefficient (C_T) is investigated through repeated tests.

4.1 Repetition of Anderson's Experiments

Almost all the experiments by J. Anderson et al. (1998) are repeated. Due to limited oscillation frequency, the highest tested Strouhal number is; $S_t < 0.3$ for $Re_c \approx 19000$, and $S_t \approx< 0.23$ for $Re_c \approx 40000$. The original experiments are done at $S_t \approx 40000$ without turbulence stimulation (TS). A few of the experiments will be highlighted and discussed here, plots for the other can be found in Appendix I. A summary of the repeated tests, together with its motion-parameters is given in Table 4.1.

In Figure 4.2 very good agreement is found for Anderson's case 7 between the experiments. This is only for when the drag force is set to 0 at $\alpha = 0°$ during a steady inflow velocity. When drag forces are included, the repeated experiments show lower efficiency and thrust. The efficiency reduction corresponds somewhat

Table 4.1: Summary of the oscillating hydrofoil experiments by J. Anderson et al. (1998), including a comment if good agreement is seen in the repeated experiments without skin friction.

Case	α_{max}	ϕ	y^{amp}_{sway}	Good agreement?
1	21°	75°	0.75	No
2	17°	105°	0.75	Fairly, $\Delta\eta \approx 10 - 20\%$
4	5°	90°	0.75	No, much higher for repeated
5	25°	90°	0.75	Fairly, $\Delta\eta \approx 10\%$
6	20°	90°	0.75	Yes, for $Re_c \approx 40000$
7	10°	90°	0.75	Yes
8	30°	90°	0.75	Yes

to the static measurements in Figure 3.18, the lowest efficiency is measured for $Re_c \approx 40000$ with turbulence stimulation (TS), where also the highest drag was recorded for low angles of attack, α.

No agreement at all was found for case 1, as seen in Figure 4.1. This was the case where originally the highest efficiency was reported. The phase was $\phi = 75°$, it seems like only the experiments with a phase of $\phi = 90°$ are accurately reproduced. With an exception for case 4, which has a very low maximum angle of attack ($\alpha_{max} = 5°$), the reproduced results show a unrealistic high efficiency. When drag is included, only 10% higher efficiency is observed in the reproduced results. This is opposite as to what is seen for all other cases. The author is uncertain to what the cause is for this, it could be due to measurement errors, as the forces are very low for small angles of attack, to evaluate this repeated tests should have been conducted. Another argument to why the tests at different phases from 90° cannot be reproduced, could be due to the different placement of yaw axis, which is $0.25c$ for the repition-experiments, and $0.3c$ in the experiments by J. Anderson et al. (1998) and Read et al. (2003).

As discussed in Section 1.2.3, has Read et al. (2003) repeated some of J. Anderson et al. (1998) experiments. They were also unable to reproduce the results in case 1, with a phase of $\phi = 75°$, but found good agreement for case 7, where the phase is $\phi = 90°$.

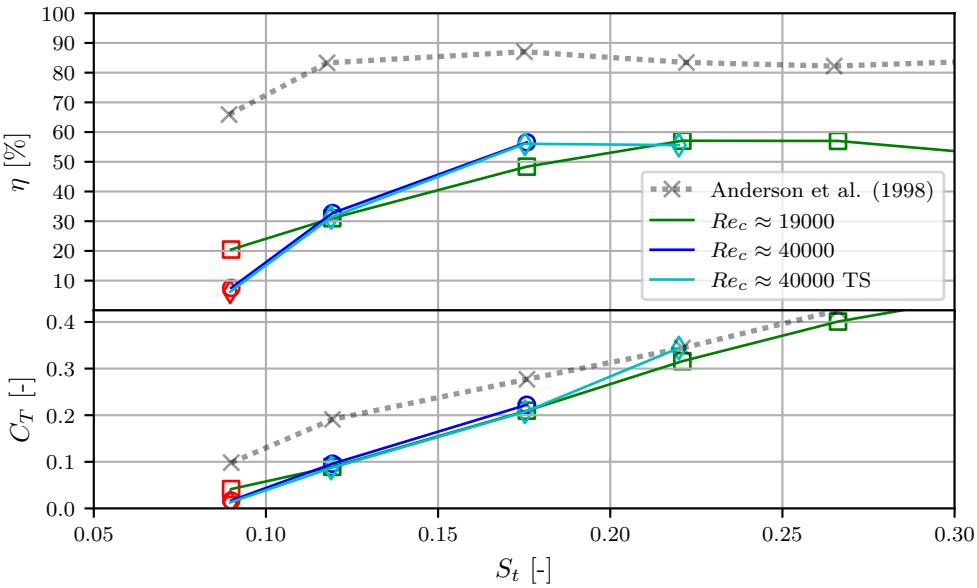

Figure 4.1: Repetition of Anderson's experiment for case 1. Experiments are repeated at the same Reynold number ($Re_c \approx 40000$), drag force (F_d) is zeroed with steady inflow-velocity. No agreement was found, the same conclusion as by Read et al. (2003).

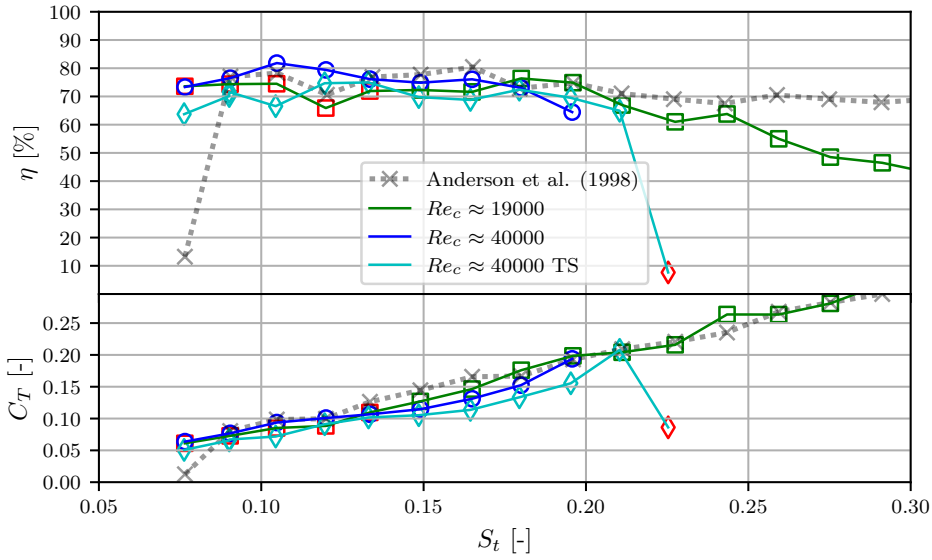

(a) Very good agreement when skin friction is removed, zero drag F_d is found at a steady inflow-velocity.

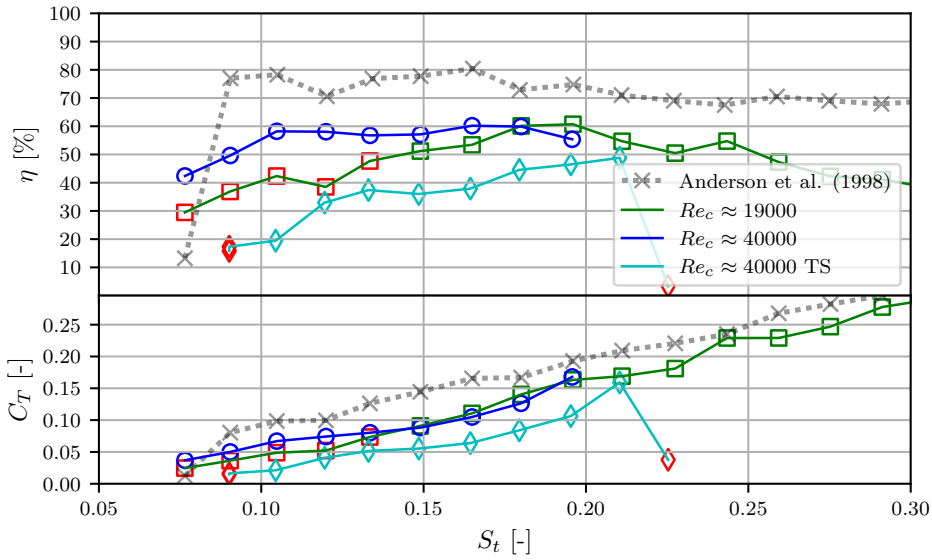

(b) Bad agreement, zero drag F_d is set without inflow-velocity.

Figure 4.2: Repetition of Anderson's experiment for case 7. Experiments are repeated at the same Reynold number $Re_c \approx 40000$, with and without turbulence stimulation (TS). This case shows best agreement between the experiments. To test higher Strouhal numbers, the repetition is also done for $Re_c \approx 19000$. Red symbols denote experiments which have a precision error between oscillations higher than 5% for thrust, and are outliers.

4.2 Optimisation Results

All tested individuals for the three cases (i.e. sinus, non-sinus and lower Reynold number) are given as scatter-diagrams in Figures 4.5, 4.4, and 4.3 respectively. Different colours denote the test-numbers given in Table 3.3, what differentiates them is usually that the experiment has been conducted on a different day, with slight change in conditions, as discussed in Section 3.5.2. The large difference in efficiency can be accounted for increased drag due to turbulence stimulation (TS), and will be discussed in the following sections.

For the tests done at $Re_c \approx 40000$, Figures 4.4 and 4.5, the individuals with highest efficiency seem to be forming a continuous function $\eta(C_T)$. This is an indication that a global maxima has been found in the optimisation. This line is not so clear for $Re_c \approx 19000$, seen in Figure 4.3, it could be due to higher test-range of S_t numbers, and thereby covering different wake dynamics, making a global maxima more difficult to find. If one assumes that the findings by J. M. Anderson (1996) on wake dynamics described in Section 2.2.1 are valid for non-sinusoidal oscillating foils, then the experiments at $Re_c \approx 40000$ should only form a traditional Von Kármán Vortex Street, illustrated as case A and B in Figure 2.4. The experiments for Figure 4.3 would then experience a reverse and traditional Von Kármán Vortex Street, indicated as case A, B and C respectively.

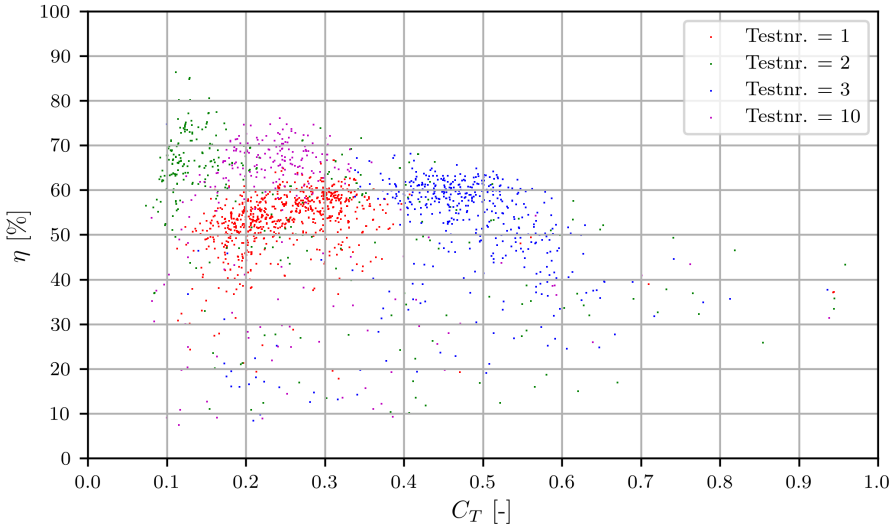

Figure 4.3: Summary of all optimization tests done at $Re_c \approx 19000$ where all motion parameters of equation (2.16) and (2.17) can be adjusted. In case 3 minimum acceptable C_T is set to 0.5, and for case 10 maximum acceptable C_T is set to 0.4. For the other cases optimization fitness is not affected by C_T, as long it is above 0.

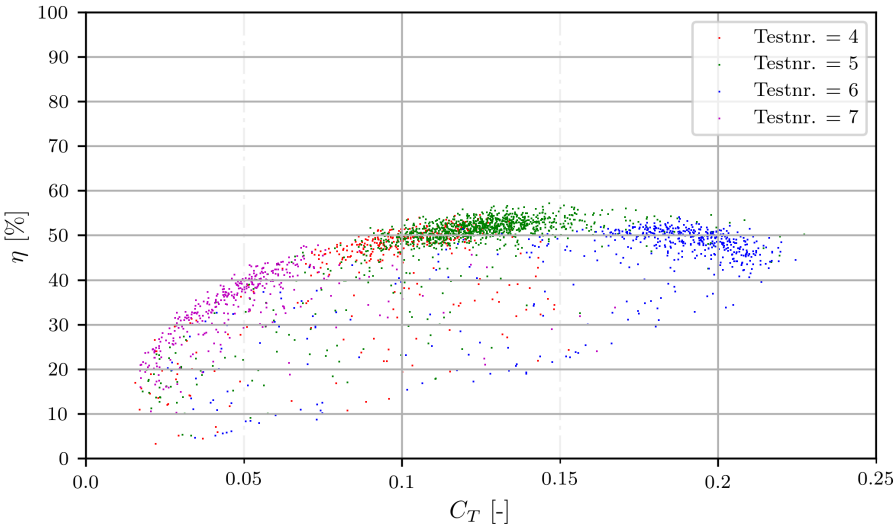

Figure 4.4: Summary of all optimization tests done at $Re_c \approx 40000$ where all motion parameters of equation (2.16) and (2.17) can be adjusted. In case 6 the minimum acceptable C_T is set to 0.2, and for case 7 the maximum acceptable C_T is set to 0.06. For the other cases optimization fitness is not affected by C_T, as long it is above 0.

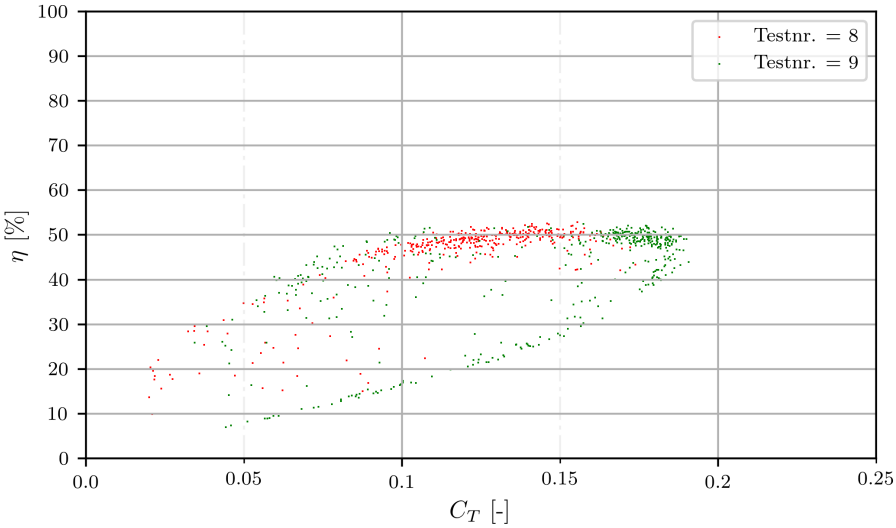

Figure 4.5: Summary of all optimization tests done at $Re_c \approx 40000$ with K_θ and K_y in Equations (2.16) and (2.17) set to 0, hence only sinus motions allowed in sway and yaw. These results can be compared directly to Figure 4.4. Note that no individuals were able to achieve a thrust coefficient C_T above 0.18. For case 8 the minimum acceptable C_T is set to 0.18, for case 7 optimization fitness is not affected by C_T, as long it is above 0.

4.2.1 Least-Square Fit

A function can be fitted to the best individuals along the span of resulting thrust coefficients C_T. This will make it easier to compare results from different cases (i.e. sinus, non-sinus and lower Reynold number). The coefficients (a, b, c, and d) in Equation (4.1) will be fitted using least square error method, the resulting coefficients are summarized in Table 4.2.

$$\eta(C_T) = a + b\,C_T + c\,C_T^2 + d\,C_T^3 \tag{4.1}$$

As an example the least-square curve for the test-case with $Re \approx 40000$ and Non-Sinus motion is illustrated in Figure 4.6 together with all tested individuals and the selected individuals used for curve-fitting as a scatter-plot. The same plots for the other cases can be found in Appendix H.

To make it easier to compare results with different flow-conditions and turbulence stimulation, the skin friction is removed from all three optimisation-cases. This is achieved by zeroing the drag force at zero angle of attack with a steady foil. The least-square fit functions for all three cases are illustrated in Figure 4.7. Tests done at $Re_c \approx 19000$ are able to produce the highest thrust, this is expected due to a higher Strouhal number. There is a minor improvement of 5% increased efficiency for $0.01 < C_T < 0.21$ for a non-sinusoidal motion. This is so insignificant that it is expected to be diminished by the complexity of creating a full-scale machinery which can represent other motions than sinus.

In an ideal world without frictional losses it is expected that it is most efficient to move as little water as possible to produce thrust. The results in Figure 4.7 support this: When friction is subtracted, the efficiency is gradually decreased with C_T; however for the case with turbulence-stimulation and large skin-friction, the highest efficiency is reached at $C_T \approx 0.12$. This could also occur in full-scale, dependent on the magnitude of skin-friction.

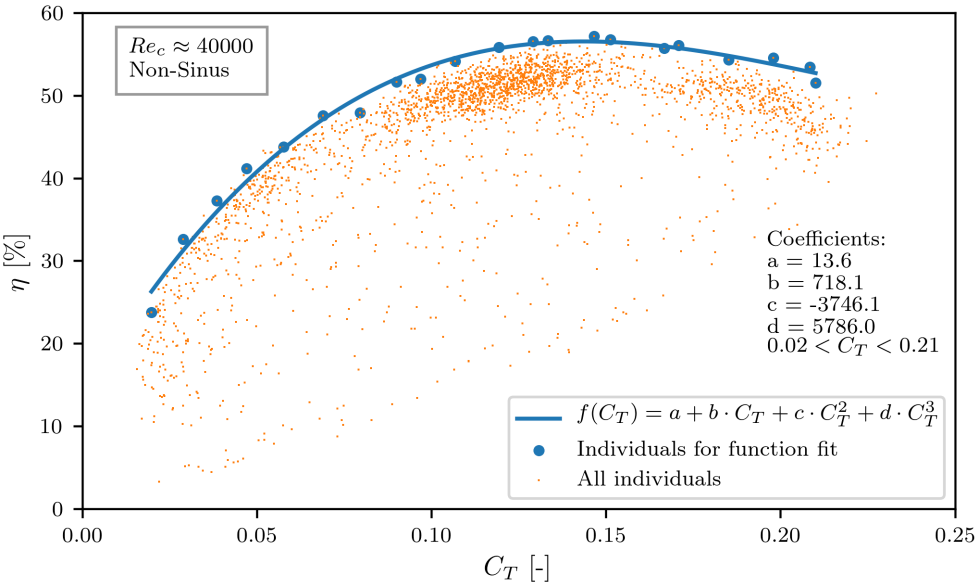

Figure 4.6: Least square fit of Equation (4.1) to the test-individuals with highest efficiency (η) for different thrust coefficients (C_T).

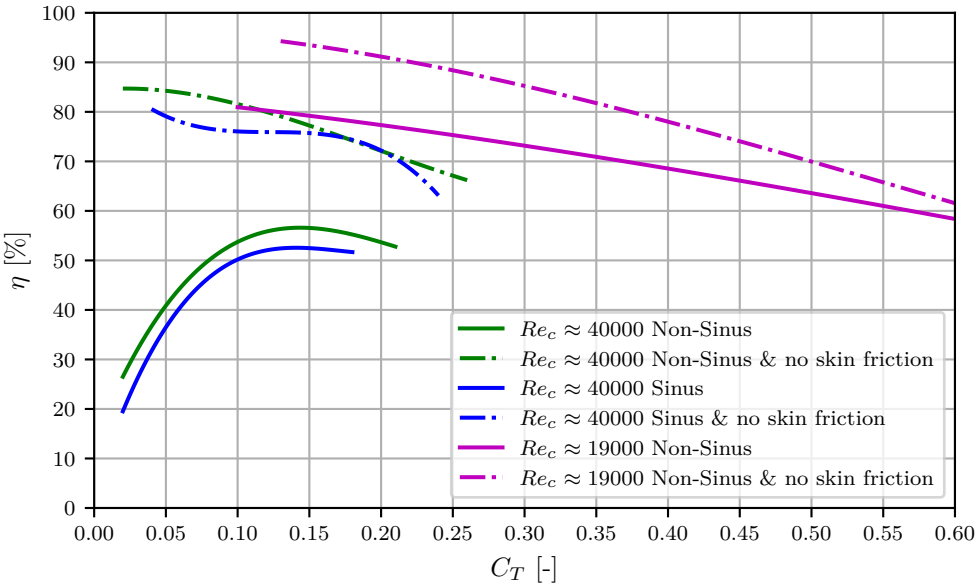

Figure 4.7: Comparison of the least-square fitted function of the highest efficiency for various optimisation runs. Lines with the same colour are from the same data-set, but the skin friction is removed on the dashed line. Note that the tests at $Re_c \approx 40000$ are all done with turbulence stimulation, hence the low efficiency.

Table 4.2: Least square fit of equation (4.1) to the individuals with highest efficiency along a range of different C_T values.

Case	a	b	c	d	C_T^{min}	C_T^{max}
$Re_c \approx 40000$ Non-Sinus	13.6	718.1	−3746.1	5786.0	0.02	0.21
$Re_c \approx 40000$ Non-Sinus & no skin friction	84.4	28.3	−683.3	1174.2	0.02	0.26
$Re_c \approx 40000$ Non-Sinus & full-scale drag	74.4	9.5	−11.8	−777.7	0.04	0.26
$Re_c \approx 40000$ Sinus	3.5	905.9	−5446.0	10556.7	0.02	0.18
$Re_c \approx 40000$ Sinus & no skin friction	90.8	−359.6	2908.7	−7879.8	0.04	0.24
$Re_c \approx 19000$ Non-Sinus	83.9	−26.0	−37.6	16.7	0.10	0.82
$Re_c \approx 19000$ Non-Sinus & no skin friction	97.2	−6.1	−136.3	79.1	0.13	0.85

Full-Scale Drag

To investigate how drag impacts the efficiency at full-scale, the drag force is corrected to the drag coefficient which would be expected at $Re_c = 42 \times 10^6$ according to the procedure described in Section 2.6.2. This comparison is done for the experiments at $Re_c \approx 40000$ with turbulence-stimulation. The fitted function for $\eta(C_t)$ is illustrated in Figure 4.8 for when full-scale drag is corrected, drag forces are set to 0, and when model-scale drag is included.

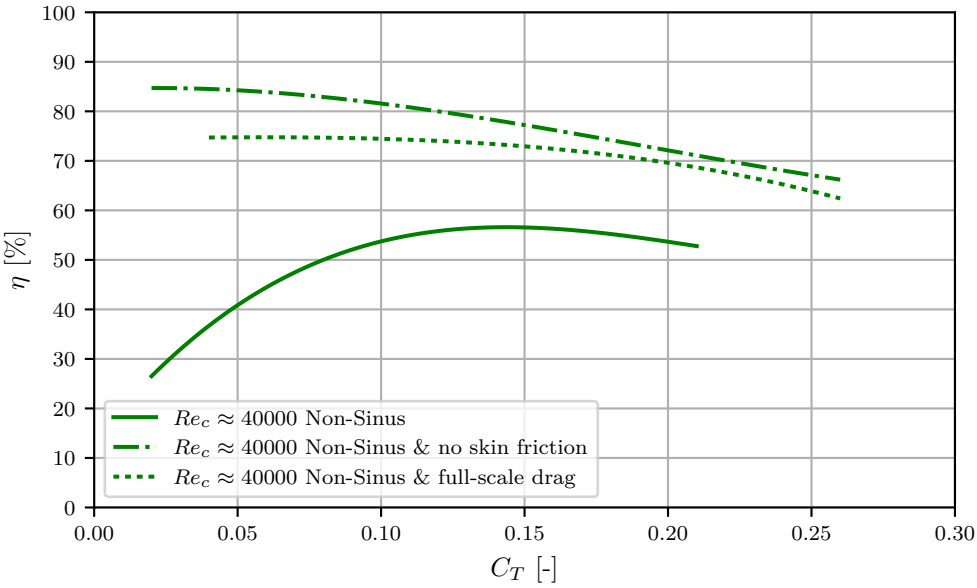

Figure 4.8: Comparison on how efficiency is affected when the theoretical drag for full-scale is corrected using methods described in Section 2.6.2. Note that when comparing frictionless line, and the one including full-scale drag it is obvious that including full-scale drag has the largest impact on low thrust coefficients.

4.2.2 Efficiency and Thrust Response Contours

In an attempt to investigate how the motion parameters affect thrust and efficiency, maximum angle of attack (α_{max}) and Strouhal number (S_t) are considered. A contour-surface is generated in the same fashion as Read et al. (2003) has done, as seen in Figure 4.10.

All individuals tested in the optimisation run, unconditional if they are optimal or not, are gathered in a scatter-plot with Strouhal number (S_t) as x-axis, and maximum AoA (α_{max}) as y-axis. The results are divided into a grid, within each cell the most efficient result is considered. This is done because individuals are selected are random at the beginning of each run, and not all of them will therefore be optimal, to avoid this a requirement is set that at least 5 individuals must exist within one cell. The grid-cells and selected optimal individuals are illustrated in Figure 4.9 for $Re \approx 40000$, with and without skin friction. Contour-grid for the other case is given in Appendix J.

The efficiency (η) and thrust coefficient (C_T) contours are generated for $Re_c \approx 19000$ and $Re_c \approx 40000$, with and without skin friction. The results including friction are comparable with those by Read et al. (2003), where friction also is included. In Figure 4.11a a peak efficiency is seen at $S_T > 0.16$ and $10° < \alpha_{max} < 18°$, this is the region where the plateau of high efficiency starts for Reads results in figure 4.10a. The plateau also continues for higher S_t in the tests with $Re_c \approx 19000$, as illustrated in Figure 4.12a. However there is a peak efficiency observed at $0.16 < S_t < 0.24$ and $\alpha_{max} < 12°$, here the efficiency is increased from $\approx 65\%$ to $\approx 80\%$. Read observed a increase of efficiency in the same region, however it was only mild from $\approx 55\%$ to $\approx 60\%$.

When skin friction is disregarded, as seen in Figure 4.11c and 4.12c, High efficiencies are observed in the entire S_t range, as long as $\alpha_{max} <\approx 15°$. Recall that this is a quite large AoA, because the static stall angle at $Re_c \approx 40000$ is measured to 7°, and 5° for $Re_c \approx 19000$ (see figure 3.16). Dynamic stall effects are therefor important for efficient oscillating foil propulsion.

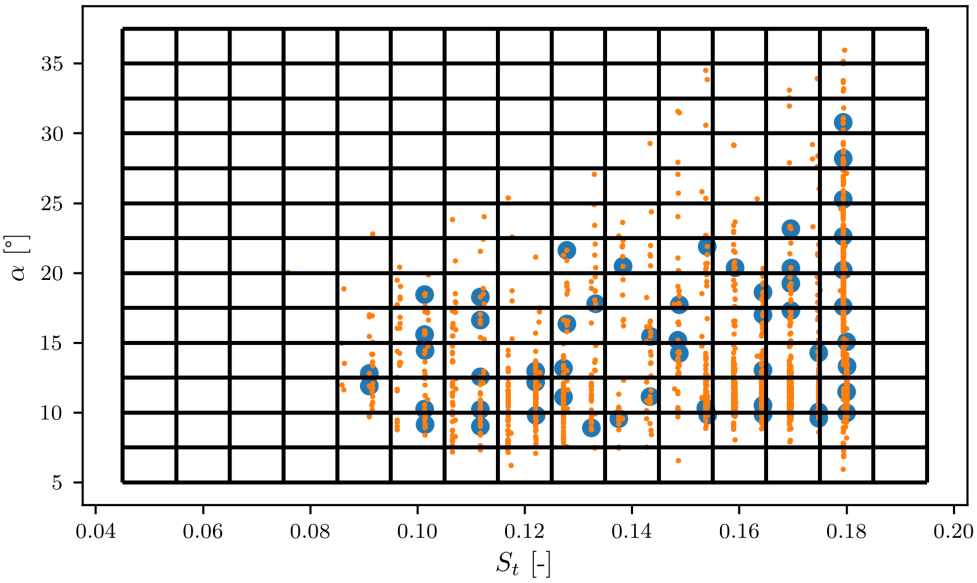

(a) $Re \approx 40000$.

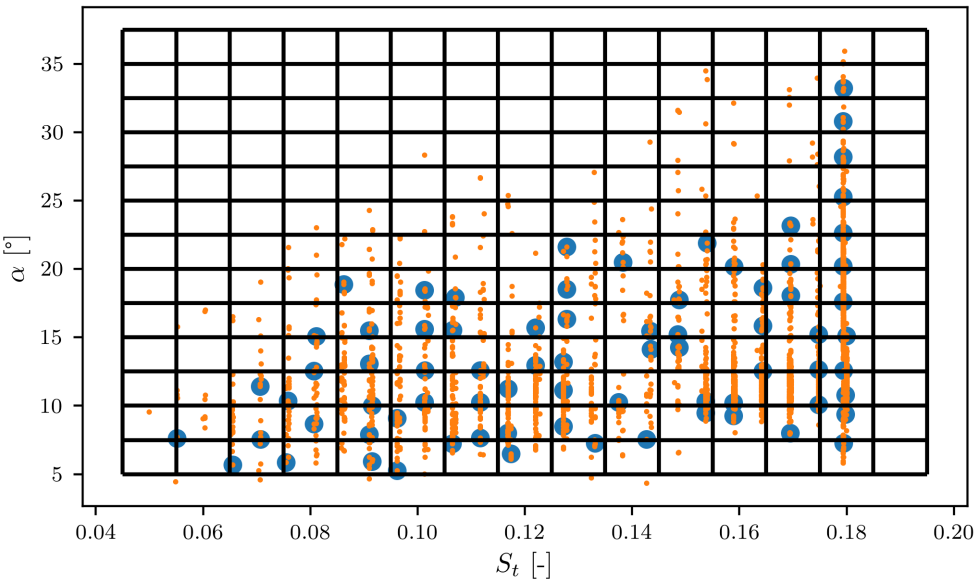

(b) $Re \approx 40000$ frictionless.

Figure 4.9: The individual with highest efficiency is selected in each grid cell to be used for the contour-plot in Figure 4.11. The selected individuals are marked with a blue dot. See appendix J for the same grid for other optimisation runs.

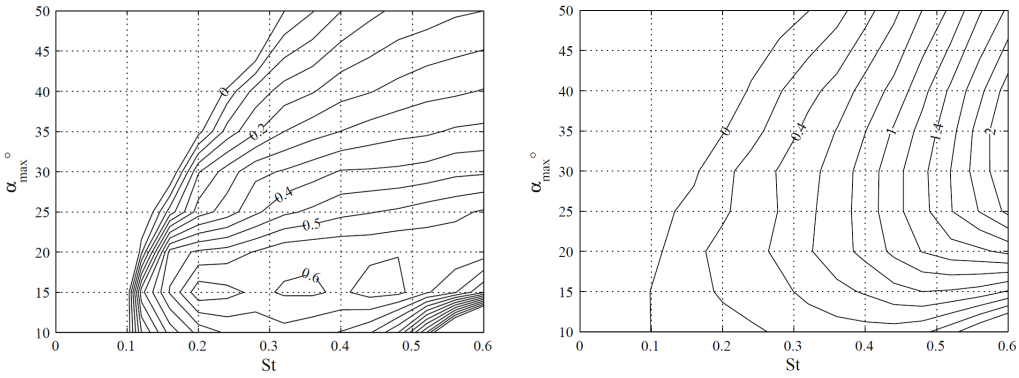

(a) Efficiency, η **(b)** Thrust coefficient, C_T

Figure 4.10: Summary of the experimental results by Read et al. (2003) on a oscillating hydrofoil, frictional drag is included.

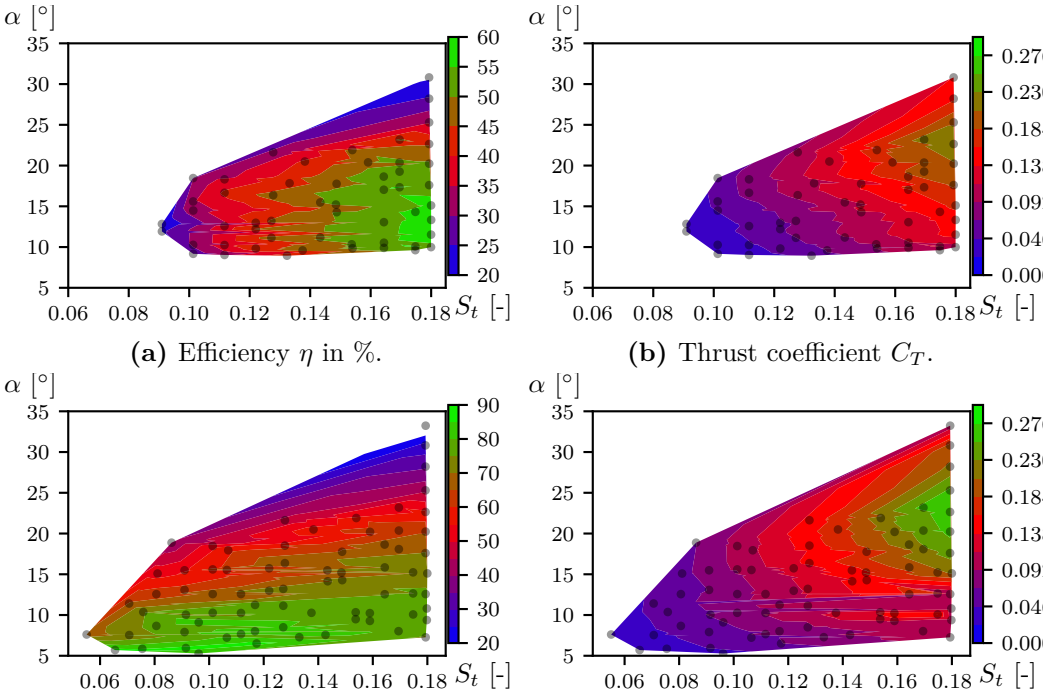

(a) Efficiency η in %. **(b)** Thrust coefficient C_T.

(c) Efficiency η in %, frictionless **(d)** Thrust coefficient C_T, frictionless

Figure 4.11: Contour-plots of the individuals with highest efficiency inside the $S_T - \alpha$ grid illustrated in figure 4.9.

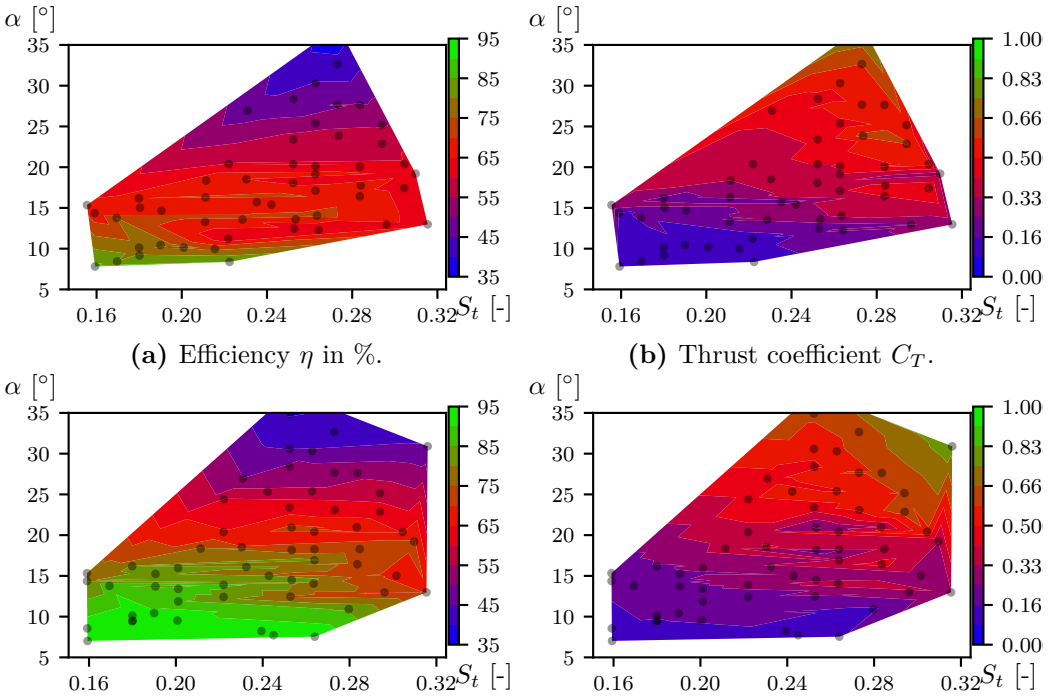

(a) Efficiency η in %.

(b) Thrust coefficient C_T.

(c) Efficiency η in %, frictionless

(d) Thrust coefficient C_T, frictionless

Figure 4.12: Contour-plots of the individuals tested at $Re_c \approx 19000$ with the highest efficiency inside the $S_T - \alpha$ grid.

4.3 Angle of Attack Profile

To investigate the tendencies for each of the six motion-parameters is too complicated when all of them are adjusted simultaneously. Instead the angle of attack (AoA) profile is investigated, its variation through one oscillation is determined by a combination of all six motion-parameters. An attempt is made to compare the AoA profile at different thrust coefficients (C_T) with the generated forces, and power consumption. Only a selected set of results are compared, because the dataset is too large to investigate all profiles manually.

From the experiments at $Re_c \approx 40000$ four individuals which are the most efficient in a stepped range of thrust coefficients are selected. Their AoA profile is presented in Figure 4.13. Four different profiles can be identified: cosine for low thrust ($C_T = 0.08$), square for medium thrust ($C_T = 0.12\&0.15$), and Zig-Zag for high thrust ($C_T = 0.17$). High, medium, and low thrust is meant relative to what range of C_T was achievable with the given parameters in the test, where in example, Strouhal number is limited $S_t < 0.18$. To clarify; during optimisation the algorithm was enforced to investigate regions with very high and low thrust, even though they are inefficient, by setting a minimum or maximum acceptable thrust.

The generated force and power consumption through one oscillation for the four profiles in Figure 4.13 is illustrated in Figures 4.14, 4.15, 4.16, and 4.17. The foil is displaced through space in one oscillation, at nine positions it is illustrated with a rotated yaw angle. The x- and y-axis is dimensionless space with respect to foil chord ($c = 0.075\,\text{mm}$). The quiver-plots illustrate dimensionless resulting force acting at the time incident, defined in equation 4.2. The red and green circles refer to power consumption P, size determines its magnitude. With a red circle power is consumed, and for a green circle, it is regenerated, meaning that force and velocity have the same direction.

$$C_R = \frac{\sqrt{F_d^2 + F_l^2}}{0.5\ \rho\ c\ s\ u_{inf}^2} \tag{4.2}$$

where C_R is the resultant force coefficient, F_d the drag force, F_l the lift force, c foil chord, s foil span, u_{inf} inflow velocity, and ρ the water density.

The most obvious trend is that the overall forces are increasing with the mean generated thrust coefficient. For the Zig-Zag profile (figure 4.17), power consumption is varying significantly in size through one oscillation, compared to the two other profiles. This causes also the forces to have large peaks, although this does not have a large impact on efficiency, the highly dynamic varying forces and energy requirement could put a lot of strain on machinery for a full scale ship.

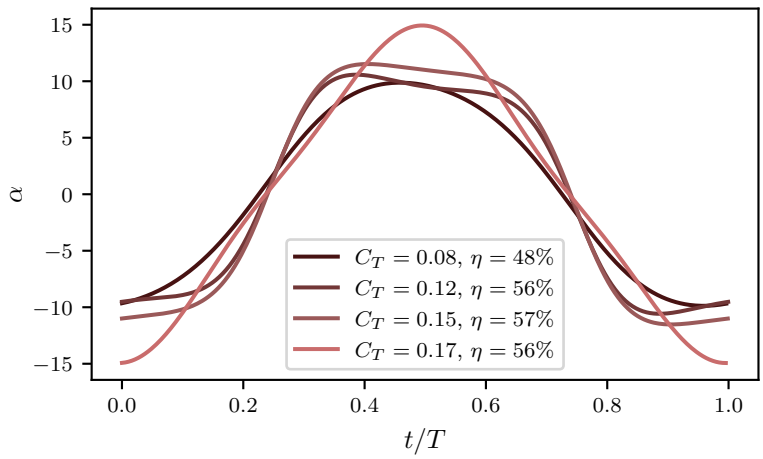

Figure 4.13: Four of the most efficient AoA profiles at different thrust coefficients, tested at $Re_c \approx 40000$. Four different profiles are identified, cosine for low thrust ($C_T = 0.08$), square for medium thrust ($C_T = 0.12\&0.15$), and Zig-Zag for high thrust ($C_T = 0.17$).

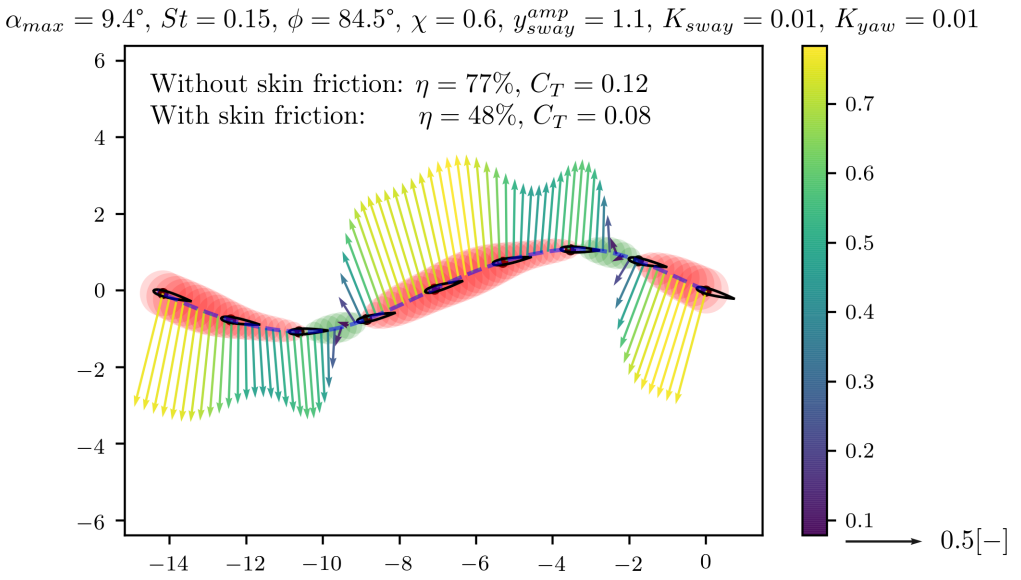

Figure 4.14: Foil-quiver plot of the cosine AoA-profile with lowest thrust in Figure 4.13. The arrows denote how the resultant force coefficient (Equation 4.2) varies in amplitude and direction through one oscillation. The size of the circles denote power consumption at the time incident, when the circle is green, energy is regenerated.

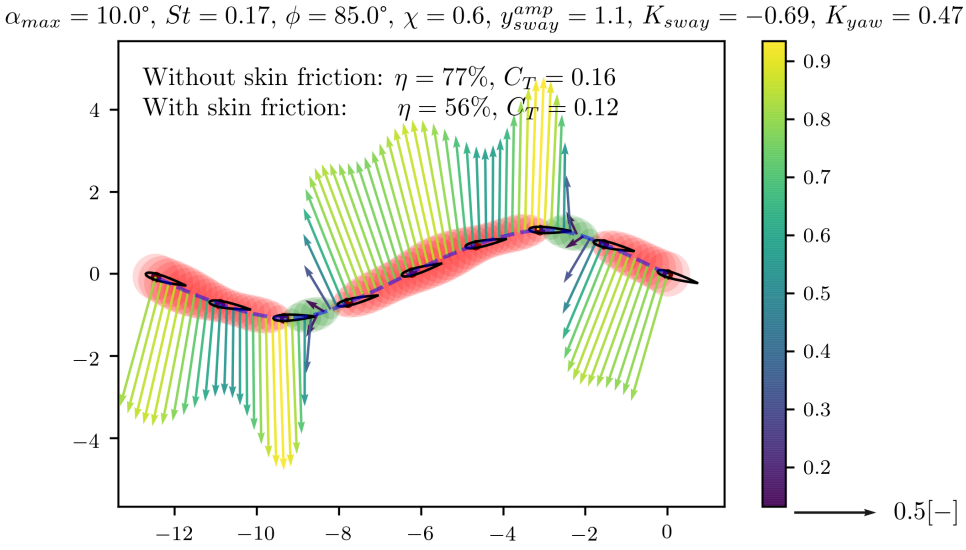

Figure 4.15: Foil-quiver plot of the square AoA-profile with thrust $C_T = 0.12$ in Figure 4.13. The arrows denote how the resultant force coefficient (Equation 4.2) varies in amplitude and direction through one oscillation. The size of the circles denote power consumption at the time incident, when the circle is green, energy is regenerated.

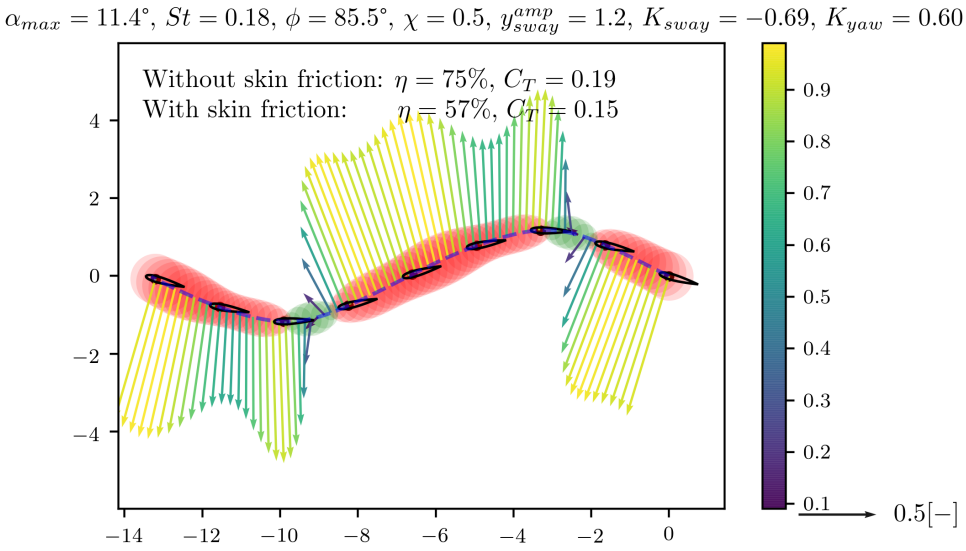

Figure 4.16: Foil-quiver plot of the square AoA-profile with thrust $C_T = 0.15$ in Figure 4.13. The arrows denote how the resultant force coefficient (Equation 4.2) varies in amplitude and direction through one oscillation. The size of the circles denote power consumption at the time incident, when the circle is green, energy is regenerated.

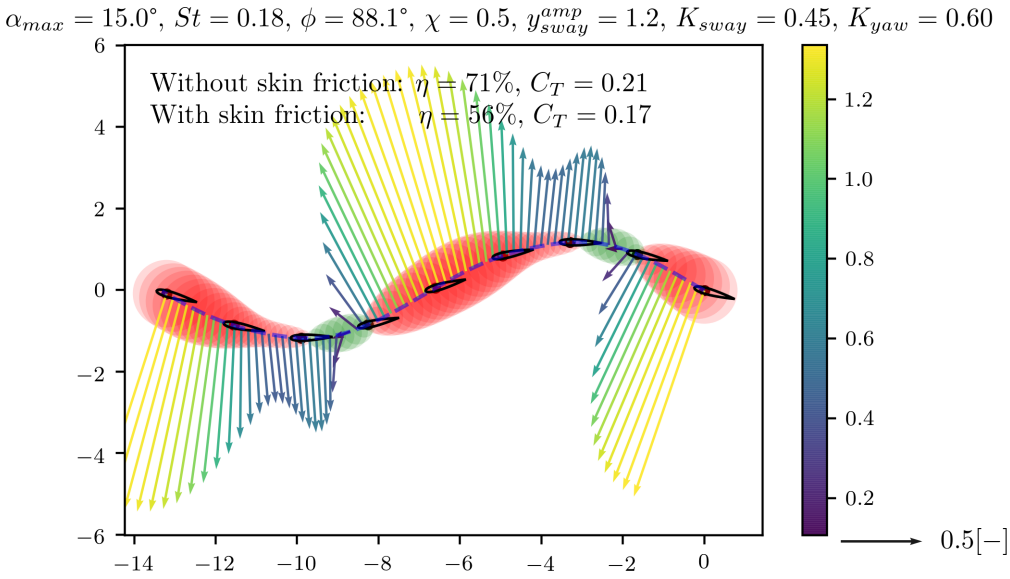

Figure 4.17: Foil-quiver plot of the square AoA-profile with thrust $C_T = 0.17$ in Figure 4.13. The arrows denote how the resultant force coefficient (Equation 4.2) varies in amplitude and direction through one oscillation. The size of the circles denote power consumption at the time incident, when the circle is green, energy is regenerated.

4.3.1 Phase

Another interesting tendency is that the phase (ϕ) for all four profiles is slightly below 90°. Which is similar to the findings of J. Anderson et al. (1998), although they tested a large phase difference of 75°, they indicated that higher efficiencies coincide for phases below 90°.

As an illustration, the phases for all tested individuals are plotted in Figure 4.18. For the efficiency (η) value, skin friction is removed, such that cases with and without turbulence stimulation (TS) can be compared. At efficiencies above 80% almost all individuals have a phase below 90°. Especially for the case at $Re_c = 19000$, here phase is typically around 75°. Note that for this case high S_t values are tested, and reverse Von Kármán Vortex Street can form according to J. M. Anderson (1996).

To investigate the phase difference further, two individuals at $Re_c \approx 19000$ with similar motion parameters are identified. The main difference is the phase, with $\phi = 76.4°$ the efficiency is 72%, when the phase is changed slightly to $\phi = 80.6°$, efficiency is reduced to 57%. In Figure 4.19 it is illustrated how thrust and power consumption varies when the angle of attack crosses 0°. The slight change in phase has caused a reversed thrust force at this inflection point. which could explain a reduction in efficiency and thrust. In addition it proposes that motions with high efficiency are very susceptible to slight changes.

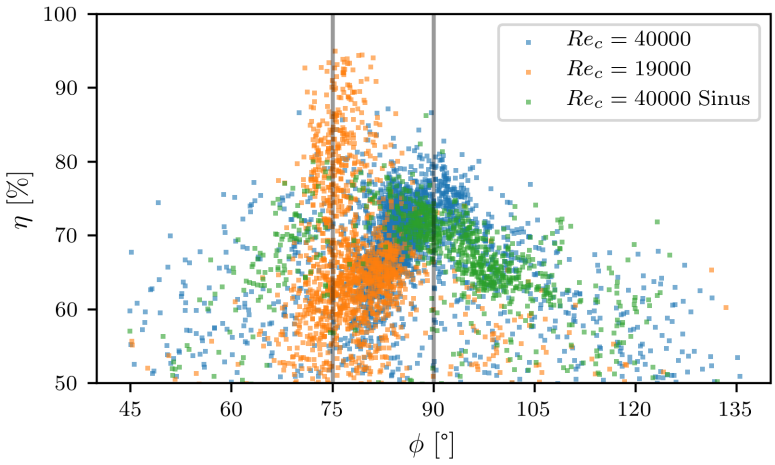

Figure 4.18: Phase difference plotted against efficiency without skin friction for all three cases. The general tendency for high efficiency is that the phase is below 90°. Especially for the case at $Re_c = 19000$ where high Strouhal numbers are tested.

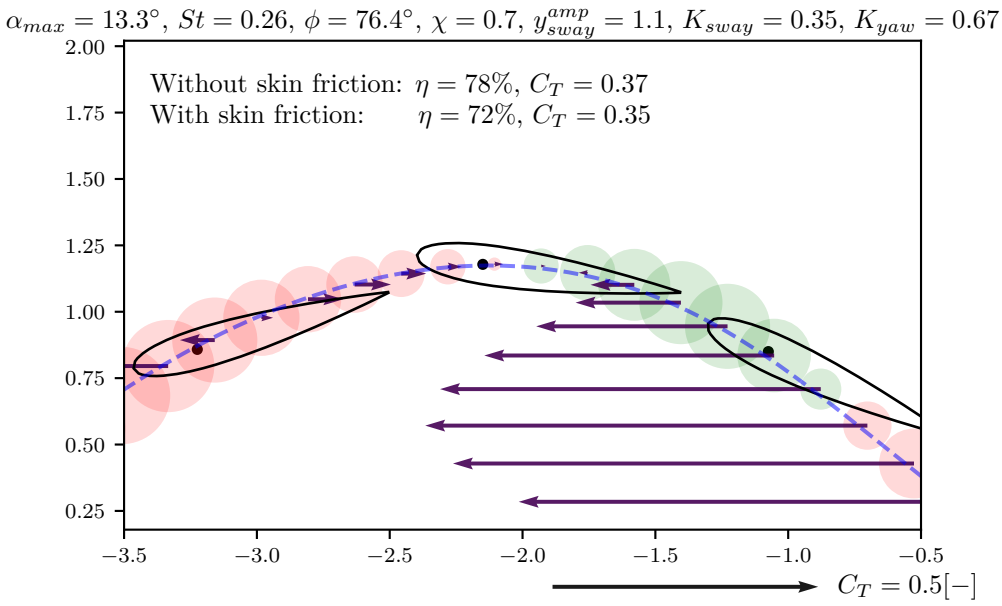

(a) Optimal

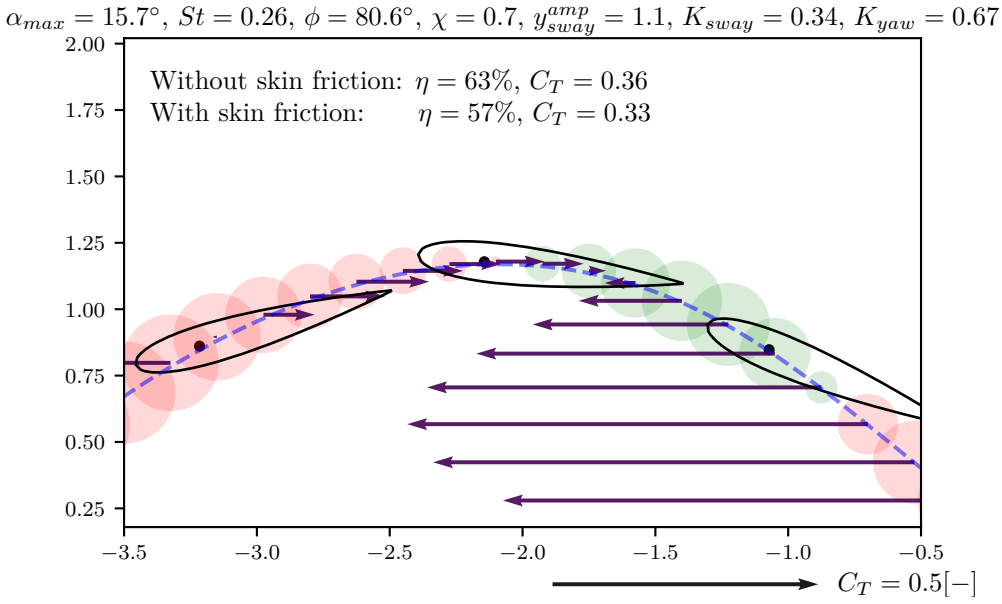

(b) Slight change in phase, reversed thrust force at $x = -1.5$ to -3, this could explain lower efficiency and mean C_T.

Figure 4.19: Thrust force coefficient and power consumption for two similar cases, with a slight change in phase (ϕ). The size of the circles denote power consumption at the time incident, when the circle is green, energy is regenerated. The arrows denote the thrust coefficient at the time incident.

4.4 Uncertainty Analysis

To investigate the uncertainty in measured thrust (C_T) and efficiency (η), approximately 3 % of all individuals illustrated as scatter dots in Figures 4.3, 4.4 and 4.5 are repeated 10 times each. The precision error for C_T and η is then found with the methods described in Subsection 2.4.2.

The precision error from each repeated test is illustrated as a error-bar cross. Where centre is the mean value, and width and height the 95 % confidence interval for C_T and η respectively. In Figure 4.22, 4.20, and 4.21 the error-bars are plotted as an overlay of a scatter-plot with all the tested individuals. Larger versions of the figures are available in Appendix C, E, and G.

A clear tendency is that the higher mean thrust $\overline{C_T}$ is measured, the lower is the precision error for efficiency (η). Surprisingly is the difference in uncertainty for C_T independent of the mean $\overline{C_T}$ value. According to Equation (2.5) is the thrust coefficient only dependent on the measured forces, and yaw angle. Efficiency is in addition dependent on the measured power consumption in Equation (2.6), which is also based on acceleration from accelerometers, yaw torque ($M_z(t)$), sway velocity ($\frac{dy}{dt}$), and yaw rate ($\frac{d\theta}{dt}$) derived from the pot-meter and sway position sensor. A lot more sensors are therefore contributing to a precision error on measured efficiency.

For tests at $Re_c \approx 19000$ in Figure 4.22, the precision error in efficiency is especially high for $C_T < 0.15$, its 95% confidence interval is measured at ± 5 in efficiency percentage. Apart from this, the precision error is in general acceptable, and mostly within a 5% relative error.

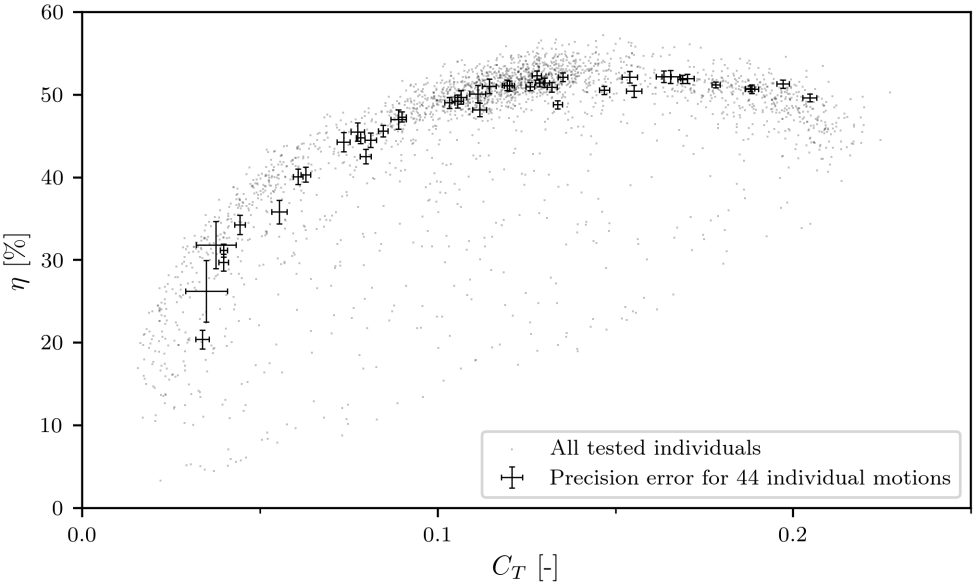

Figure 4.20: Precision error for 44 selected individual motions of the optimisation runs at $Re_c \approx 40000$. In general very low precision error for efficiency (η), and thrust coefficient (C_T). Two outliers with high precision error at very low C_T are detected, this is expected due to a very low Strouhal number (S_t) in those tests, and thereby low oscillating frequency.

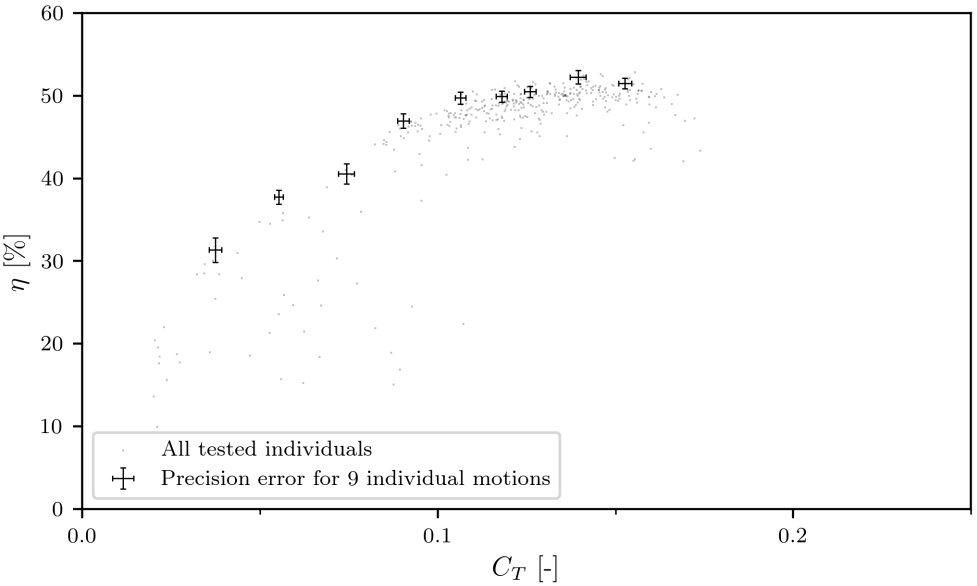

Figure 4.21: Precision error for 9 selected individual motions of the optimisation runs at $Re_c \approx 40000$ for sinusoidal motions only (K_y, and K_θ enforced to 0). Very low precision error for all 9 individuals.

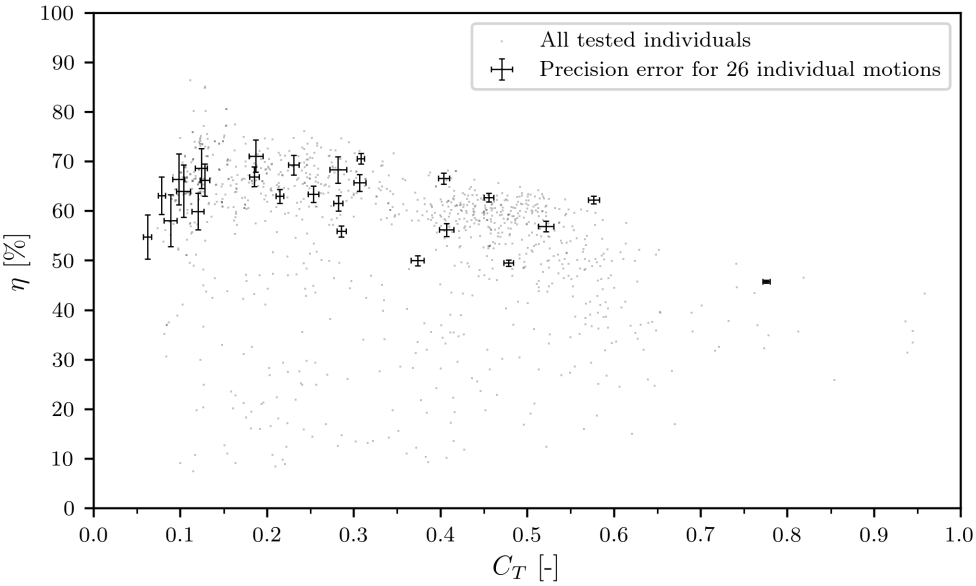

Figure 4.22: Precision error for 26 selected individual motions of the optimisation runs at $Re_c \approx 19000$. Tendency is that low precision error exists for measured C_T, precision error for efficiency (η) is higher at low thrust coefficients.

Chapter 5

Conclusion

For the model-scale experiments, successful turbulence stimulation (TS) has been utilized at $Re_c \approx 40000$. This is confirmed through tests with steady flow conditions. To cover a wider range of S_t, including the most optimal range observed in nature (Taylor et al., 2003) and indicated by other research (Triantafyllou et al., 1993), two test-conditions are selected; $Re_c \approx 19000$ without TS, $Re_c \approx 40000$ with TS.

Good agreement for both test-conditions was found with the experiments from J. Anderson et al. (1998), if drag force is zeroed with inflow-velocity (friction drag is removed). The highest reported efficiency could not be repeated, which also was the same conclusion as by Read et al. (2003). The highest efficiency measured by J. Anderson et al. (1998) which was successfully repeated is measured at $\eta \approx 80\%$.

Efficiencies above 90% were measured after optimisation at $Re_c \approx 19000$, although the uncertainty analysis indicated high precision error for this test-condition when thrust coefficient is small $C_T < 0.15$. Efficiencies above 80% were measured up to $C_T < 0.4$, this is a significant improvement from the experiments by J. Anderson et al. (1998), if case 1, which could not be repeated is discarded.

At $Re_c \approx 40000$ two separate optimisation experiments were done; in one the K-parameters for non-sinusoidal motions were fixed to 0, causing a forced sinusoidal motion in sway and yaw. Through theses experiments it was determined that by introducing K-parameters and allowing non-sinusoidal motion, slightly higher thrust is achieved, and a overall increase of 5% thrust efficiency is observed.

The findings can be summarized to:

- Optimisation techniques can successfully be employed to optimize physical experiments in real-time.
- Correct execution of the experiments is confirmed by successfully repeating many of the most promenent results for oscillating hydrofoils by J. Anderson et al. (1998).
- High efficiencies are measured ($\eta > 60\%$) for a large range of thrust coefficients.

  When thrust coefficient is below $C_T < 0.35$, efficiencies above $\eta > 80\%$ are observed if skin-friction is subtracted.

  Highest efficiency is usually observed when maximum angle of attack (α_{max}) is much higher than static stall angle, and is increased with increasing Strouhal number (S_t).

  A tendency is that for high thrust efficiency, the phase between sway and yaw is usually below 90°. When Strouhal numbers higher than $St > 0.18$ are tested, the phase is around 75°.

  High efficiency is extremely susceptible to minor changes in motion, it was observed that when phase changed by 4°, the efficiency reduced from 72% to 57%.
- Skin friction is very important at low thrust coefficients, and can cause a large degradation of efficiency.
- Only minor improvement in thrust-efficiency by utilising non-sinusoidal sway and yaw motion.

5.1 Recommendations for Further Work

The thrust efficiency optimisation has shown promising results. However, the data generated is enormous and in this thesis it was focused on analysing the resulting efficiency and thrust. An attempt was made to investigate what values are ideal for motion-parameters, and how power-consumption and thrust varies through an oscillation. This can be investigated further with the same dataset. Attached to this thesis is a *.csv* file, which contains information on all motions tested. Unfortunately does not NTNU support data-hosting for master theses. Time-series and raw-data are therefore available on request, people who have a copy of the data are listed in Table 5.1.

In Chapter 1, Introduction, it was mentioned that no literature was found where yaw and sway motions on thunniform swimmers is measured. It would be very interesting to see if there is some relationship between the motion optimised with a genetic algorithm, and natural selection.

In addition the following topics could be of interest:

- Optimisation with drag correction. Drag was included in the optimisations for this thesis, it was observed that drag has a very high impact for low thrust-coefficients. Maybe are other motions efficient in this thrust range.
- Turbulence stimulation with different thickness. Time was limited for this thesis, and only one geometry for turblence stimulation was tested.
- Are laminar separation bubbles (LSB) really a problem for oscillating foils? Considering that only tests for steady flows were conducted in this tesis to evaluate their extend.

Table 5.1: Contact information on people who can provide the raw-data for the experiments presented in this thesis.

Name	Role	Phone	E-mail
Lennard Bösch	Author	+47 91850883	lenni1b@gmail.com
Thomas Gjerde	Master thesis collaboration	+47 95147266	thomasgjerde90@gmail.com
John Martin Kleven Godø	Co-Advisor	+47 90607515	john.martin.kleven.godo@gmail.com

References

Abbott, I. H., & Von Doenhoff, A. E. (1959). *Theory of wing sections, including a summary of airfoil data.* Courier Corporation.

Anderson, J., Streitlien, K., Barrett, D., & Triantafyllou, M. (1998). Oscillating foils of high propulsive efficiency. *Journal of Fluid Mechanics*, *360*, 41-72.

Anderson, J. M. (1996). *Vorticity control for efficient propulsion* (Unpublished doctoral dissertation). Massachusetts Institute of Technology.

Arena, A., & Mueller, T. (1980). Laminar separation, transition, and turbulent reattachment near the leading edge of airfoils. *AIAA journal*, *18*(7), 747-753.

Braslow, A. L., & Knox, E. C. (1958). *Simplified method for determination of critical height of distributed roughness particles for boundary-layer transition at mach numbers from 0 to 5.* National Advisory Committee for Aeronautics.

Bösch, L. (2016, 12). *Investigation of low-reynolds number scale effects for oscillating hydrofoil motions.* (7.5 ECTS project to initiate this master thesis)

Carmichael, B. (1981). Low reynolds number airfoil survey, volume 1.

Drela, M. (1989). Xfoil: An analysis and design system for low reynolds number airfoils. In *Low reynolds number aerodynamics* (p. 1-12). Springer.

Gjerde, T. (2017). *Optimizing bio-inspired propulsion systems using genetic algorithm [title subject to change]* (Unpublished master's thesis). Norwegian University of Science and Technology, Trondheim. (Available on: `http://brage.bibsys.no/xmlui/handle/11250/223328`)

Hoerner, S. F. (1965). *Fluid-dynamic drag: Practical information on aerodynamic drag and hydrodynamic resistence.* Sighard F. Hoerner.

Hover, F., Haugsdal, ., & Triantafyllou, M. (2004). Effect of angle of attack profiles in flapping foil propulsion. *Journal of Fluids and Structures*, *19*(1), 37-47.

Inglezakis, V. J., & Poulopoulos, S. G. (2006). Appendix i - physical properties of water, air and selected compounds. In *Adsorption, ion exchange and catalysis* (p. 551-573). Amsterdam: Elsevier.

ITTC-1978. (2008). *ITTC - Recommended Procedures and Guidelines. Performance, Propulsion 1978 ITTC Performance Prediction Method.* International Towing Tank Conference.

Kinsey, T., & Dumas, G. (2008). Parametric study of an oscillating airfoil in a power-extraction regime. *AIAA journal*, *46*(6), 1318-1330.

Knower, T. (1998). *Biomechanics of thunniform swimming* (Unpublished doctoral dissertation). Ph. D. Dissertation. University of California, San Diego.

Lighthill, M. (1970). Aquatic animal propulsion of high hydromechanical efficiency. *Journal of Fluid Mechanics*, *44*(02), 265–301.

Lu, K., Xie, Y., & Zhang, D. (2014a). Nonsinusoidal motion effects on energy extraction performance of a flapping foil. *Renewable Energy*, *64*, 283-293.

Lu, K., Xie, Y., & Zhang, D. (2014b). Numerical investigations into the nonsinusoidal motion effects on aerodynamics of a pitching airfoil. *Energy Procedia*, *61*, 2497-2500.

Mitchell, M. (1995). Genetic algorithms: An overview. *Complexity*, *1*(1), 31-39.

Mueller, T. J., & Batil, S. M. (1982). Experimental studies of separation on a two-dimensional airfoil at low reynolds numbers. *AIAA journal*, *20*(4), 457-463.

Read, D. A., Hover, F., & Triantafyllou, M. (2003). Forces on oscillating foils for propulsion and maneuvering. *Journal of Fluids and Structures*, *17*(1), 163–183.

Riegels, F. W. (1961). *Aerofoil sections.* Butterworths, London.

Schlichting, H., Gersten, K., Krause, E., Oertel, H., & Mayes, K. (1960). *Boundary-layer theory* (Vol. 7). Springer.

Selig, M. S., Guglielmo, J. J., Broeren, A. P., & Giguère, P. (1995). *Summary of low speed airfoil data* (Vol. 1). SoarTech.

Sfakiotakis, M., Lane, D. M., & Davies, J. B. C. (1999). Review of fish swimming modes for aquatic locomotion. *IEEE Journal of oceanic engineering*, *24*(2), 237-252.

Shyy, W., Lian, Y., Tang, J., Viieru, D., & Liu, H. (2007). *Aerodynamics of low reynolds number flyers* (Vol. 22). Cambridge University Press.

Steen, S. (2014). *Experimental methods in marine hydrodynamics.* Trondheim: Akademika forlag.

Syme, D. A., & Shadwick, R. E. (2011). Red muscle function in stiff-bodied swimmers: there and almost back again. *Philosophical Transactions of the Royal Society B: Biological Sciences*, *366*(1570), 1507-1515.

Taylor, G. K., Nudds, R. L., & Thomas, A. L. (2003). Flying and swimming animals cruise at a strouhal number tuned for high power efficiency [Journal Article]. *Nature*, *425*(6959), 707-711.

Triantafyllou, G. S., Triantafyllou, M., & Grosenbaugh, M. (1993). Optimal thrust development in oscillating foils with application to fish propulsion [Journal Article]. *Journal of Fluids and Structures*, *7*(2), 205-224.

Van Ingen, J. (2008). *The en method for transition prediction: historical review of work at tu delft.* AIAA.

Van Rooij, R., & Timmer, W. (2003). Roughness sensitivity considerations for thick rotor blade airfoils [Journal Article]. *Journal of solar energy engineering*, *125*(4), 468-478.

Yamaguchi, H., & Bose, N. (1994). Oscillating foils for marine propulsion. *Oscillating Foils for Marine Propulsion*, *3*, 539-544.

Yang, Z., Igarashi, H., Martin, M., & Hu, H. (2008). An experimental investigation on aerodynamic hysteresis of a low-reynolds number airfoil. In *46th aiaa aerospace sciences meeting and exhibit* (p. 315).

Young, D. F., Munson, B. R., Okiishi, T. H., & Huebsch, W. W. (2010). *A brief introduction to fluid mechanics.* John Wiley & Sons.

Appendix

B Summary of all Individuals Tested at $Re_c \approx 19000$

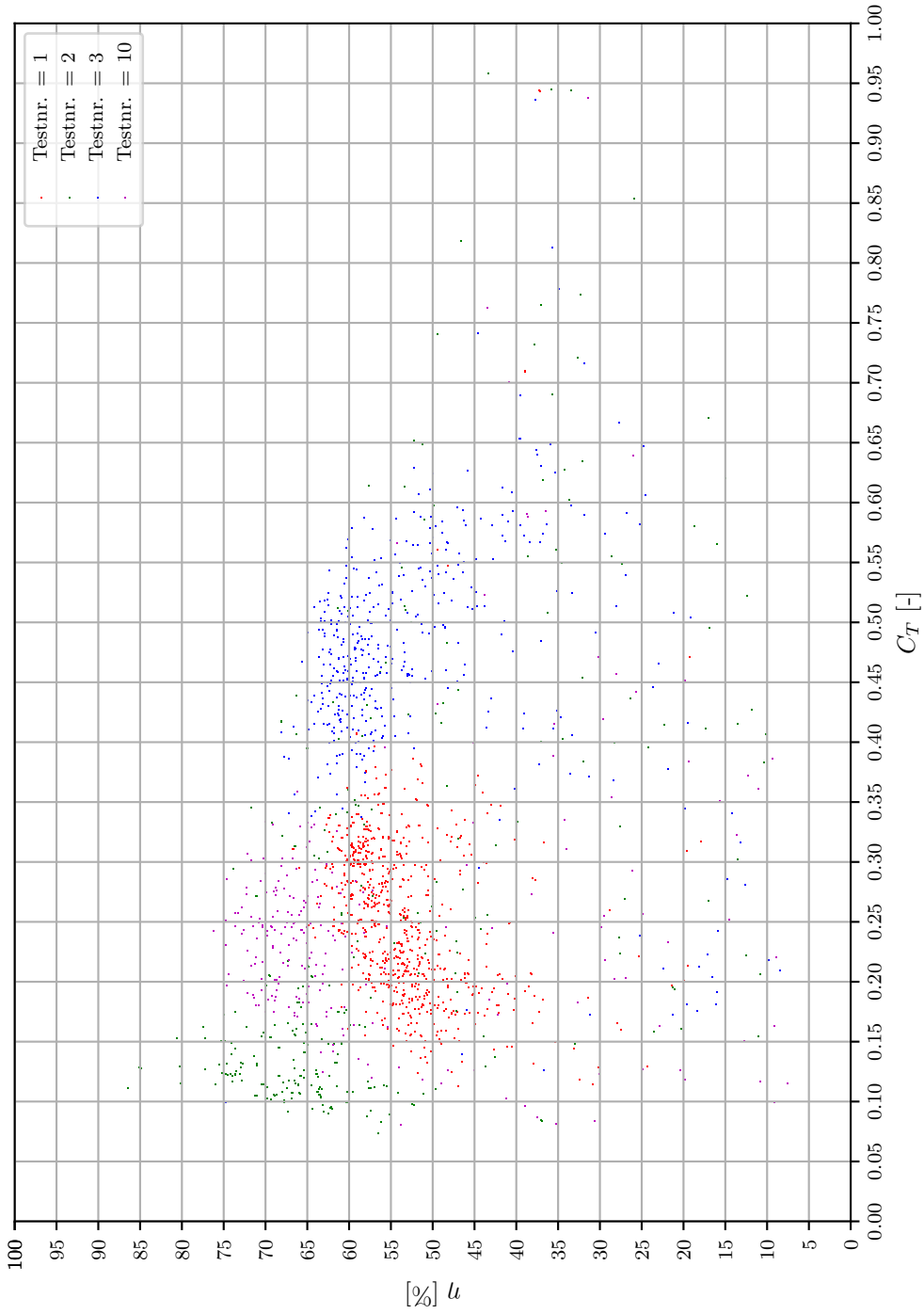

C Uncertainty analysis $Re_c \approx 19000$

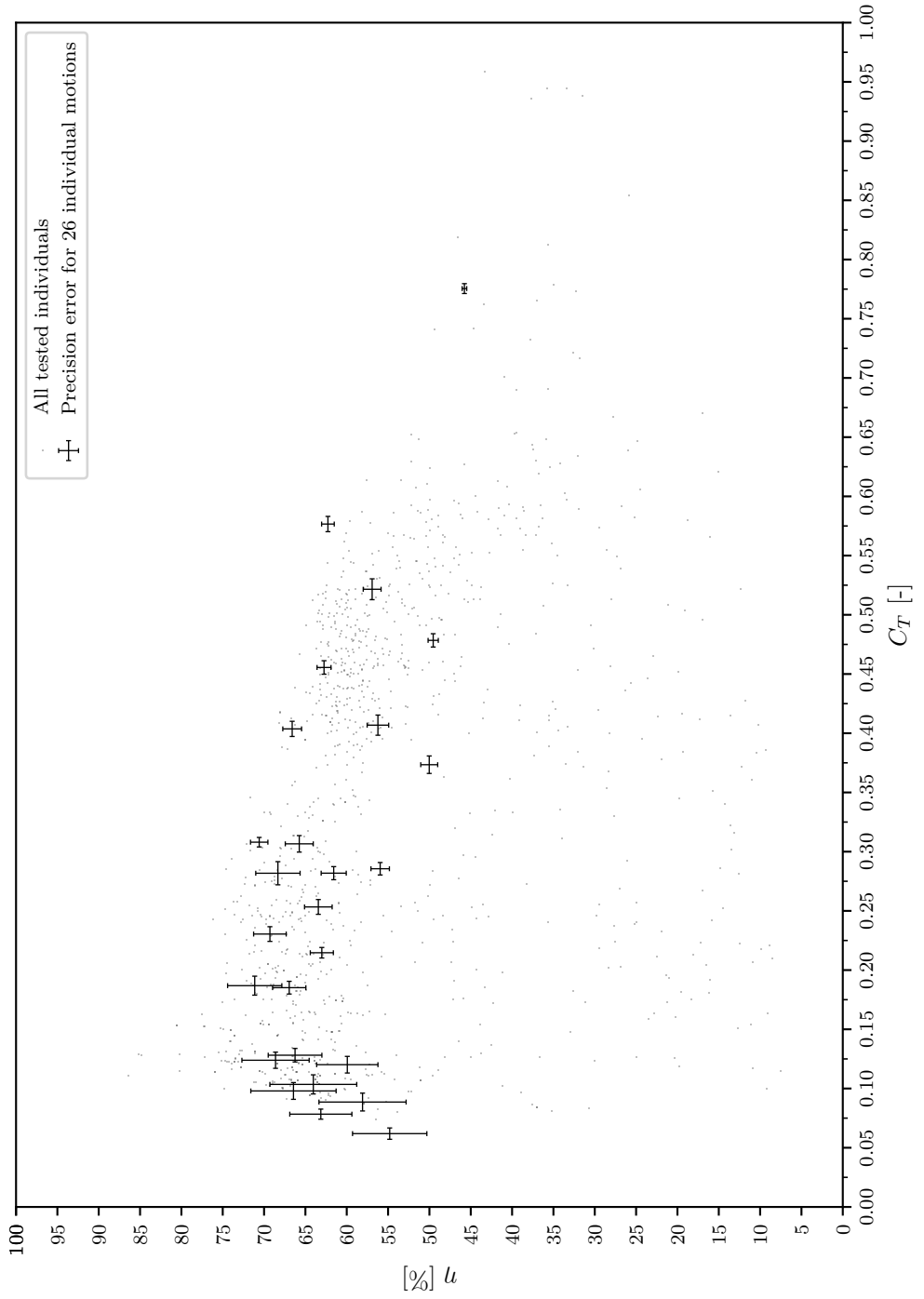

D Summary of all Individuals Tested at $Re_c \approx 40000$

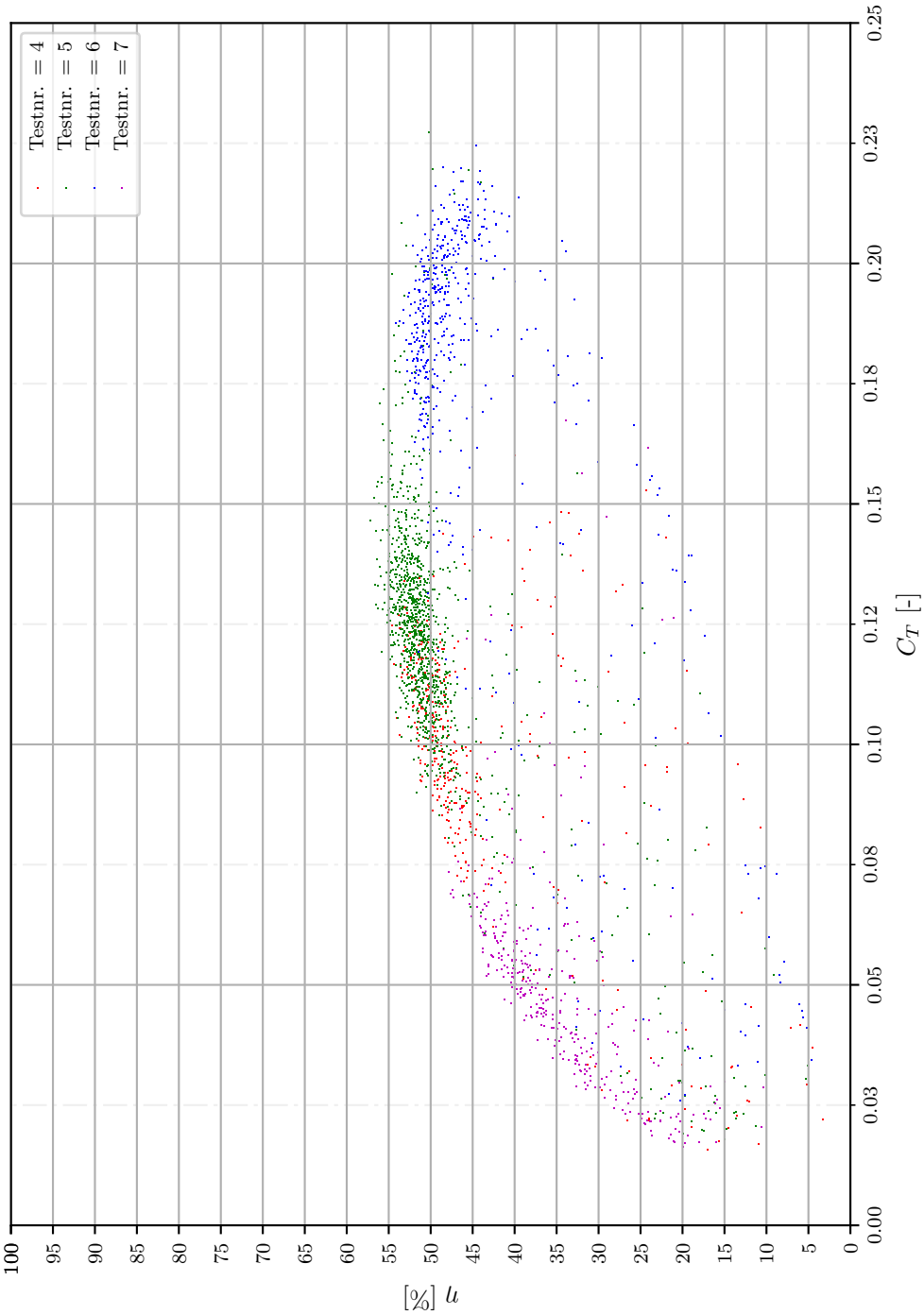

E Uncertainty analysis $Re_c \approx 40000$

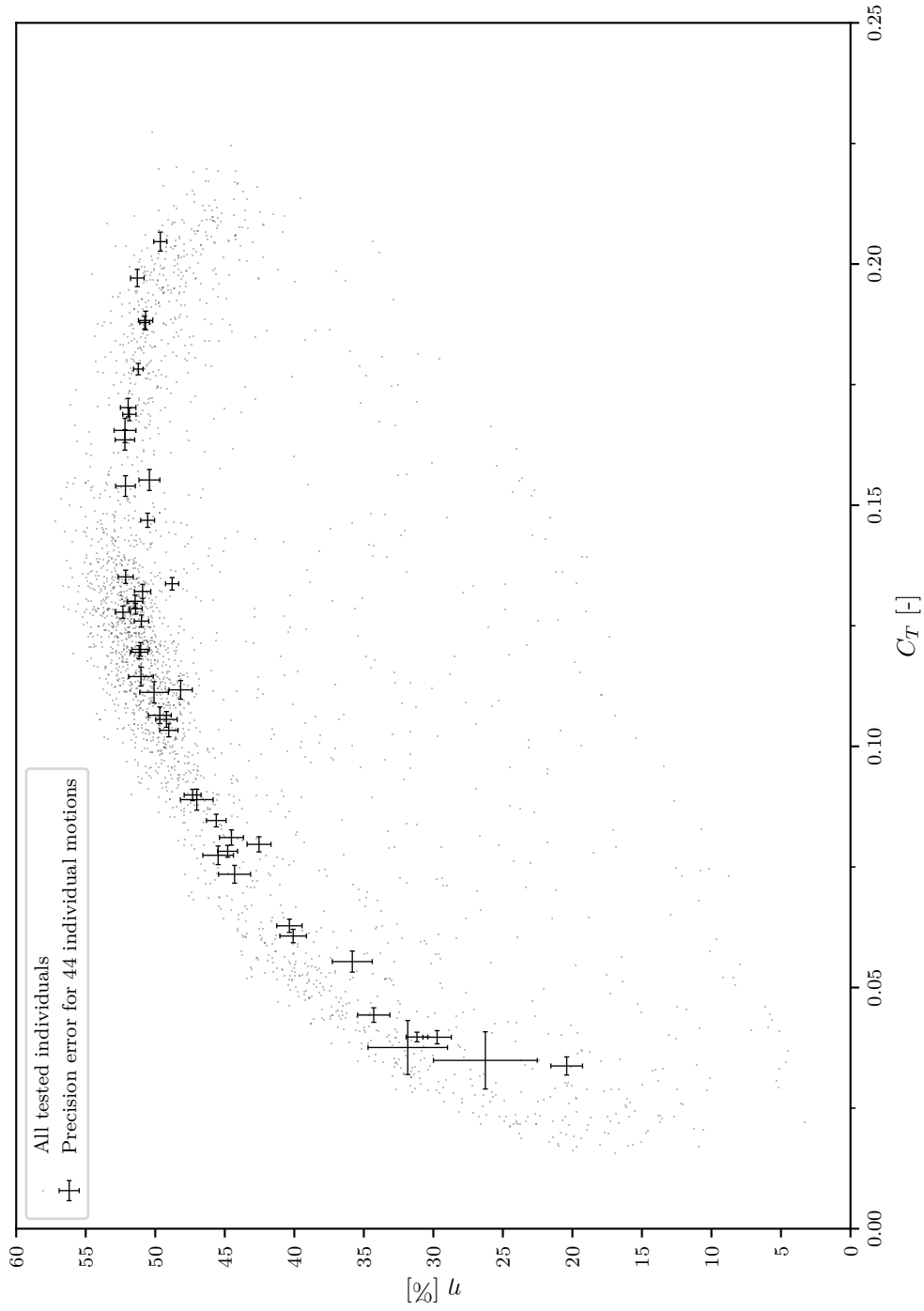

F Summary of all Individuals Tested at $Re_c \approx 40000$, with only sinusoidal motions allowed

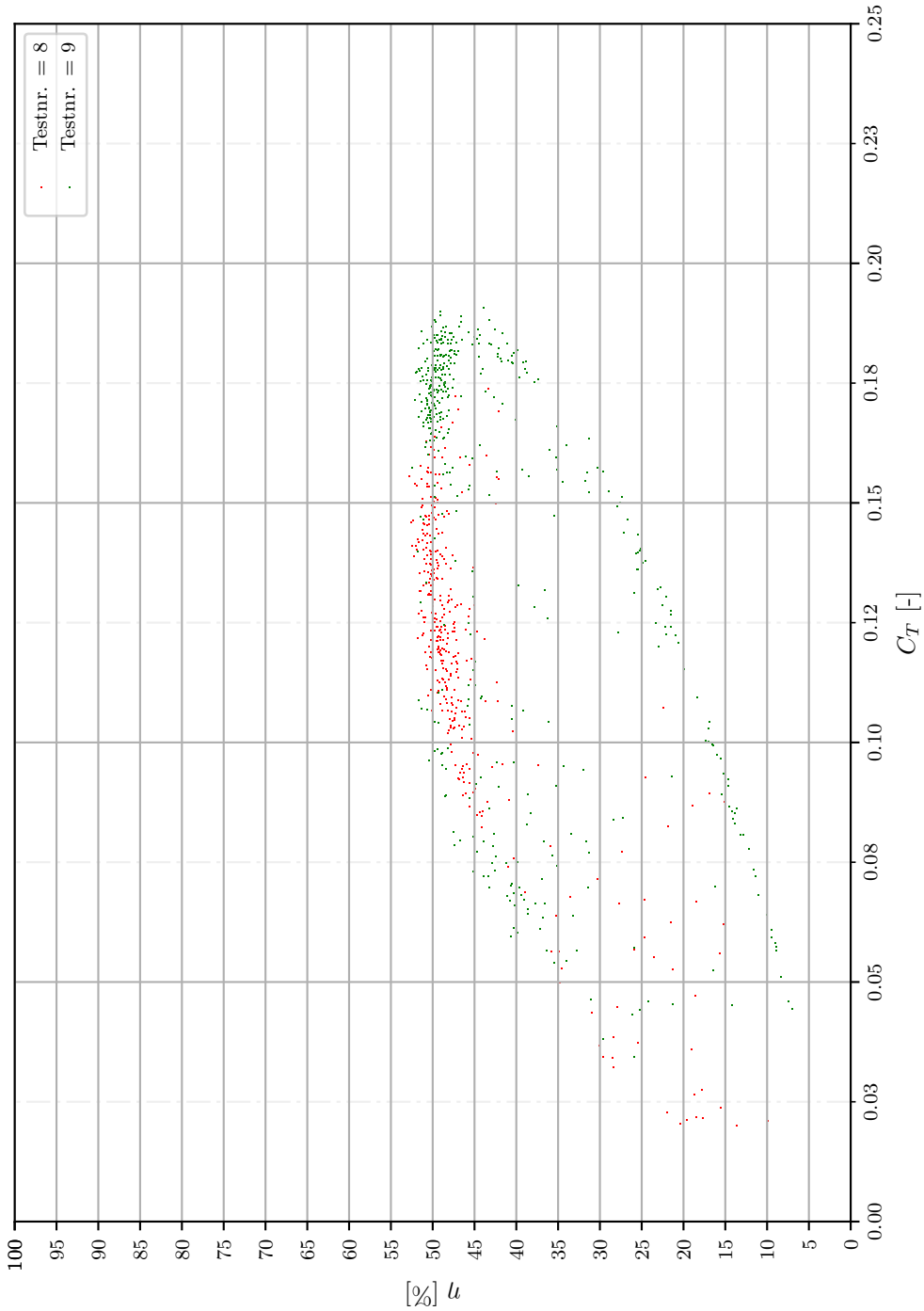

G Uncertainty analysis $Re_c \approx 40000$ sinus

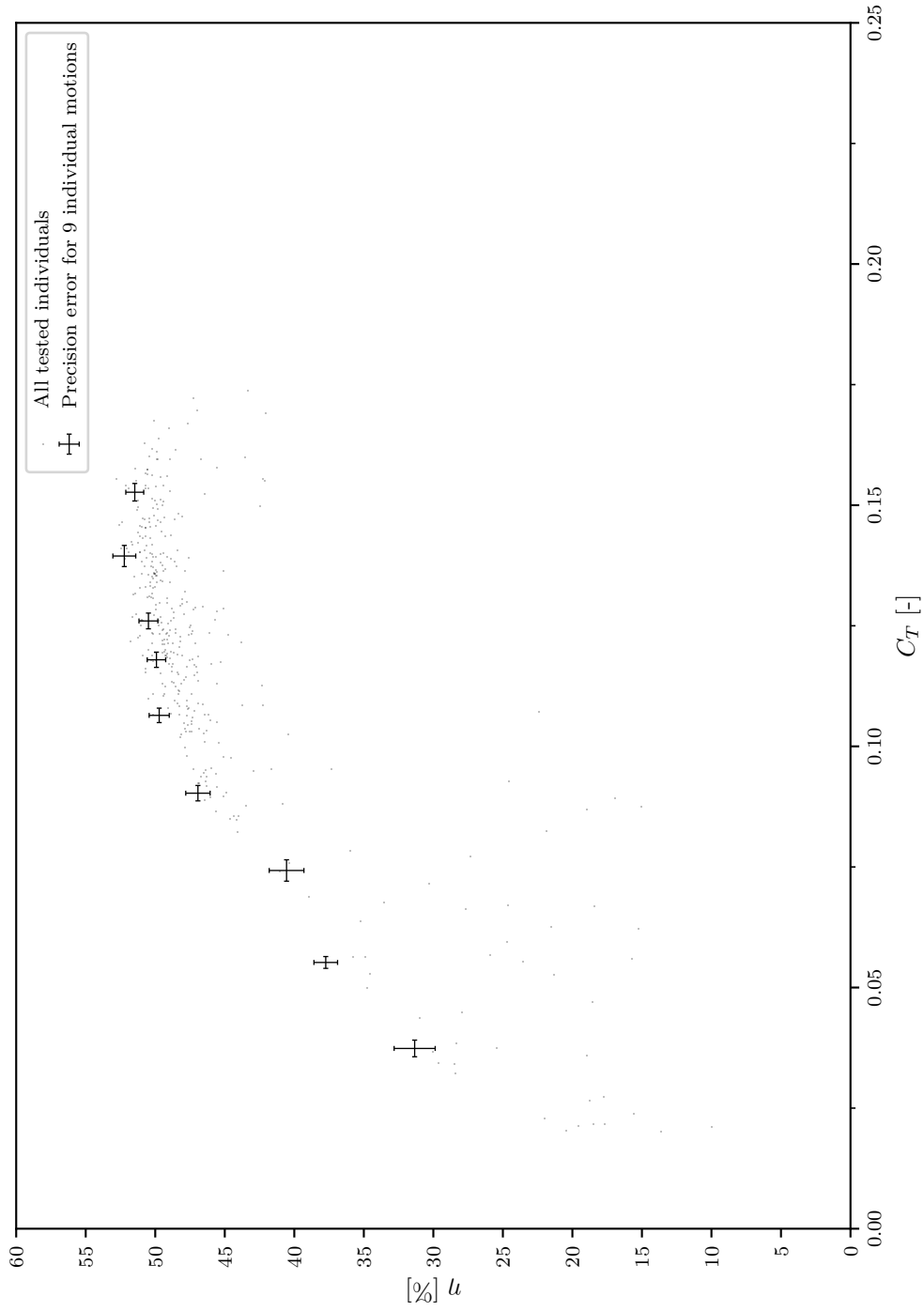

H Least-square fit of $\eta(C_T)$ function to test-data

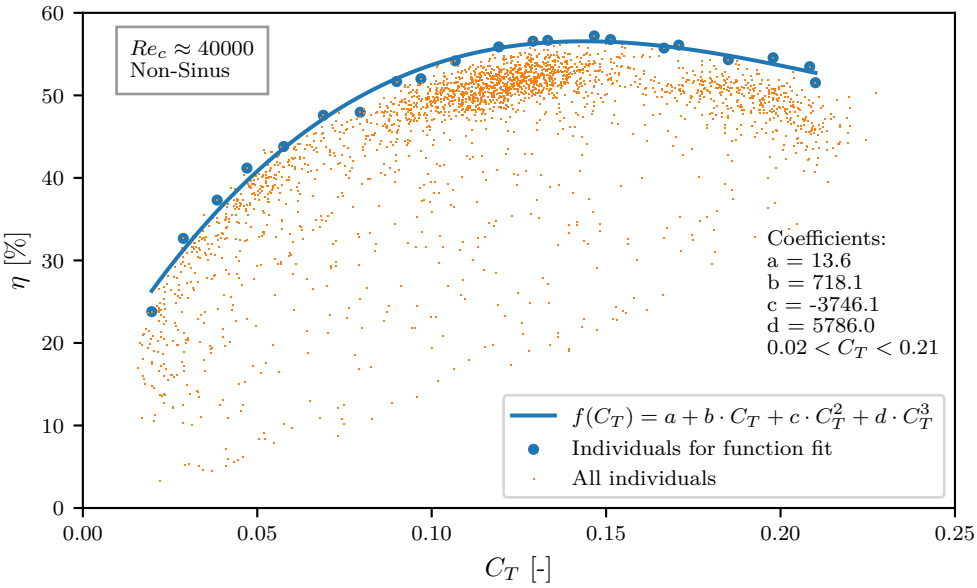

(a) With skin friction

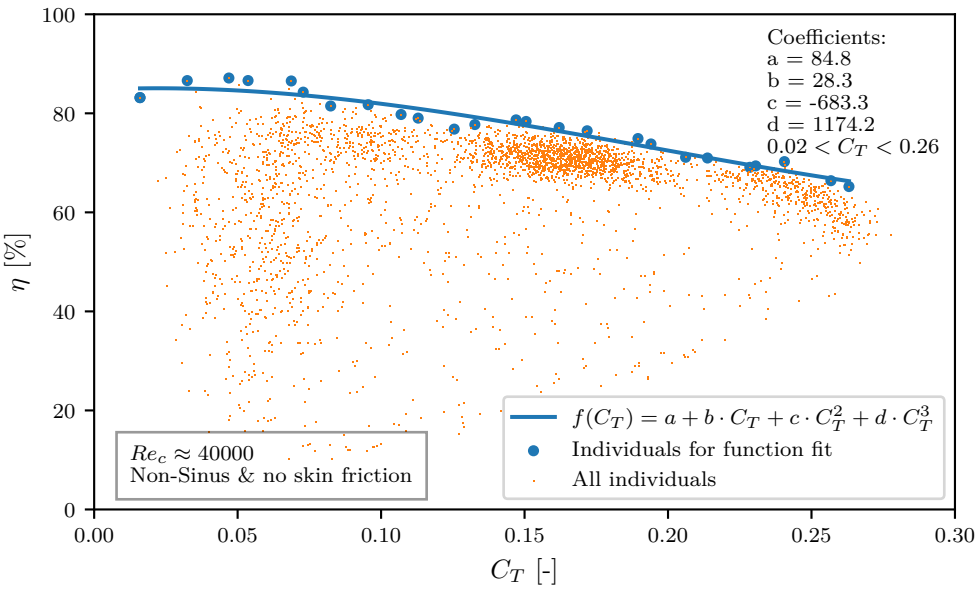

(b) Without skin friction

Figure H.1: Least square fit of equation 4.1 to the test-individuals with highest efficiency (η) for different thrust coefficients (C_T). The individuals are tested at $Re_c \approx 40000$, non-sinusoidal motion in sway and yaw is tested.

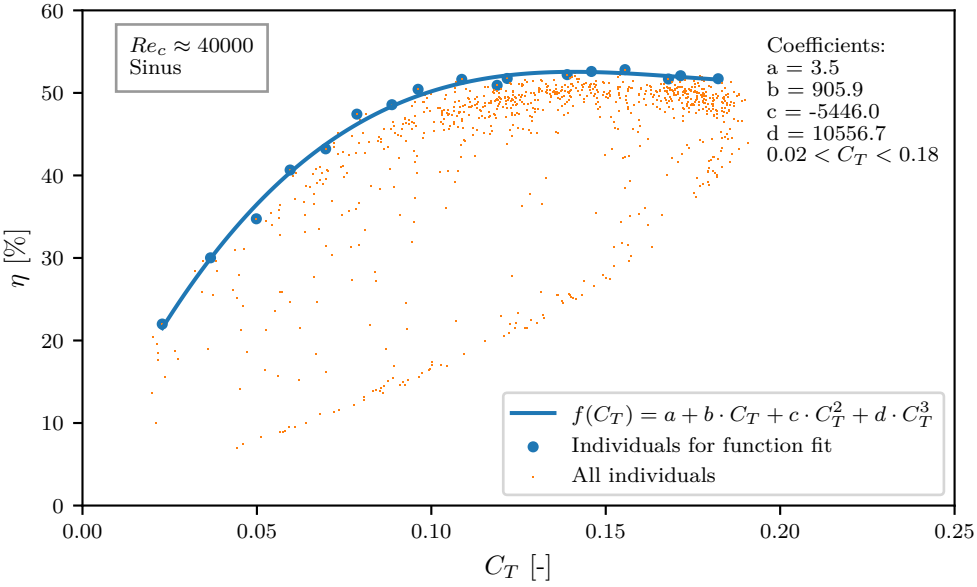

(a) With skin friction

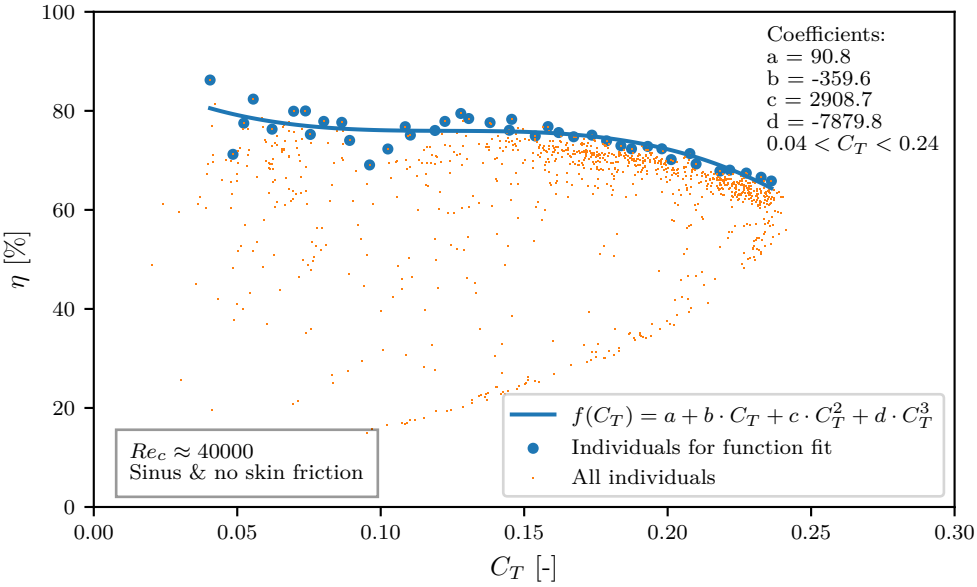

(b) Without skin friction

Figure H.2: Least square fit of equation 4.1 to the test-individuals with highest efficiency (η) for different thrust coefficients (C_T). The individuals are tested at $Re_c \approx 40000$, only sinus sway and yaw motion is tested.

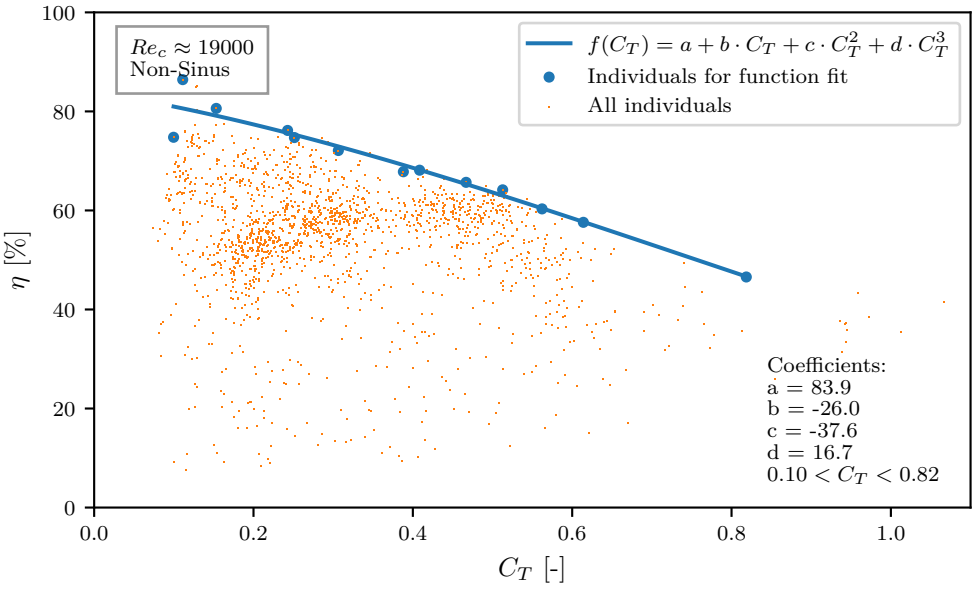

(a) With skin friction

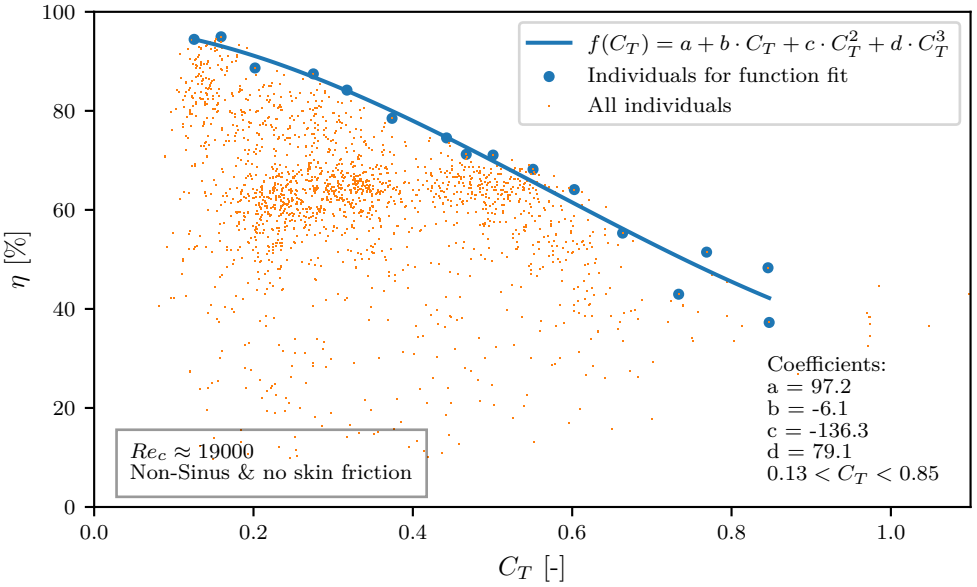

(b) Without skin friction

Figure H.3: Least square fit of equation 4.1 to the test-individuals with highest efficiency (η) for different thrust coefficients (C_T). The individuals are tested at $Re_c \approx 19000$, non-sinusoidal motion in sway and yaw is tested.

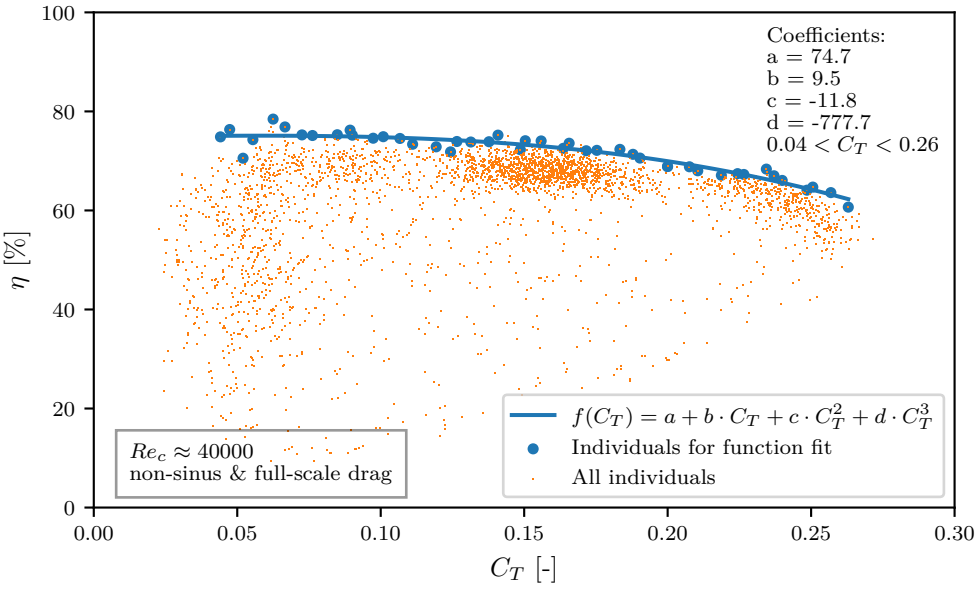

Figure H.4: Least square fit of equation 4.1 to the test-individuals with highest efficiency (η) for different thrust coefficients (C_T). The individuals are tested at $Re_c \approx 40000$, non-sinusoidal motion in sway and yaw is tested. The drag force is corrected to full-scale at $Re_c = 42 \times 10^6$.

I Repetition of Anderson et al. (1998) experiments

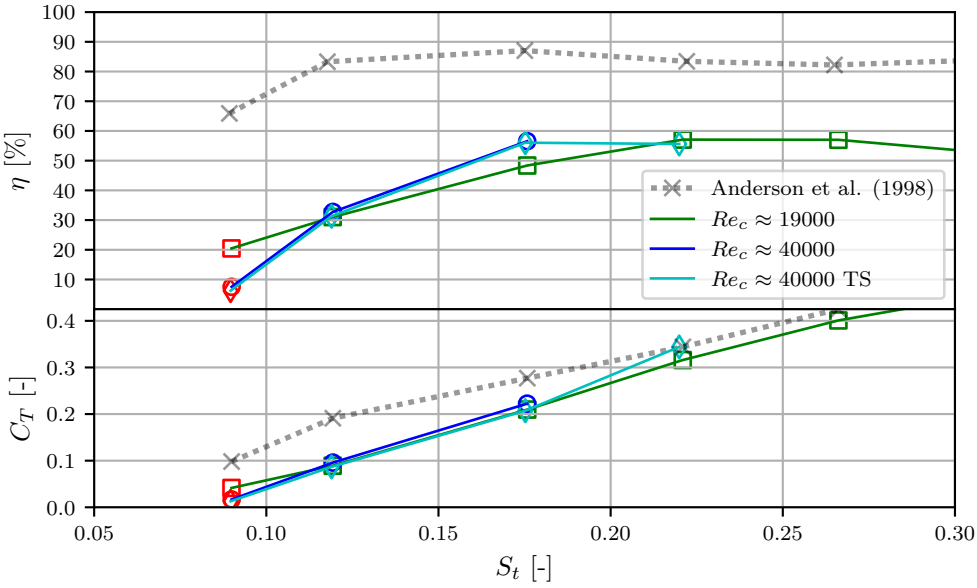

(a) Frictionless, drag zeroed with inflow-velocity.

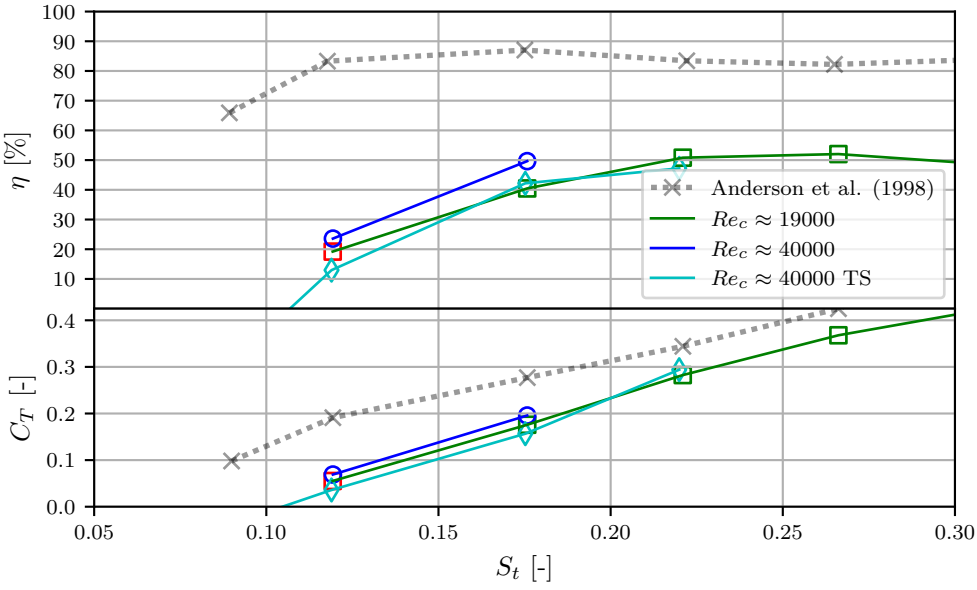

(b) Drag included, zeroed without inflow-velocity.

Figure I.1: Repetition of Anderson's case 1 with parameters: $\alpha_{max} = 21°$, $\phi = 75°$, $y^{amp}_{sway} = 0.75$.

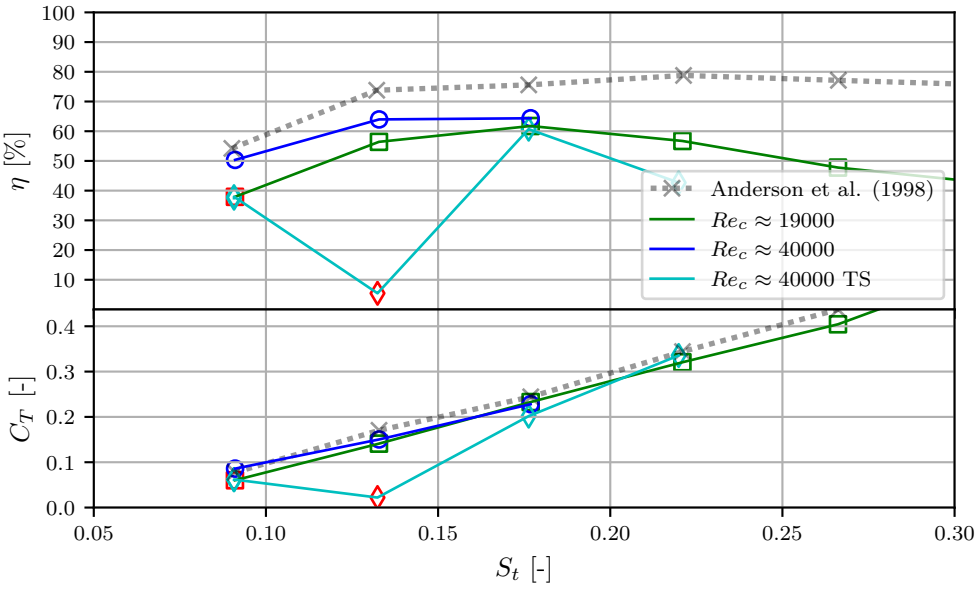

(a) Frictionless, drag zeroed with inflow-velocity.

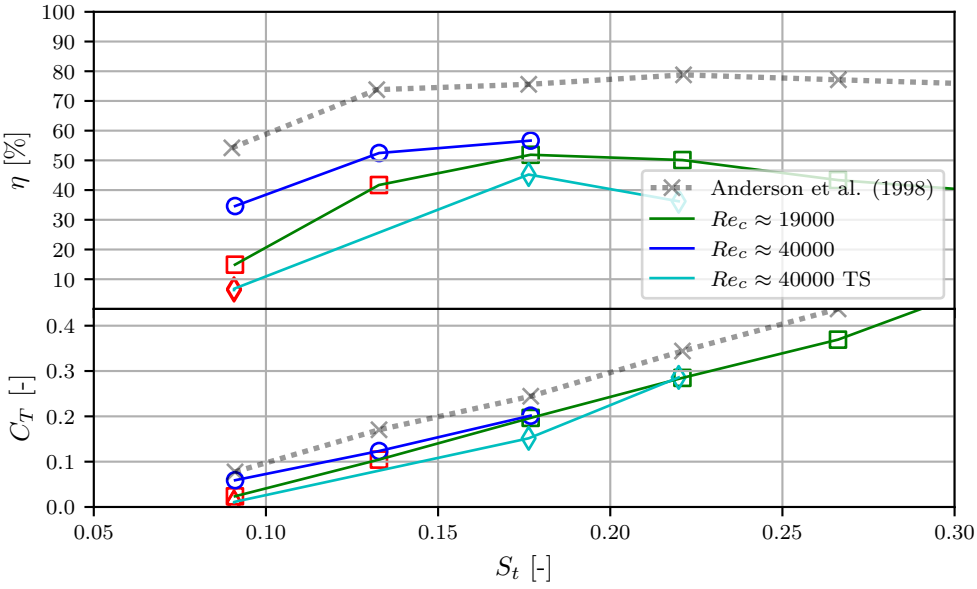

(b) Drag included, zeroed without inflow-velocity.

Figure I.2: Repetition of Anderson's case 2 with parameters: $\alpha_{max} = 17°$, $\phi = 105°$, $y_{sway}^{amp} = 0.75$.

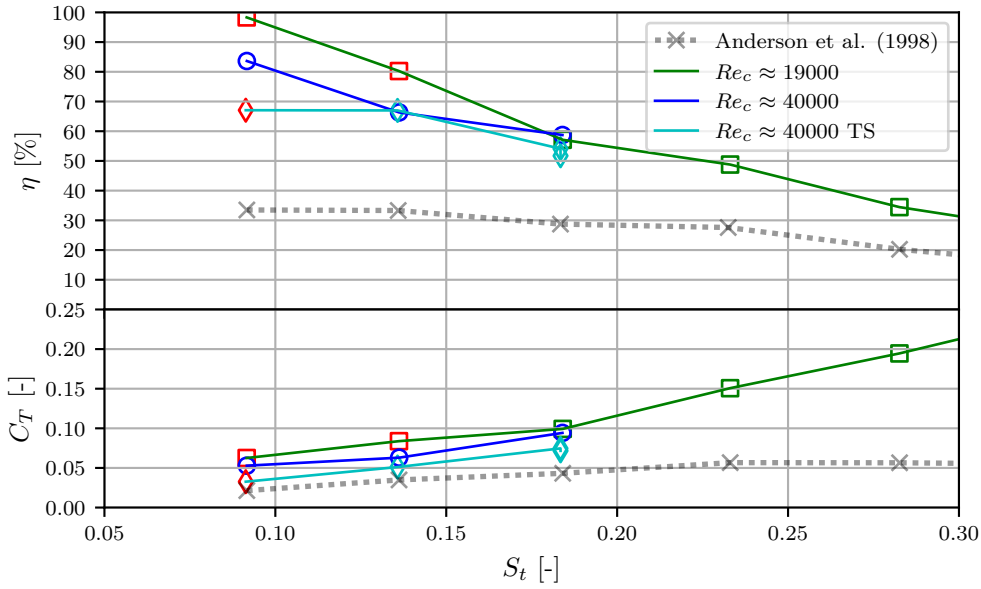

(a) Frictionless, drag zeroed with inflow-velocity.

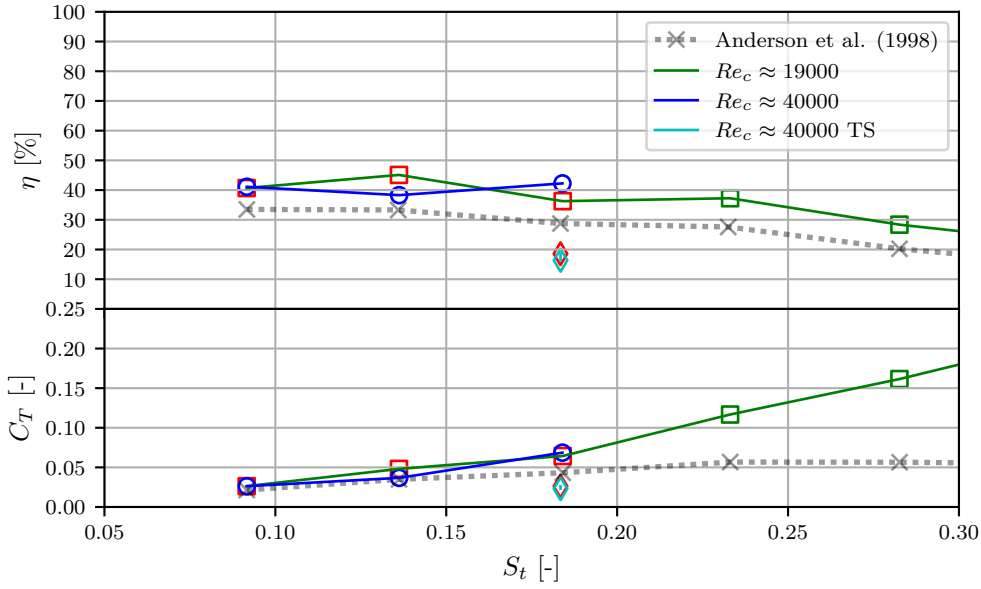

(b) Drag included, zeroed without inflow-velocity.

Figure I.3: Repetition of Anderson's case 4 with parameters: $\alpha_{max} = 5°$, $\phi = 90°$, $y^{amp}_{sway} = 0.75$.

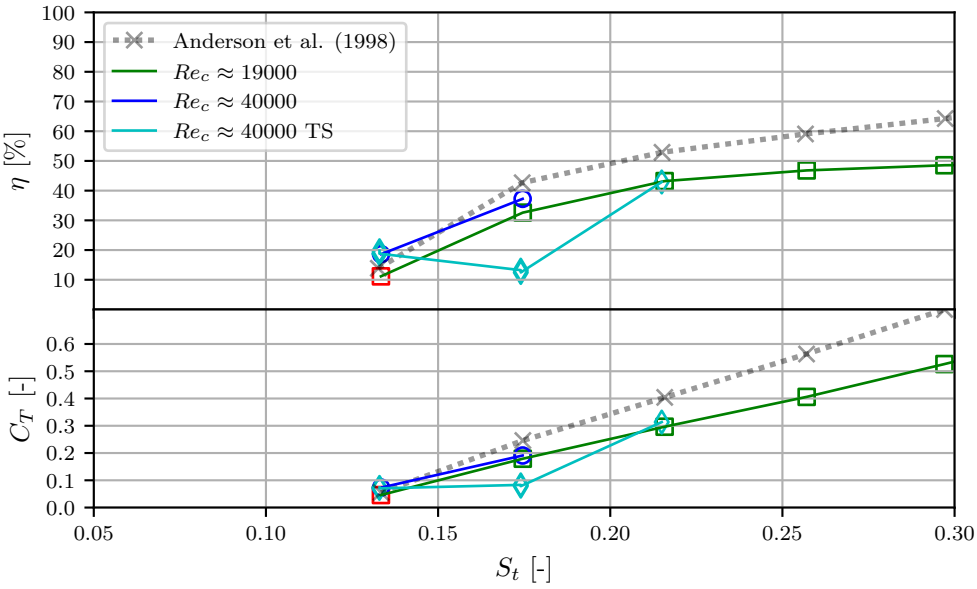

(a) Frictionless, drag zeroed with inflow-velocity.

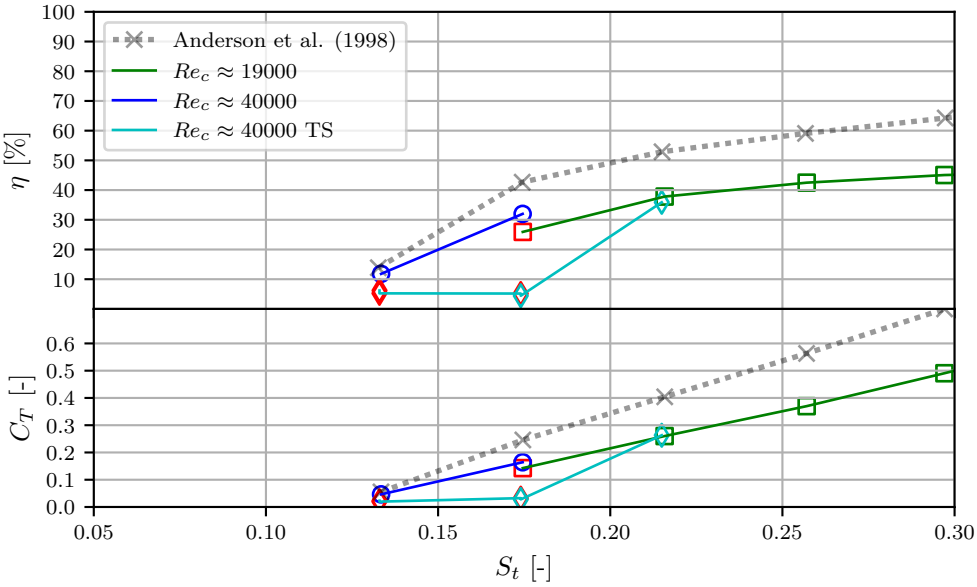

(b) Drag included, zeroed without inflow-velocity.

Figure I.4: Repetition of Anderson's case 5 with parameters: $\alpha_{max} = 25°$, $\phi = 90°$, $y_{sway}^{amp} = 0.75$.

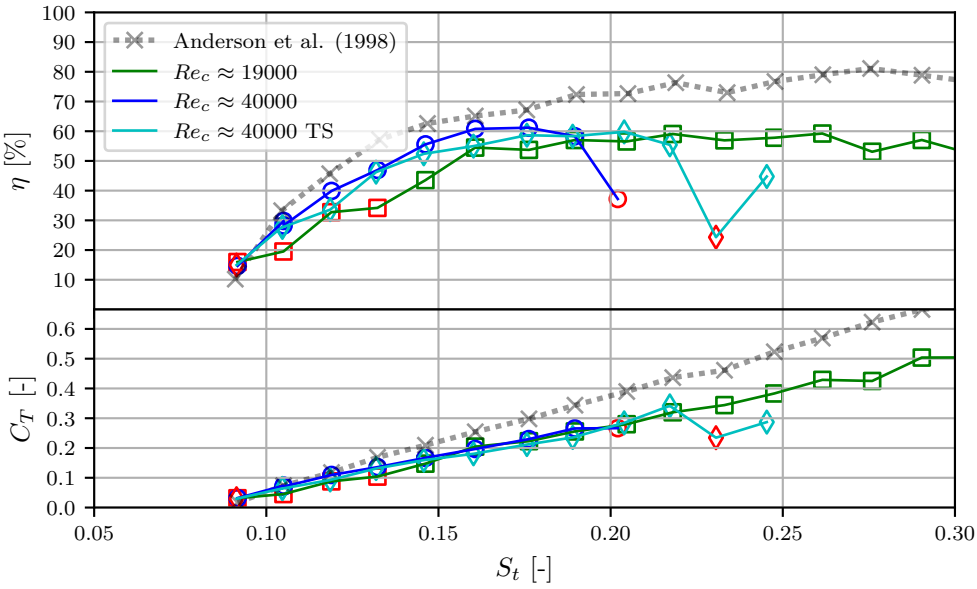

(a) Frictionless, drag zeroed with inflow-velocity.

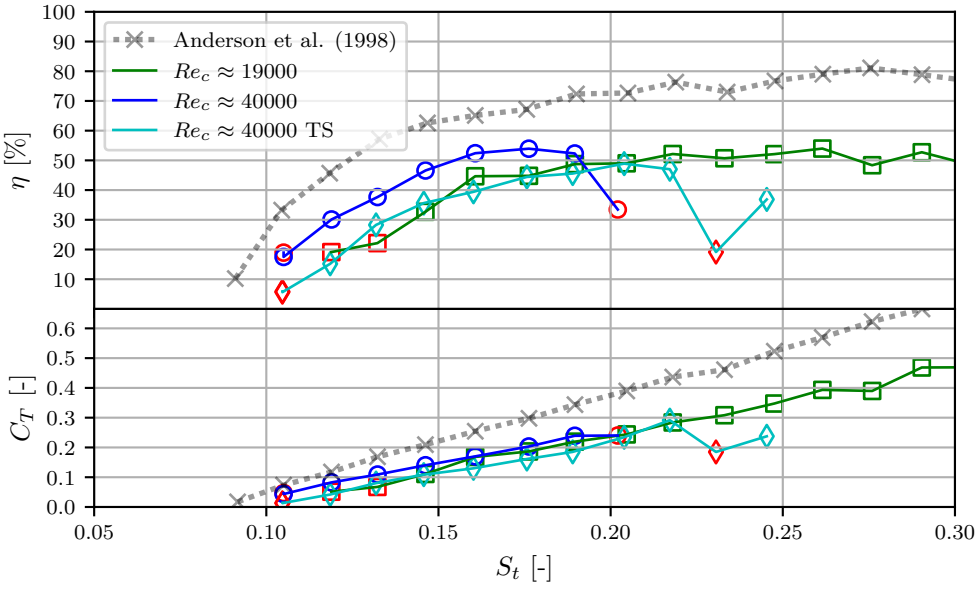

(b) Drag included, zeroed without inflow-velocity.

Figure I.5: Repetition of Anderson's case 6 with parameters: $\alpha_{max} = 20°$, $\phi = 90°$, $y_{sway}^{amp} = 0.75$.

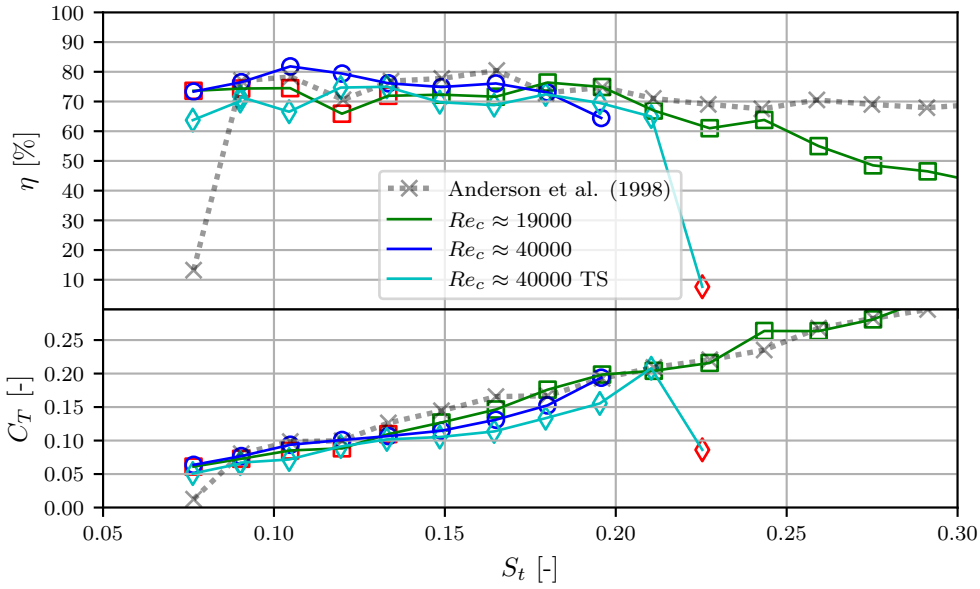

(a) Frictionless, drag zeroed with inflow-velocity.

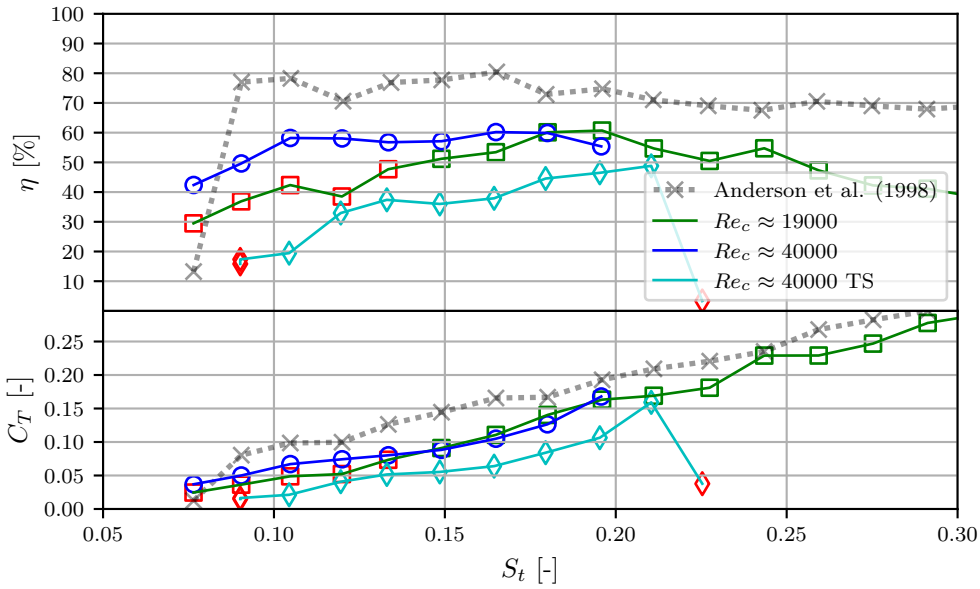

(b) Drag included, zeroed without inflow-velocity.

Figure I.6: Repetition of Anderson's case 7 with parameters: $\alpha_{max} = 10°$, $\phi = 90°$, $y_{sway}^{amp} = 0.75$.

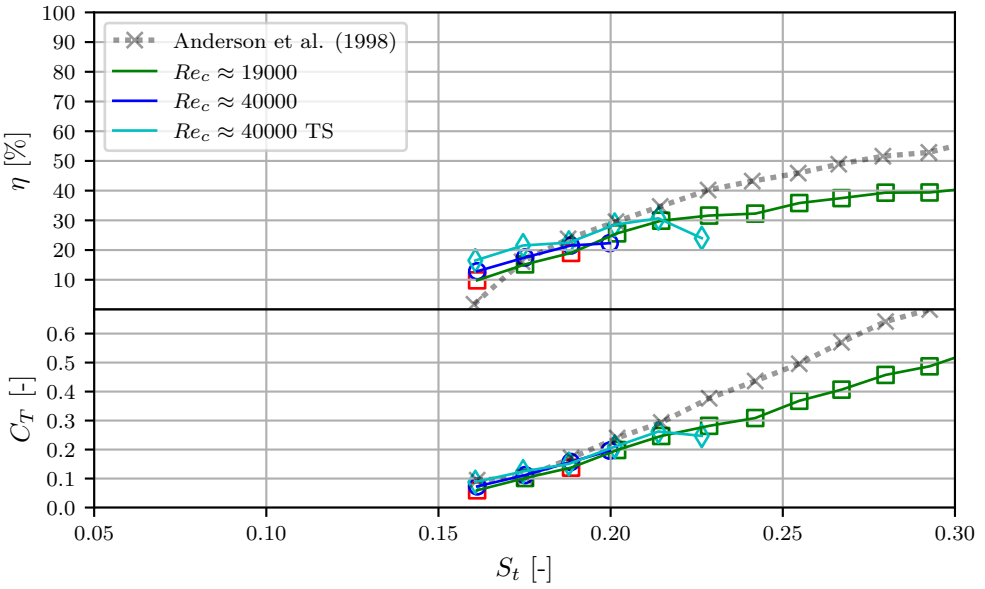

(a) Frictionless, drag zeroed with inflow-velocity.

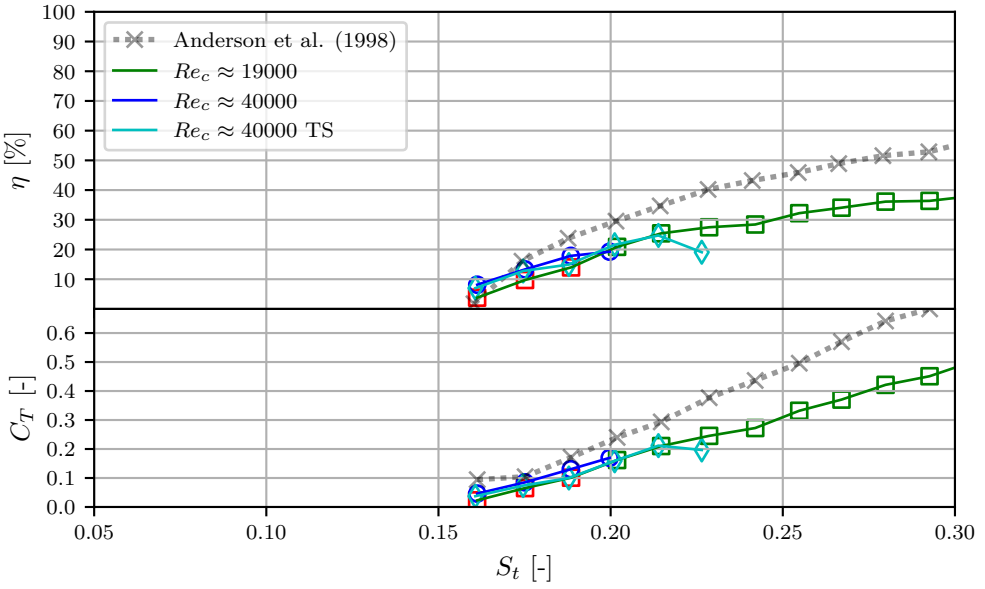

(b) Drag included, zeroed without inflow-velocity.

Figure I.7: Repetition of Anderson's case 1 with parameters: $\alpha_{max} = 30°$, $\phi = 90°$, $y_{sway}^{amp} = 0.75$.

J Grid to determine S_t-α_{max} contour for η and C_T.

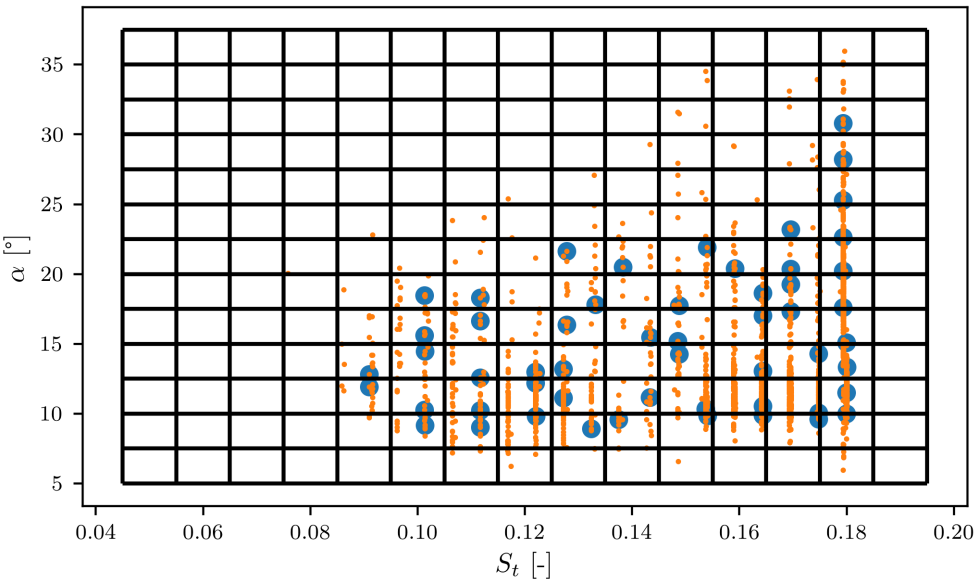

(a) $Re \approx 40000$]

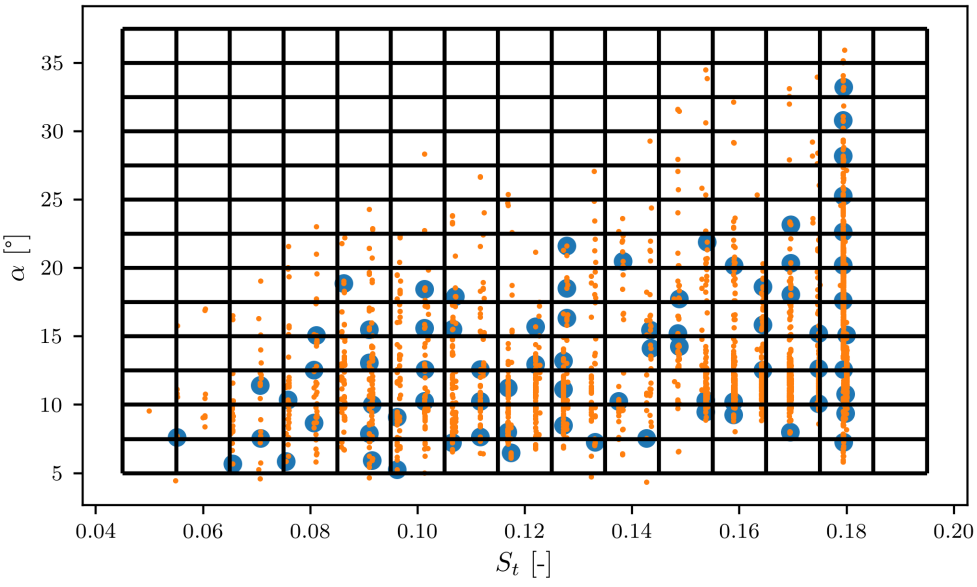

(b) $Re \approx 40000$ frictionles

Figure J.1: The individual with highest efficiency is selected in each grid cell to be used for the contourplot in figure 4.11. The selected individuals are marked with a blue dot.

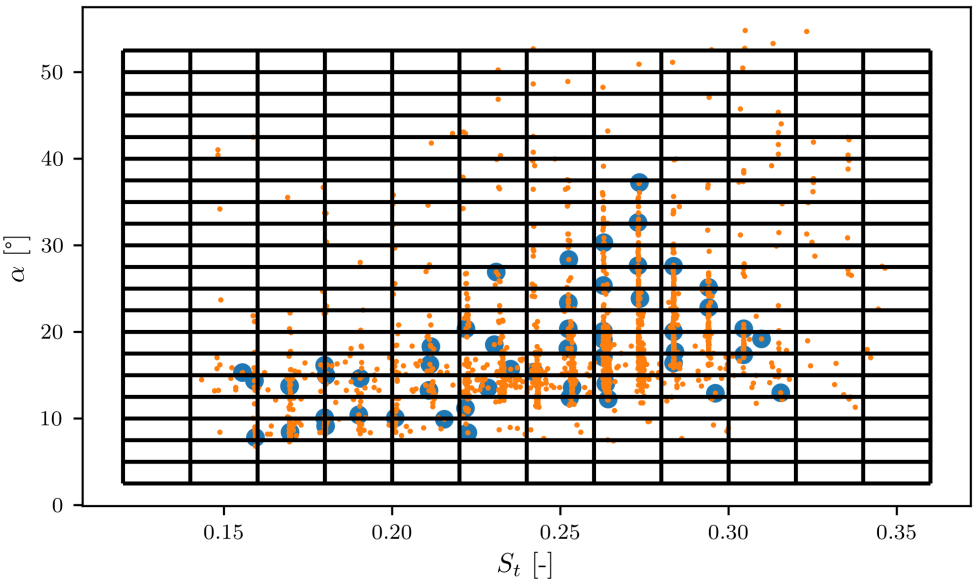

(a) $Re \approx 19000$

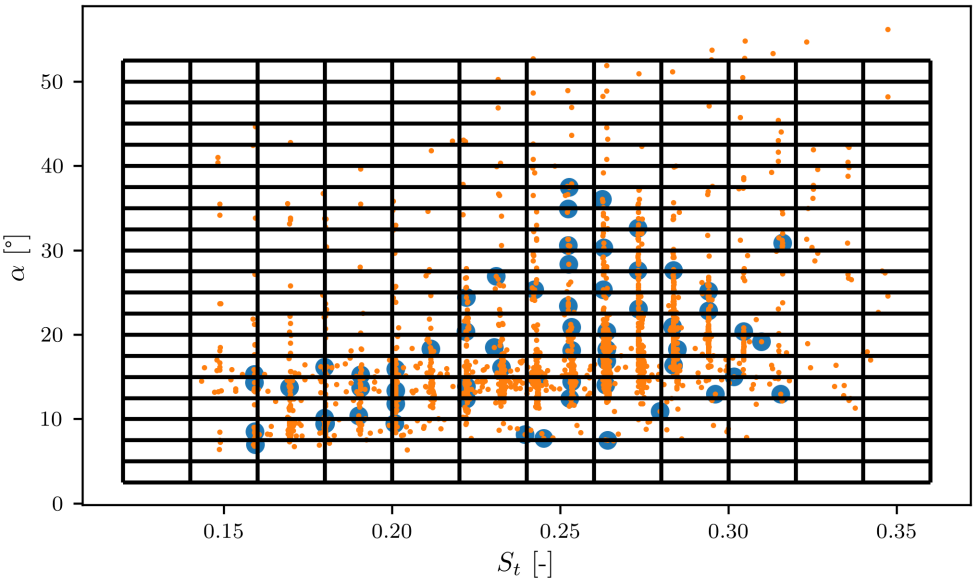

(b) $Re \approx 19000$ frictionless

Figure J.2: The individual with highest efficiency is selected in each grid cell to be used for the contourplot in figure 4.12. The selected individuals are marked with a blue dot.